

Pervasive epistasis modulates neurodevelopmental defects of the autism-associated 16p11.2 deletion

Janani Iyer^{1,9}, Mayanglambam Dhruba Singh^{1,9}, Matthew Jensen^{1,2,9}, Payal Patel^{1,9}, Lucilla Pizzo¹, Emily Huber¹, Haley Koerselman³, Alexis T. Weiner¹, Paola Lepanto⁴, Komal Vadodaria¹, Alexis Kubina¹, Qingyu Wang^{1,2}, Abigail Talbert¹, Sneha Yennawar¹, Jose Badano⁴, J. Robert Manak^{3,5}, Melissa M. Rolls¹, Arjun Krishnan^{6,7}, and Santhosh Girirajan^{1,2,8*}

1. Department of Biochemistry and Molecular Biology, The Pennsylvania State University, University Park, PA 16802
2. Bioinformatics and Genomics Program, Huck Institute of Life Sciences, The Pennsylvania State University, University Park, PA 16802
3. Departments of Biology, University of Iowa, Iowa City, IA 52242
4. Human Molecular Genetics Laboratory, Institut Pasteur de Montevideo, Montevideo, Uruguay
5. Department of Pediatrics, University of Iowa, Iowa City, IA 52242
6. Department of Computational Mathematics, Science and Engineering, Michigan State University, East Lansing, MI 48824
7. Department of Biochemistry and Molecular Biology, Michigan State University, East Lansing, MI 48824
8. Department of Anthropology, The Pennsylvania State University, University Park, PA 16802
9. These authors contributed equally to this work.

Correspondence to:

Santhosh Girirajan
 205A Life Sciences Building
 The Pennsylvania State University
 University Park, PA 16802
 E-mail: sxg47@psu.edu
 Phone: 814-865-0674

ABSTRACT

As opposed to syndromic CNVs caused by single genes, extensive phenotypic heterogeneity in variably-expressive CNVs complicates disease gene discovery and functional evaluation. Here, we propose a complex interaction model for pathogenicity of the autism-associated 16p11.2 deletion, where CNV genes interact with each other in conserved pathways to modulate expression of the phenotype. Using multiple quantitative methods in *Drosophila* RNAi lines, we identified a range of neurodevelopmental phenotypes for knockdown of individual 16p11.2 homologs in different tissues. We tested 565 pairwise knockdowns in the developing eye, and identified 24 interactions between pairs of 16p11.2 homologs and 46 interactions between 16p11.2 homologs and neurodevelopmental genes that suppressed or enhanced cell proliferation phenotypes compared to one-hit knockdowns. These interactions within cell proliferation pathways were also enriched in a human brain-specific network, providing translational relevance in humans. Our study indicates a role for genetic interactions within CNVs and identifies potential therapeutic targets for neurodevelopmental disorders.

Rare recurrent copy-number variants with breakpoints typically mapping within segmental duplications are a significant cause of neurodevelopmental disorders, such as intellectual disability/developmental delay (ID/DD), autism, epilepsy, and schizophrenia¹. Gene discovery within rare syndromic CNVs has traditionally involved mapping the disease-associated region using atypical CNVs, inversions, or translocations to identify a causative gene that explains the distinct phenotypes associated with the CNV, followed by detailed functional evaluation of that gene using animal models. Using this approach, the retinoic acid induced 1 gene (*RAI1*) was identified as the locus responsible for the core features of Smith-Magenis syndrome², and individual genes within chromosome 7q11.23 were connected to specific Williams-Beuren syndrome phenotypes, such as *ELN* for cardiovascular features³. Absence of atypical deletions for other CNVs required more direct functional evidence for implicating a candidate gene. For example, the role of *TBX1* in aortic arch defects observed in individuals with 22q11.2 deletion/DiGeorge syndrome was identified through a functional screen for cardiac features in a series of mouse models carrying overlapping deletions of the human syntenic region⁴. All of these examples provide evidence that dosage alteration of one or more genes within the syndromic CNV interval contribute to the observed phenotypes.

Unlike rare CNVs associated with a consistent set of phenotypes, more recently described rare CNVs are associated with a range of neurodevelopmental features, and are also reported in unaffected or mildly affected individuals¹. One such CNV is the 16p11.2 deletion, which encompasses 593 kbp and 25 unique genes. The deletion was originally identified in individuals with autism^{5, 6}, and subsequently reported in children with ID/DD⁷, epilepsy⁸, and obesity⁹. Several themes have emerged from recent studies on dissecting the role of individual genes within the 16p11.2 deletion region towards neurodevelopmental phenotypes. *First*, extensive heterogeneity and incomplete penetrance of the associated phenotypes adds additional challenges to genetic mapping strategies that use atypical variants. *Second*, while this deletion is enriched within various neurodevelopmental disease cohorts, exome sequencing studies of hundreds of individuals have not identified any individual genes within this region as causative for these diseases on their own^{10, 11, 12, 13}. *Third*, functional studies using cellular^{14, 15, 16}, mouse^{17, 18, 19, 20, 21}, and zebrafish models^{22, 23, 24} have implicated several different genes within 16p11.2 in neurodevelopmental phenotypes. These findings suggest that the observed phenotypes in 16p11.2 deletion are not caused by haploinsufficiency of a single causative gene, but rather are

modulated by multiple dosage-sensitive genes in the region, potentially through combinatorial mechanisms within pathways related to neurodevelopment. This model is also consistent with a recent observation that pathogenic CNVs are more likely to contain clusters of functionally related genes than benign CNVs²⁵, suggesting intra-CNV genetic interactions as a potential cause for CNV pathogenicity. Therefore, an approach that combines a systematic functional evaluation of each gene within 16p11.2 and its genetic interactions is necessary to identify key neurodevelopmental pathways and molecular mechanisms of disease.

Evaluation of gene interactions in neurodevelopment requires a system that is sensitive to genetic perturbations but, at the same time, allows for performing interaction studies in the nervous system without compromising viability of the organism. *Drosophila melanogaster* provides such a model, as developmental processes, synaptic mechanisms, and neural structure and signaling are conserved between flies and vertebrates²⁶. In fact, neurodevelopmental disorders such as Angelman Syndrome²⁷, Rett Syndrome²⁸, Fragile X syndrome²⁹, and intellectual disability³⁰ have been modeled in flies, while several studies have used *Drosophila* models to test for genetic interactions^{31, 32, 33}. We used the power of *Drosophila melanogaster* as a genetic model to perform a series of quantitative and high-throughput assays to systematically characterize phenotypes, function, cellular mechanisms, and interactions of conserved homologs of human 16p11.2 genes. Our data suggest a complex interaction model for disease pathogenicity, where multiple 16p11.2 genes are sensitive to dosage imbalance and participate in complex interactions that both enhance and suppress the phenotypic effects of each other within cellular proliferation pathways, and in turn are modulated by other genes in the genetic background.

RESULTS

Multiple 16p11.2 homologs contribute to neurodevelopmental phenotypes

We identified 14 fly homologs from the 25 human 16p11.2 genes (Table S1), and used 31 RNA interference (RNAi) lines and tissue-specific *GAL4* drivers to knockdown the expression levels of individual homologs ubiquitously or in neuronal, eye, or wing tissues (Figures 1 and 2A). RNAi is an effective strategy to model partial reduction of gene expression, which in principle recapitulates the effect of a heterozygous microdeletion, and for high-throughput screening of genes for tissue specific phenotypes. We used multiple independent *UAS-RNAi* transgenes targeting the same gene to validate our results (Figure S1A, Table S2), and used stringent quality control to eliminate lines that showed phenotypes due to off-target or positional effects (Figure S1A). Using quantitative PCR, we measured the reduction in gene expression for each line with neuronal knockdown (using *Elav-GAL4>Dicer2* at 25°C), and on average achieved approximately 50% reduction in gene expression for the tested 16p11.2 homologs (Table S3). As this study is focused on studying the functional role of human genes in a fly model, we represent the identified fly homologs in the format of *HumanGene*^{*FlyGene*}—for example, *MAPK3*^{*rl*}.

We performed a series of quantitative assays on 16p11.2 homologs for more than 20 phenotypes that have been classically used to measure conserved developmental function in flies, and identified lethality and a variety of morphological phenotypes due to ubiquitous and tissue-specific knockdown²⁹ (Figures 1 and 2A). For example, seven homologs were lethal at the larval or pupal stage with ubiquitous knockdown, indicating that these genes are essential for viability and development in *Drosophila*³⁴. We next performed pan-neuronal knockdown experiments and tested for several nervous system phenotypes, such as climbing assays for motor impairment and spontaneous seizures. We performed negative geotaxis experiments to measure locomotor function and identified dramatic reductions in the climbing ability of *ALDOA*^{*ald*} and *MAPK3*^{*rl*} knockdown flies throughout the testing period (Figure 2B, Figure S2A). Since about 20% of individuals with 16p11.2 deletion manifest seizures³⁵, we next used a recently developed spontaneous seizure assay that assesses unprovoked seizures in their native state, which better recapitulates human seizures in *Drosophila*³⁶. We found that *MAPK3*^{*rl*}, *PPP4C*^{*pp4-19C*}, and *KCTD13*^{*CG10465*} knockdown flies were more likely to show seizure phenotypes compared to controls (Figure 2C, Figure S2B).

We further examined deeper cellular features, including neuromuscular junction, dendritic arborization, and axonal targeting, to understand the molecular basis of the observed neuronal features. *Drosophila* neuromuscular junction (NMJ) is a well-established model for studying synapse growth defects, and alterations in NMJ architecture have been documented in genes associated with autism²⁹. We found significant differences in NMJ structure at body wall muscles 6-7 with knockdown of *CDIPT*^{pis} and *FAM57B*^{CG17481} compared to controls, suggesting altered growth and development of the NMJ in these flies (Figure 2D, Figures S2C and S2D). The architecture of dendritic arbors also plays an important role in neural circuit formation, and defects in dendrites are associated with neurodevelopmental disorders such as schizophrenia and autism³⁷. To assay dendritic growth and structure, we examined large branched dendrites of the class IV ddaC sensory neuron in intact larvae after gene knockdown with the *ppk-GAL4* driver³⁸, and observed decreased complexity in dendritic arborization with knockdown of *KCTD13*^{CG10465} and increased complexity with knockdown of *TAOK2*^{dTao-1} (Figure 2E, Figures S2E and S2F). Another hallmark of nervous system development is the accuracy of synaptic connections, which is determined by the guidance of axons to their correct targets³⁹. We explored axonal targeting by staining larval eye discs of flies using chaoptin antibody, and observed aberrant targeting in *KCTD13*^{CG10465} and *MAPK3*^{rl} flies (Figure 2F). In summary, we found multiple developmental and neuronal defects for each of the homologs, indicating the pleiotropic effect of conserved 16p11.2 genes and their importance in neurodevelopment.

***Drosophila* eye models identify cellular proliferation phenotypes in 16p11.2 homologs**

Decades of studies have shown that the *Drosophila* eye is an accessible and sensitized experimental system for quantitative studies of nervous system development and function, as genetic defects that alter the development of a single cell type can lead to observable rough eye phenotypes^{40, 41} (Figures 3A and 3B). In fact, genetic interaction studies using the fly eye have led to the discovery of novel modifier genes in nervous system disorders, such as Rett syndrome and spinocerebellar ataxia type 3^{28, 42}, as well as conserved developmental processes⁴³. To quantify the degree of severity of the eye phenotypes, we developed and tested a computational method called *Flynotyper* that calculates a phenotypic score based on the disorderliness of ommatidial arrangement at high sensitivity and specificity⁴⁴. We performed eye-specific knockdown of gene expression using the *GMR-GAL4* driver with and without *Dicer2* for all

Drosophila 16p11.2 homologs, and compared the degree of phenotypic severity as measured by *Flyntyper* to controls with the same genetic background (Figures 3C and 3D, Figure S3A-C). We found a strong correlation (Pearson correlation, $r=0.69$, $p=2.88 \times 10^{-6}$) between the percentile ranks of all tested RNAi lines with *Dicer2* and without *Dicer2* (Figure S3D). As shown in Figure 3D, we observed a range of severe but significant eye defects for nine homologs, which were comparable to that of genes associated with neurodevelopmental disorders such as *CHD8^{kis}*, *SHANK3^{prosap}*, *SCN1A^{para}*, and *PTEN^{dpten}* (Table S4, Figure S3D). For example, the severity of eye defects in *KCTD13^{CG10465}*, *DOC2A^{rph}*, and *PPP4C^{pp4-19C}* knockdown flies had phenotypic scores greater than the 85th percentile of the tested 39 fly homologs of human neurodevelopmental genes (Table S4). These results suggested that knockdown of 16p11.2 homologs affect development of the fly eye to varying degrees of severity, which mirrors the global developmental and neurological defects observed with ubiquitous and pan-neuronal knockdown.

To investigate the cellular basis of the rough eye phenotype observed in individual gene knockdowns, we stained the pupal eye imaginal disc with Discs large (Dlg) antibody for ommatidial cells and Phalloidin for photoreceptor neurons, and screened for anomalies in different cells in the developing eye (Figures 3A-3C). A variety of cellular defects leading to altered structure of the hexagonal lattice were observed with knockdown of seven of the homologs, suggesting potential alterations in cellular proliferation (Figures 3E and 3F, Figure S4). For example, *KCTD13^{CG10465}* knockdown flies showed a drastic increase in the number of cone cells, secondary pigment cells, and photoreceptor neurons, while *MAPK3^{rl}* knockdown showed a decreased number of interommatidial cells and photoreceptor neurons, with a consequent loss of the hexagonal structure in the ommatidia. Similarly, *ALDOA^{ald}* knockdown flies had misplaced bristle cells as well as an increase in secondary and photoreceptor cells, while *PPP4C^{pp4-19C}* knockdowns showed severe rotational defects and a complete loss of the ommatidial architecture. Overall, we found that knockdown of several 16p11.2 homologs contribute to defects in cell count and patterning of different cell types, including photoreceptor neurons and ommatidial cells, during development.

We further investigated cellular mechanisms associated with the observed developmental defects, as recent functional studies have implicated defects in neuronal proliferation as a cellular mechanism underlying autism disorders⁴⁵. In fact, genome-wide CNV and exome sequencing

studies of individuals with autism have uncovered pathogenic variants enriched for cell proliferation genes^{46, 47}. We used phospho-Histone H3 (pH3) antibody and bromodeoxyuridine (BrdU) staining to identify dividing cells, and counted the number of stained cells posterior to the morphogenetic furrow of the developing larval eye (Figures 3A and 3C, Figure S4). Several homologs showed a significant alteration in dividing cell counts (Figure 3G). For example, we found an increase in mitotic cell count with knockdown of *KCTD13*^{CG1046}, *CDIPT*^{pis}, and *ALDOA*^{ald}, while *MAPK3*^{rl} knockdown flies showed a significant reduction in proliferating cells. No changes in cell differentiation were observed using *Elav* staining in *KCTD13*^{CG10465} and *MAPK3*^{rl} knockdowns, suggesting that these two genes are specifically involved in cell proliferation (Figures S4B). Consistent with the proliferation phenotypes, we also observed an overall increase in the adult eye area in four RNAi knockdowns comparable to flies with knockdown of *PTEN*^{dpten}, a known cell proliferation gene⁴⁸, as well as a decrease in eye area for *MAPK3*^{rl} flies (Figure 3H). For *KCTD13*^{CG1046} knockdown flies, we also found an increase in the size of ommatidia similar to that observed for *PTEN*^{dpten} knockdown, indicating that cell growth defects in these flies may also occur with the observed increase in cell proliferation (Fig. S4C). Overall, our analysis of individual gene knockdowns showed that reduced expression of individual 16p11.2 homologs cause defects in cell proliferation and organization.

Interactions between 16p11.2 homologs modulate neurodevelopmental and cellular phenotypes

Our phenotypic and functional studies of individual 16p11.2 homologs showed that many genes within the CNV region are involved in neurodevelopment, indicating that no single gene in the region is solely responsible for the observed neuronal phenotypes of the deletion. Based on these observations we hypothesized that interactions between genes within the 16p11.2 region may contribute to the observed phenotypes. To systematically test interactions between 16p11.2 homologs in the developing fly eye, we selected a subset of four homologs, including *PPP4C*^{pp4-19C}, *MAPK3*^{rl}, *KCTD13*^{CG10465} and *DOC2A*^{rph}, and generated recombinant lines expressing their respective RNAi lines with the *GMR-GAL4* driver. We selected these genes as primary drivers of neurodevelopmental phenotypes based on severity of phenotypes with various tissue-specific knockdowns (Figure 2A), published functional studies in mouse and zebrafish (Table S1), and identifiable eye phenotypes amenable for large-scale modifier screens (Figure 3D).

We generated 52 two-locus fly models (123 total lines) by reducing gene expression of each of the four homologs in combination with the 13 other 16p11.2 homologs. We used manual eye scoring and *Flynotyper* to compare these pairwise knockdown lines to respective control flies with single gene knockdowns. In this way, we identified 24 pairwise interactions of 16p11.2 homologs, validated with multiple RNAi or deficiency lines that enhanced or suppressed the rough eye phenotypes observed with single-hit knockdown of the four tested genes (Figures 4 and S5, Table S5). Reduced expression of seven 16p11.2 homologs resulted in suppression of the rough eye phenotypes observed in *MAPK3^{rl}* knockdown flies, including a full rescue of the *MAPK3^{rl}* phenotype with simultaneous knockdown of *CORO1A^{coro}* and a partial rescue with knockdown of *C16ORF53^{pal}* and *FAM57B^{CG17641}* (Figures 4A and S5A). We also found that double knockdown of *MAPK3^{rl}* and *PPP4C^{pp4-19C}* led to an enhancement of the *MAPK3^{rl}* rough eye phenotype. Similarly, reduced expression of six 16p11.2 homologs partially rescued the severe rough eye phenotype in *KCTD13^{CG10465}* knockdown models, including *CORO1A^{coro}* and *ALDOA^{ald}* (Figures 4B and S5B). Further, the glossy eye phenotype observed in one-hit knockdown of *PPP4C^{pp4-19C}* was suppressed by reduced expression of five homologs, including *YPEL3^{CG15309}* and *CDIPT^{pis}* (Figures 4C and S5C). We also observed an enhancement of the rough eye phenotype with double knockdown of *PPP4C^{pp4-19C}* and *KCTD13^{CG10465}* at 30°C, which we initially suspected to be due to the severity of *KCTD13^{CG10465}* knockdown by itself. To dissect this interaction, we performed reciprocal crosses of *KCTD13^{CG10465}* RNAi lines with *PPP4C^{pp4-19C}* at 25°C, and confirmed the phenotypic enhancement observed at 30°C (Figure S5D). Finally, the rough eye phenotypes in *DOC2A^{rph}* knockdown models were suppressed by reduced expression of *CDIPT^{pis}* and *ALDOA^{ald}* (Figure S5E).

We tested a subset of 16p11.2 interaction pairs for alteration in their cellular phenotypes by staining the pupal and larval eye discs with anti-Dlg and anti-pH3, respectively (Figures 4E and S5F). Assessing the count, structure, and orientation of the cells in the developing eye discs confirmed several interactions documented in the adult eyes. For example, reduced expression of *ALDOA^{ald}* in *MAPK3^{rl}* models rescued the rotation errors and primary cell defects in the pupal eye, as well as proliferation defects in the larval eye (Figures 4E-4G, Figure S5H). Similarly, *ALDOA^{ald}* knockdown suppressed the cone cell defects, secondary cell defects, and rotation errors observed in *KCTD13^{CG10465}* knockdown pupae, and showed a significant reduction in the number of proliferating cells compared to the *KCTD13^{CG10465}* larval eye (Figures 4E-4G, Figure

S5H). Although reduced expression of *TAOK2*^{dTao-1} did not rescue external eye defects in *MAPK3*^{rl} and *KCTD13*^{CG10465} knockdown flies, we observed partial rescue of cellular defects in the pupa and a significant rescue of proliferation defects in *MAPK3*^{rl} and *KCTD13*^{CG10465} larval eyes (Figures 4E-4G, Figure S5F-S5H). To test if the two-hit interactions observed in the fly eye were also relevant in the nervous system, we evaluated the accuracy of retinal axon innervation into the lamina and medulla of the brain using anti-chaoptin in larvae with knockdown of both *KCTD13*^{CG10465} and *CORO1A*^{coro}, and confirmed a complete rescue of the axonal targeting defects observed in single-hit *KCTD13*^{CG1046} flies (Figure 4D).

Some literature evidence exists for the functional interactions documented in our study. For example, *MAPK3* and *TAOK2* are both involved in synaptic assembly and signaling⁴⁹, and *ALDOA* was identified as a member of the MAP kinase (ERK1/2) interactome in differentiating epidermal and neuronal cells⁵⁰. We also found that the tested 16p11.2 genes were connected to each other through intermediates at different degrees of separation within human gene interaction networks, potentially explaining the varying degrees of phenotypic modulation observed in the two-hit fly models (Figure S5I). For example, the apoptosis regulatory gene⁵¹ *FKBP8* interacts with both *KCTD13* and *ALDOA* in the brain, serving as an intermediate between these two genes. In fact, certain 16p11.2 human genes without fly homologs, including *MAZ* and *HIRIP3*, appeared as intermediate genes in our networks, further demonstrating the pervasive interactions between 16p11.2 genes. Overall, we found that pairwise knockdowns of 16p11.2 genes modulate cell proliferation defects observed in single-gene knockdowns during development. These defects can not only be enhanced but also rescued or suppressed by simultaneous knockdown of another 16p11.2 homolog, indicating that interactions between 16p11.2 homologs are epistatic in nature, where the phenotypic effects of two genes are greater or less than the sum of the effects of each individual gene⁵². These results point towards a new model for pathogenicity of the 16p11.2 deletion, where genes within the region are functionally related and interact with each other in conserved pathways to modulate the expression of the neurodevelopmental phenotype.

Interactions of 16p11.2 homologs within cell proliferation pathways determine the pathogenicity of the phenotype

To further explore the membership of 16p11.2 homologs within cellular and developmental pathways, we extended our two-hit interaction studies to include 18 homologs of known

neurodevelopmental genes and 32 homologs of genes within five pathogenic CNV regions: 16p11.2 distal, 1q21.1, 15q13.3, 15q11.2, and 3q29. Using recombinant lines of *MAPK3^{rl}*, *KCTD13^{CG10465}*, *PPP4C^{pp4-19C}* and *DOC2A^{rph}*, we tested a total of 200 pairwise gene interactions in 420 total lines (*UAS-RNAi* and deficiency lines) using manual scoring (Figure 5A) and *Flynotyper* (Figure 5C), and identified 46 interactions with 26 neurodevelopmental and CNV genes (Figure 5B, Figures S6, Table S6). Interestingly, 17 of these interactions of 16p11.2 homologs were with genes known to be involved in cell proliferation. For example, knockdown of the Wnt signaling pathway gene⁵³ *CHD8^{kis}* resulted in a complete rescue of *MAPK3^{rl}* phenotype as well as a strong suppression of the *KCTD13^{CG10465}* rough eye phenotype (Figures 5C and S6). Similarly, reduced expression of beta catenin, *CTNNB1^{arm}*, significantly enhanced the phenotypes observed with *MAPK3^{rl}*, *KCTD13^{CG10465}*, and *PPP4C^{pp4-19C}* one-hit knockdowns (Figure 5C). Knockdown of *SHANK3^{prosap}*, a gene that codes for a post-synaptic scaffolding protein and is associated with autism⁵⁴, suppressed the rough-eye phenotype of *KCTD13^{CG10465}*, *MAPK3^{rl}*, and *PPP4C^{pp4-19C}* flies (Figure 5C). These data show that multiple 16p11.2 homologs interact through conserved neurodevelopmental genes that potentially act as intermediates, whose knockdown modulates the expression of the ultimate phenotype. Interestingly, six genes within the 16p11.2 distal CNV region⁵⁵ interacted with 16p11.2 homologs. For example, reduced expression of *SH2B1^{lnk}* fully rescued the rough-eye phenotype observed with knockdown of *MAPK3^{rl}*, while *ATXN2L^{atx2}* knockdown led to a more severe phenotype in *PPP4C^{pp4-19C}*, *KCTD13^{CG10465}*, and *DOC2A^{rph}* knockdown flies (Figures 5C and S6). These results suggest overlapping functional roles in neurodevelopment for genes within the proximal and distal 16p11.2 regions apart from chromosomal contacts between the two syntenic segments in humans⁵⁶. We further assessed the cellular mechanisms responsible for suppression of the *MAPK3^{rl}* rough eye phenotype by simultaneous knockdown of the autism-associated tumor suppressor⁵⁷ *PTEN^{dpten}* (Figures 5C-5F). We observed a complete rescue of the bristle group defects, rotation errors, primary and secondary cell defects, and photoreceptor cell counts in the pupal eye of the two-hit knockdowns, and a complete rescue of cell proliferation defects observed with *MAPK3^{rl}* single-hit knockdown (Figures 5D-5F, Figure S6E and 6F).

Transcriptome studies of 16p11.2 homologs show a network of genes enriched for cell proliferation

To examine functional processes associated with 16p11.2 homologs, we selected six 16p11.2 homologs, *MAPK3^{rl}*, *KCTD13^{CG10465}*, *DOC2A^{rph}*, *CORO1A^{coro}*, *C16ORF53^{pal}*, and *CDIPT^{pis}*, based on high phenotypic severity, and performed RNA sequencing on fly heads for each knockdown to identify differentially-expressed genes (Table S7). We first conducted parametric gene-set enrichment analysis⁵⁸ to identify Gene Ontology terms enriched for human homologs of up- or down-regulated genes in each fly model relative to the control (Figure S7A, Table S7). Several terms related to neurodevelopment, including cell proliferation, cell cycle process, neurogenesis, neuron differentiation, neuron projection development, and cell-cell signaling, were significantly enriched in the knockdown models ($p < 0.01$, corrected by Benjamini-Hochberg method) (Figure S7A). Based on the cell proliferation phenotypes observed in the fly eye, we further constructed a network of differentially-expressed genes annotated for cell cycle and proliferation in humans (Figure S7B). Interestingly, we found a significantly high degree of overlap among differentially-expressed cell proliferation genes between the knockdown models (empirical $p < 0.001$), with 38.5% (65/169) of these genes differentially expressed in two or more models and 16.6% (28/169) differentially expressed in at least three knockdown models. These results provide additional evidence that the 16p11.2 homologs function in well-connected cell proliferation pathways in both *Drosophila* and humans.

We next selected 22 genes that were among the most up-regulated genes in *KCTD13^{CG10465}* and *MAPK3^{rl}* models for two-hit interaction experiments, and identified 18 genes whose knockdown suppressed the rough eye phenotypes in the *MAPK3^{rl}* and *KCTD13^{CG10465}* flies (Figures 6A and 6B). For example, knockdown of *COX6A2^{cox6AL}* fully rescued the *MAPK3^{rl}* rough eye phenotype, and knockdown of *CNGA2^{CG42260}*, *CYP24A1^{cyp12d1-d}* and *RAF1^{CG14607}* suppressed the *KCTD13^{CG10465}* phenotype. We further examined the cellular phenotypes of *COX6A2^{cox6AL}/MAPK3^{rl}* and *RAF1^{CG14607}/KCTD13^{CG10465}* knockdowns by staining the larval and pupal eye discs with anti-Dlg, phalloidin, anti-pH3, and anti-chaoptin (Figures 6C-6F, Figures S6E and S6F). Defects in cone cells, primary and secondary cells, and photoreceptor and proliferating cell count were all corrected in both two-locus models (Figures 6D and 6E, Figures S6E and S6F). Additionally, *RAF1^{CG14607}* and *COX6A2^{cox6AL}* knockdowns rescued the aberrant axonal targeting observed in *KCTD13^{CG10465}* and *MAPK3^{rl}* flies, respectively (Figure 6F). While

interactions between *RAF1* and *KCTD13* have not been previously reported, *COX6A2* was shown to interact with *MAPK3* within a human-specific gene interaction network⁵⁹. *COX6A2* was also differentially expressed in a 16p11.2 deletion mouse model¹⁴, providing further evidence for this interaction. Of note, although the transcriptome analysis was performed on fly brains using a neuron-specific driver, we were able to validate those interactions in the fly eye, supporting the utility and veracity of using the *Drosophila* eye to study nervous system interactions.

Concordance of functional interactions with human brain-specific genetic interaction network provides translational relevance

To assess the relevance of the identified functional interactions in our fly experiments to neurodevelopment in humans, we explored the functional context of the human 16p11.2 genes and their involvement in cell proliferation, specifically in relation to brain biology, using a Bayesian network of known and predicted genetic interactions in the brain. We first mapped 14 homologs of 16p11.2 genes and 35 interacting genes identified from fly experiments (26 key neurodevelopmental genes and nine differentially-expressed genes from transcriptome studies) onto a human brain-specific gene interaction network^{60, 61}, and then identified additional genes in the network that connected these genes to each other. Overall, we found 982 interactions present in the human brain, with 39 out of the 49 tested genes connected through 428 novel genes within the network (Figure 6G, Table S8). A significant enrichment for cell cycle and cell proliferation function was identified among these novel connector genes (96/428, one-tailed Fisher's exact test, $p=3.14 \times 10^{-12}$). However, we also found the same enrichment among connector genes for random sets of fly genes exhibiting neurological and behavioral phenotypes, indicating that this result is likely a general characteristic for genes involved in neurodevelopment. Additionally, our connector genes were enriched for genes related to neurodevelopment, including FMRP-protein binding genes ($p=3.34 \times 10^{-14}$, one-tailed Student's t-test) and genes involved in post-synaptic density ($p=3.31 \times 10^{-32}$), as well as genes differentially expressed in the fly knockdown models ($p=0.0215$). These results suggest a strong concordance between data obtained from fly two-locus experiments with putative interactions identified in the human nervous system, and provide a novel set of candidates that could be potential therapeutic targets for the deletion phenotypes.

DISCUSSION

We used the sensitive genetic system of *Drosophila* to identify conserved functions and interactions of 16p11.2 homologs. While previous functional studies of the 16p11.2 region have either focused on the phenotypic effects of the whole deletion or the additive effects of individual genes, our work provides functional evidence that uncovers a complex model of genetic interactions in this region. The composite system of the fly eye allowed us to assay multiple genes and hundreds of interactions using high-throughput and quantitative assays for neurodevelopment without compromising the organism's viability. In fact, we were able to validate nervous system-specific interactions identified through transcriptome studies using both the fly eye and a human brain-specific network, which provides strong support for the use of genetic screens in the *Drosophila* eye for studying mechanisms of disease in the nervous system. Additionally, we identified multiple interactions of conserved 16p11.2 homologs that are consistent with published biochemical studies as well as functional gene networks constructed from human co-expression and protein-protein interaction datasets. Screening for interactions with neurodevelopmental genes and differentially-expressed genes in the transcriptome was particularly useful in identifying potential therapeutic targets for 16p11.2 deletion phenotypes. For example, rapamycin has been shown to rescue cellular and behavioral phenotypes in mouse knockouts of *PTEN*⁶², while sorafenib inhibits growth and promotes apoptosis in cancer cells with *RAF1* mutations^{63, 64}. In the context of the deletion, the identified suppressors of multiple 16p11.2 homologs both within and outside the region, such as *ALDOA*, *CORO1A*, *CHD8*, *PTEN*, and *RAF1*, could be targeted for therapeutic strategies that target cell cycle pathways. This approach is especially well suited for 16p11.2 deletion, where genes participate in a shared pathway that can be targeted by a single treatment (instead of multiple targets for individual CNV genes). Although we observed interactions in the subset of 16p11.2 genes with homologs in *Drosophila*, it is likely that genes without fly orthologs also contribute to complex genetic interactions in the region. In fact, two 16p11.2 genes not tested in flies, *MAZ* and *HIRIP3*, were found in human gene interaction networks based on the tested homologs. Interactions between *MAZ* and other 16p11.2 genes are especially noteworthy, as a recent study reported cell proliferation defects in human embryonic kidney cells upon siRNA knockdown of *MAZ*⁶⁵. Overall, our findings provide evidence for specific interactions in the 16p11.2 region that can be integrated with data from more sophisticated neurobiological systems, such as human stem cells,

mouse, and zebrafish, to fully explain the complex interactions responsible for the neurodevelopmental phenotypes observed in 16p11.2 deletion carriers.

Multiple lines of evidence including two-hit screening in the fly eye, transcriptome data from fly heads, and human brain-specific genetic interaction network suggest that interactions among 16p11.2 genes are mediated through cellular proliferation and cell cycle pathways, which are well-conserved between flies and humans^{66, 67}. In fact, several 16p11.2 genes have already been implicated in these cellular pathways. For example, *MAPK3* is a key member of the MAPK/ERK signaling pathway, which is partially regulated by *TAOK2* and *ALDOA*^{49, 50}, while *KCTD13* encodes PDIP1 (polymerase delta-interacting protein 1), which interacts with the proliferating cell nuclear antigen and therefore could have a role in the regulation of cell cycle during neurogenesis⁶⁸. Our results are also consistent with aberrant changes in proliferation during early cortical neurogenesis observed in a 16p11.2 deletion mouse model¹⁹. While a recent study by Deshpande and colleagues did not find defects in cell proliferation in their neural progenitor cells¹⁶, the discrepancies could be attributed to testing individual 16p11.2 genes versus the entire deletion or due to model system specific sensitivities. Interestingly, we also found increased ommatidial size with knockdown of *KCTD13*^{CG10465}, similar to that of *PTEN*^{dpten}. This result is consistent with data from Deshpande and colleagues showing increased cell growth in human iPSC-derived neurons from patients with the 16p11.2 deletion¹⁶. In contrast to increased cell growth in the fly eye, we also found reduced dendritic complexity for *KCTD13*, suggesting that the cell growth defects observed with knockdown of individual 16p11.2 genes could also be cell-type specific.

Our results suggest that multiple 16p11.2 homologs contribute to a range of phenotypes that have key roles in different tissue types and organ systems, indicating pleiotropic effects in *Drosophila* that mirror the multitude of phenotypes observed in humans. These data are consistent with other functional studies of 16p11.2 knockdown or knockout models in mouse and zebrafish, which show abnormal neuronal or developmental phenotypes for multiple genes (Table S1). Additionally, several 16p11.2 genes have similar intolerance to variation and likelihoods of having loss-of-function mutations compared to causative genes in syndromic CNVs¹, including *RAI1*, *SHANK3*, and *NSD1* (Table S9). The presence of multiple genes in 16p11.2 that are individually potentially pathogenic and behave similarly to classical neurodevelopmental genes, as determined by RVIS⁶⁹ and pLI scores⁷⁰, suggest that interactions

between these genes are necessary to modulate the effects of each gene in the deletion. Further, the additive effects of haploinsufficiency of all 16p11.2 genes cannot completely explain the clinical features of the deletion, as all patients with the deletion should then manifest some degree of the affected phenotype. However, this is not the case, as several clinical features of 16p11.2 deletion are not completely penetrant, including autism⁷¹ and macrocephaly³⁵. We identified 24 interactions between pairs of 16p11.2 homologs, as well as 64 interactions between the 16p11.2 homologs and key neurodevelopmental genes or genes differentially expressed in one-hit models (Figure 7). We found that 20 out of 24 interactions between 16p11.2 homologs suppressed the cellular phenotypes observed in one-hit knockdown flies, suggesting that these interactions are epistatic in nature rather than merely additive^{52, 72} (Figures 7 and S8A). While the results from our fly interaction studies fit the classical definition of epistasis, we can consider individual haploinsufficient genes within the human deletion to be independent, and their interactions with each other at a mechanistic level to be epistatic despite being located within the same variant.

Based on these results, we propose a complex interaction model for the pathogenicity of 16p11.2 deletion, where the phenotypic effects of the whole deletion may not equal the sum of the phenotypic effects due to disruption of its constituent genes. Rather, the interactions between the genes within the deletion, acting through common pathways, determine the phenotypic severity (Figure 7C). These interactions can suppress, rescue or enhance the one-hit phenotypes, providing evidence for epistasis as a phenomenon for the incomplete penetrance of clinical features associated with the deletion. The phenotypic variability of the deletion can therefore be explained by variants in upstream regulatory regions or modifier genes that also participate in these pathways (Figure 7C). In fact, the complex interactions between 16p11.2 genes can amplify the effects of second hits in the genetic background located within the same pathway, as these second hits can potentially modulate the phenotypic effects of several 16p11.2 genes at once (Figure S8B). This model is in contrast to that reported for syndromic CNVs, where the core phenotypes can be due to a single gene (such as *RAI1* in Smith-Magenis syndrome) or a subset of individual genes in the contiguous region (as in Williams syndrome), but agrees with previous findings showing epistatic interactions between genes within *de novo* CNVs identified in individuals with autism³³. Our results further suggest the importance of genetic interactions towards causation and modulation of neurodevelopmental disease, and emphasize the need for a

function-based analysis in addition to sequencing studies towards discovery of gene function in the context of genetic interactions.

METHODS

Identification of *Drosophila* homologs

We first queried the *Drosophila* genome for homologs using DRSC Integrative Ortholog Prediction Tool (DIOPT)⁷³, reciprocal BLAST and ENSEMBL database⁷⁴ for each of the 25 human 16p11.2 genes (Table S1). We narrowed down the list of homologs to 15 genes with a DIOPT score of 3 or greater, or in the case of *KIF22*^{klp68D}, high query coverage and percentage identity in BLAST. Of the 15 selected homologs, RNAi lines were available for all homologs except *INO80E*, and therefore we were unable to characterize this gene. Therefore, 14 homologs of 16p11.2 genes were used in this study. We used a similar strategy for identifying homologs for other genes tested for interactions in this study. We confirmed that all tested 16p11.2 homologs were expressed in the fly eye using database and literature searches^{75, 76, 77, 78}.

Drosophila stocks and genetics

Tissue-specific knockdown of 16p11.2 homologs and other genes tested in this study was achieved with the *UAS-GAL4* system⁷⁹, using *w; GMR-GAL4; UAS-Dicer2* (Zhi-Chun Lai, Penn State University), *dCad-GFP, GMR-GAL4* (Claire Thomas, Penn State University), *Elav-GAL4;;UAS-Dicer2* (Scott Selleck, Penn State University), *Elav-GAL4* (Mike Grotewiel, VCU), *Da-GAL4* (Scott Selleck, Penn State University), *MS1096-GAL4;; UAS-Dicer2* (Zhi-Chun Lai, Penn State University), *w; C5-GAL4;Dicer2* (Zhi-Chun Lai, Penn State University), and *UAS-RNAi* transgenic lines. The RNA interference lines were obtained from the Vienna *Drosophila* Resource Center (includes both KK and GD lines)³⁴ and the Bloomington Stock Center (NIH P40OD018537), and deficiency lines were obtained from the Bloomington Stock Center. All fly stocks and crosses were cultured on conventional cornmeal-sucrose-dextrose-yeast medium at 25°C unless otherwise indicated. For the eye-specific RNAi knockdown with *GMR-GAL4*, the temperature dependence of *GAL4* activity and knockdown efficiency with *UAS-Dicer2* allowed us to test pathogenicity at varying doses of expression. We set up breeding experiments with *GMR-GAL4* at 30°C, with or without *Dicer2*, to modulate the level of gene expression). A list of all lines used in this study is presented in Table S2.

To study two-locus models, we first generated individual fly stocks with reduced expression for *KCTD13*^{CG10465}, *MAPK3*^{rl}, *PPP4C*^{pp4-19C}, and *DOC2A*^{rph} containing *GMR-GAL4* and *UAS-RNAi* on the same chromosome. We tested to ensure there was adequate *GAL4* to bind

to two independent *UAS* constructs in the two-locus models (Figure S1E). Females from the stocks with constitutively reduced gene expression for each of these four genes were then crossed with other RNAi lines to achieve simultaneous knockdown of two genes in the eye. Overall, we performed 565 pairwise knockdown experiments, including 123 interactions between 16p11.2 homologs, 420 interactions with other neurodevelopmental and CNV genes (selected from ⁴⁴ and ⁸⁰), and 22 validation experiments to test interactions with differentially-expressed genes (Tables S5 and S6).

RNA extraction and quantitative real-time PCR

We assessed mRNA expression by performing quantitative real-time PCR (qRT-PCR) experiments on cDNA samples isolated from fly heads. Briefly, RNAi lines were crossed with *Elav-GAL4* driver at 25°C, and F1 female progeny were collected in groups of 40-50, quickly frozen in liquid nitrogen, and stored at -80°C. For RNA extraction, the heads were separated from their bodies by repetitive cycles of freezing in liquid nitrogen and vortexing. Total RNA was isolated using TRIZOL (Invitrogen), and reverse transcription was performed using qScript cDNA synthesis kit (Quanta Biosciences). RNA was also isolated from fly heads from *GMR-GAL4* crosses for a subset of genes to compare the gene expression with fly heads from *Elav-GAL4* crosses (Figure S1C). Quantitative RT-PCR was performed using an Applied Biosystems Fast 7500 system with SYBR Green PCR master mix (Quanta Biosciences) using optimized protocols. A list of primers used for the qRT-PCR experiments is provided in Table S10.

Quality control

We checked the insertion site of the RNAi constructs to identify and remove any fly lines that may show phenotypes due to insertion-site effects (Figure S1A). While RNAi transgenes for the Bloomington lines are inserted at the attP2 site on chromosome 3L with no expression or effect on the nervous system, thorough analysis of RNAi lines obtained from VDRC stock center was required to rule out off-target effects. We obtained 2 types of lines from VDRC: GD lines, which are P-element-based transgenes with random insertion sites, and KK lines, which are phiC31-based transgenes with defined insertion sites³⁴. In order to rule out any effect of insertion of the RNAi construct in the GD lines, we mapped the insertion site by performing Thermal Asymmetric Interlaced PCR (TAIL-PCR) and Sanger sequencing. The TAIL-PCR method was

modified from a protocol developed in B. Dickson's lab, based on published protocol⁸¹. The first round of PCR was performed with a 1:100 dilution of a genomic DNA preparation with Taq polymerase using three degenerate forward primers (AD1, AD2 and AD3) and a specific reverse primer (T1BUAS) (see Table S10 for TAIL-PCR primers). The second PCR reaction was set up using 1:50 dilution of the first PCR as template, with the AD primer as the forward primer and T2D as the specific reverse primer. The second PCR products were then visualized in 1% agarose gel, followed by gel extraction of the PCR product, Sanger sequencing using the T2En primer, and analysis of the resulting sequence in BLAST. If the insertion site was in the 5'UTR, we only excluded the lines if there was an overexpression of the downstream gene and the phenotype was discordant with another line. In case of KK lines, Green and colleagues demonstrated that the host strain for the KK library has two landing sites: 5' UTR of the *tiptop* gene and a previously non-annotated insertion adjacent to 5'UTR of the *numb* gene (at position chr2L: 9437482, cytological band 30B3)⁸². We observed non-specific shriveled wings in three out of seven KK lines of 16p11.2 homologs with *Elav-GAL4*, and these three lines also showed increased expression of *tiptop* (Table S3). Therefore, we excluded these KK lines from neuronal experiments using *Elav-GAL4*. However, we found that overexpression of *tiptop* (using *UAS-tio*) with *GMR-GAL4* showed a rough eye phenotype and reduced pigmentation confined to the right side of the eye, distinct from the eye phenotypes observed in the KK lines (Figure S1D). Further, we did not observe any changes in the expression of *numb* in the fly lines used in this study (Table S3).

Climbing assay

Fly crosses were set up at 25°C with *Elav-GAL4* to achieve neuronal knockdown. Four genes, *PPP4C^{pp4-19C}*, *ALDOA^{ald}*, *TAOK2^{dTao}*, and *KIF22^{klp68D}*, showed lethality when neuronal expression was reduced using RNAi at 25°C, and therefore were tested at room temperature. *KIF22^{klp68D}* lines were also lethal when raised at room temperature. For each genotype, groups of 10 flies were transferred to a climbing vial and tapped down to the bottom. They were allowed to climb past a line marked at 8 cm from the bottom of the vial, and the number of flies crossing the 8 cm mark at 10 seconds was recorded. For each group, this assay was repeated nine more times with one-minute rest between each trial. These sets of 10 trials for each group were repeated daily for ten days, capturing data from flies aged day 1 to day 10. All experiments were

performed during the same time of the day for consistency of the results. Two-way ANOVA and pairwise two-tailed T tests were used to determine significance for each genotype and day of experiment (Table S11).

Spontaneous seizures assay

Newly eclosed flies of the relevant genotypes were collected and aged for 7 days. Male and female flies were isolated at least 1 day after collection to ensure all females had mated. After aging, flies were transferred individually into the chambers of a 4×5 mating plate using a manual aspirator. The plate was then placed on a standard light box, where the flies were allowed to acclimate for 5 min. Fly behavior was recorded at 30 frames/sec for 5 min using a Canon High Definition Vixia HFM31 Camcorder (resolution 1920 x 1080). Each fly's behavior during the viewing window was then assessed for abrupt, involuntary seizure-associated movements, which manifest as rapid repositioning of the flies within the chamber as previously described³⁶. The total number of flies that exhibited spontaneous seizure events and the number of seizing events per seizing fly was initially assessed in 10-20 flies with each knockdown genotype (Figure S2B), and validated using 5-7 replicates of 20 flies for three select 16p11.2 homologs (Figure 2C). Knockdown lines were compared to controls using one-tailed Mann-Whitney U tests (number of seizures per fly and percentage of seizing flies in replicate experiments) or Fisher's exact test (percentage of seizing flies in experiments without replicates) (Table S11).

Dendritic arborization assays

RNAi lines were crossed to a *UAS-Dicer2*; *ppk-GAL4*, *UAS-mCD8-GFP* driver at 25°C, and embryos were collected at 24 hours on apple juice plates. First instar larvae, eclosed from the embryo, were transferred to the food plate and allowed to age for 48 hours at 25°C before live imaging. Third instar larvae were collected, washed in PBS, and transferred dorsal side up to a glass slide containing a dried agarose pad with a coverslip on top secured with sticky tape. Z-stack images of Class IV Dendritic Arborization neurons were acquired using a Zeiss LSM 800 confocal microscope and processed using ImageJ⁸³ to a scale of 5.0487 pixels/micron. Using an in-house Java plug-in, four concentric circles with a distance of 25 microns between each circle were placed on the images, with the cell body as the center. A manual Sholl analysis was conducted by counting the number of intersections of dendritic branches on each of the

concentric circles. Total and average number of intersections were calculated and normalized to the width of the hemisegment of each sampled neuron to control for slight variation in larval sizes. Two-way ANOVA and pairwise two-tailed T tests were used to determine significance of the number of intersections in each genotype and concentric circle, and two-tailed Mann-Whitney tests were used to determine significance of the total number of intersections (Table S11).

Phenotypic analysis of fly eyes using *Flynotyper*

We used *GMR-GAL4* drivers with and without *Dicer2* to achieve eye-specific knockdown, and imaged 2-3 day old flies using an Olympus BX53 compound microscope with an LMPlanFL N 10X 0.25 NA air objective (Olympus, Tokyo, Japan), at 0.5X magnification and a z-step size of 12.1 μ m. We used CellSens Dimension software (Olympus Optical) to capture the images, and stacked the image slices using Zerene Stacker (Zerene Systems, USA). All eye images presented in the figures are maximum projections of consecutive 20 optical z-sections. Eye area was calculated from each image using ImageJ⁸³. Eye phenotypes were scored manually from rank 1 to 10 based on severity, with rank 1 assigned to wild type-like and rank 10 for the most severe phenotype, as described previously⁴⁴. We developed a computational method called *Flynotyper* (flynotyper.sourceforge.net) that calculates a phenotypic score based on alterations in the hexagonal arrangement of ommatidia in the fly eye⁴⁴. The *Flynotyper* software detects the center of each ommatidium (orange circle), and calculates the phenotypic score based on the number of ommatidia detected, the lengths of six local vectors with direction pointing from each ommatidium to the neighboring ommatidia, and the angle between these six local vectors (Figure 3A (i)). Using *Flynotyper*, we obtained quantitative measures of fly eye roughness with single gene or pairwise gene knockdown. The significance of *Flynotyper* results compared to a GD control was determined using one-tailed or two-tailed Mann-Whitney tests (Table S11). We found no significant differences in *Flynotyper* scores between GD and KK control *Drosophila* lines with and without *Dicer2*, and therefore we used a single control for statistical analysis (Figure S1B). We have previously shown a strong concordance between manual scores and phenotypic scores⁴⁴. In this study, we used manual scoring in conjunction with *Flynotyper*, as certain features such as necrotic patches, glossy eyes, and overall eye size are not detected by *Flynotyper*.

Immunohistochemistry

Neuromuscular synapse (NMJ): Female third instar larvae were dissected in 1.8 mM Ca^{2+} and 4 mM Mg^{2+} saline solution (128 mM NaCl, 2 mM KCl, 1.8 mM Ca^{2+} , 4mM Mg^{2+} , 5 mM Hepes and 36 mM sucrose, pH 7.0) and fixed in saline solution containing 4% paraformaldehyde (PFA) for 30 minutes⁸⁴. The fixed larvae were washed with saline, PBS (13 mM NaCl, 0.7 mM Na_2HPO_4 , and 0.3 mM NaH_2PO_4), and PBT (0.2% Triton X-100 in PBS) for 10 minutes each, incubated with blocking buffer (5% normal goat serum in PBT) for one hour, and then incubated with anti-Dlg (1:500; 4F3, Developmental Studies Hybridoma Bank (DSHB), University of Iowa) overnight at 4°C. These preparations were then washed thrice with PBT and twice with PBS for six minutes each, and incubated with fluorophore-conjugated secondary antibodies, Alexa fluor 568 goat anti-mouse (1:200; A11031, Molecular Probes by Life Technologies), and a plasma membrane marker, Alexa fluor 647-conjugated AffiniPure Goat anti-HRP (1:200; 123-605-021, Jackson ImmunoResearch Laboratories, Inc.), for two hours. Final washes were performed with PBS, five times each for six minutes, and mounted in a 1:1 mixture of PBS and glycerol between two cover slips for imaging.

Larval and pupal eye disc: The eye discs from wandering third instar or 45-hour-old pupae were dissected in PBS and fixed in PBS containing 4% PFA for 20 minutes. The tissues were then washed in PBT, treated with blocking solution for 30 minutes, and then incubated overnight with primary antibodies at 4°C. Mouse anti-phospho-Histone H3 (S10) antibody (1:200; 9706-Cell Signaling Technology), a specific mitotic marker for measuring proliferating cells, and mouse anti-chaoptin (1:200; 24B10, DSHB), a marker for retinal axonal projections, were used for larval eye discs, and mouse anti-Dlg (1:200; 4F3, DSHB), a septate junction marker to visualize and count ommatidial cells, and Rhodamine Phalloidin (1:100; R415, Molecular Probes by Life Technologies), an F-actin marker, were used for observing photoreceptor cells in pupal eyes. These preparations were then washed for 10 minutes thrice with PBT, and incubated with fluorophore-conjugated secondary antibodies (Alexa fluor 568 goat anti-mouse (1:200); A11031 and Alexa fluor 647 goat anti-mouse (1:200); A21236, Molecular Probes by Life Technologies) for two hours. Final washes were performed in PBS, and the tissues were mounted in Prolong Gold antifade reagent with DAPI (Thermo Fisher Scientific, P36930) for imaging.

Bromouridine (BrdU) cell proliferation assay

For BrdU incorporation, the larval eye discs were dissected in PBS and immediately transferred to Schneider media (Sigma). The tissues were then incubated in 10 μ M BrdU (Sigma) at 25°C for 1 hour with constant agitation to allow for incorporation of BrdU into the DNA of replicating cells in S phase. The tissues were washed thrice with PBS for 5 minutes each, and fixed in PBS containing 4% PFA for 20 minutes. The tissues were acid-treated in 2N HCl for 20 minutes to denature DNA. Subsequently, the tissues were neutralized in 100 mM Borax solution for 2 minutes, washed three times with PBT for 10 minutes each, and treated with blocking solution for 1 hour. Then tissues were incubated with mouse anti-BrdU (1:200; DSHB-G3G4) diluted in blocking solution overnight at 4°C. On the following day, the tissues were washed three times in PBT for 20 minutes each and incubated in Alexa fluor-568 Goat anti-mouse (1:200) diluted in 1X PBS, containing 5% normal goat serum, for two hours with constant agitation. Finally, tissues were mounted in Prolong Gold antifade reagent with DAPI.

Confocal Microscopy and image analysis

We acquired Z-stack images of larval eye discs (proliferation assay), pupal eye discs (cellular architecture), and body wall muscles 6 and 7 in the abdominal segments A2 and A3 (NMJ architecture) using an Olympus Fluoview FV1000 laser scanning confocal microscope (Olympus America, Lake Success, NY). Acquisition and processing of images was performed with the Fluoview software (Olympus). We used one or two optical sections for larval and pupal eye disc images, and maximum projections of two or three optical sections were used for NMJ images. For BrdU staining and proliferation (anti-pH3) assays, maximum projections of all optical sections were generated for display. Area, length, perimeter, and number of branches in neuromuscular synapses were calculated using the *Drosophila_NMJ_morphometrics* macro in ImageJ⁸⁵. The bouton counts in each NMJ and pH3-positive cells from larval tissues were counted using the Cell Counter Plug-In within ImageJ⁸³. We also calculated the number of pH3 positive cells using the Analyze particles function in ImageJ, and found a high correlation (Pearson correlation, $r=0.9599$, $p<0.0001$) with counts obtained from Cell Counter Plug-In (Figure S1F). Significance of cell counts or NMJ features from confocal microscopy compared to GD controls was determined using one-tailed or two-tailed Mann-Whitney tests (Table S11).

Differential expression analysis of transcriptome data

We performed RNA sequencing of samples isolated from fly heads of *Elav-GAL4>Dicer2* crosses for *MAPK3^{rl}*, *KCTD13^{CG10465}*, *DOC2A^{rph}*, *CORO1A^{coro}*, *C16ORF53^{pal}*, and *CDIPT^{pis}*, and compared gene expression levels to VDRC control flies carrying the same genetic background. We prepared cDNA libraries for three biological replicates per knockdown model using TruSeq Stranded mRNA LT Sample Prep Kit (Illumina, San Diego, CA), and performed single-end sequencing using Illumina HiSeq 2000 to obtain 100 bp reads at an average coverage of 35.2 million aligned reads/sample. We used FastQC (bioinformatics.babraham.ac.uk/projects/fastqc) and Trimmomatic⁸⁶ for quality control assessment, TopHat2⁸⁷ v.2.1.0 to align the raw sequencing data to the reference fly genome and transcriptome build 6.08, and HTSeq-Count⁸⁸ v.0.6.1 to calculate raw read counts for each gene. edgeR⁸⁹ v.3.16.5 (generalized linear model option) was used to perform differential expression analysis. Genes with a log2-fold change greater than 1 or less than -1, and with a corrected false-discovery rate less than 0.05, were considered as differentially expressed (Table S7). We used the log-fold change in expression to confirm reduced gene expression of each 16p11.2 homolog in the tested RNAi lines. These values were similar to expression values obtained by qPCR; we found a positive correlation between qPCR and RNA-Seq derived expression values for 186 differentially expressed genes across the six knockdown models (Pearson correlation, $r=0.4677$, $p=1.672 \times 10^{-11}$). Human homologs of differentially-expressed fly genes were identified using DIOPT⁷³ v.5.3.

Functional enrichment in differentially expressed genes

We used gene set enrichment analysis to summarize the genome-wide list of genes and their levels of differential expression into biological pathways and processes perturbed by knockdown of 16p11.2 homologs (Figure S7A). First, we used DIOPT⁷³ to identify fly homologs of all annotated genes in each human Gene Ontology Biological Process term⁹⁰. We then calculated Z scores for all GO terms with less than 500 genes (in order to exclude very general GO terms) across the six knockdown models using the Parametric Analysis of Geneset Enrichment procedure⁵⁸. This method averages the log-fold change in expression of all genes in every GO term, and then subtracts the mean and divides by the standard deviation of the log-fold change levels in all genes. The Z-score represents the degree of up- or down-regulation of all genes

within the GO term. We estimated a p-value for each z-score by comparing to the standard normal distribution (two-sided test), and corrected for multiple hypothesis testing using the Benjamini-Hochberg method. 516 GO terms with corrected p-values <0.01 are listed in Table S7. We also used Cytoscape⁹¹ to visualize the network of cell proliferation (GO:0008283) and cell cycle (GO:0007049) genes that were differentially expressed in the knockdown models (Figure S7B).

Analysis of 16p11.2 gene interactions in the context of a human brain-specific gene network

We used a human brain-specific gene interaction network⁶⁰ to further contextualize the observed interactions in 16p11.2 homologs. This network was built using a Bayesian framework that integrated brain-specific signals from genomic data published in over 14,000 publications, as described previously⁶⁰. Within this network, we mapped 49 genes with identified interactions in the fly eye, and calculated the shortest paths between these genes. This procedure identified 428 additional genes in the network that were critical in connecting the 49 assayed genes to each other (Table S8). We then examined these connector genes for enrichment of genes with cell proliferation and cell cycle GO annotations using a one-sided Fisher's exact test.

DATA AVAILABILITY

Gene expression data for the six 16p11.2 homolog model fly lines are publicly available from the GEO (Gene Expression Omnibus) database with accession code GSE100387, and the raw RNA-Sequencing files are publicly available from SRA (Sequence Read Archive) with BioProject accession PRJNA391493.

ACKNOWLEDGEMENTS

We thank T. Mackay, S. Williams, and J. Moore for helpful discussions on the role of epistasis in our interactions, E. Eichler, J. Kumar, F. Hormozdiari, D. Cavener, M. Grotewiel, C. Shashikant, Z-C. Lai, V. Hoxha, and S. Selleck for useful discussions and critical reading of the manuscript. We also thank R. Danjo and R. Pandya for assistance with fly husbandry, I. Albert, A. Sebastian and Q. Li for assistance with RNA-Sequencing data analysis, A. Castells and A. Schenck for help with NMJ morphometrics, and A. Srivastava for technical help. This work was supported by a Basil O'Connor Award from the March of Dimes Foundation (#5-FY14-66), NIH R01-

GM121907, a NARSAD Young Investigator Grant from the Brain and Behavior Research Foundation (22535), and resources from the Huck Institutes of the Life Sciences to S.G., and NIH T32-GM102057 to M.J.

AUTHOR CONTRIBUTIONS

J.I., M.D.S., M.J., and S.G. designed the study. J.I., M.D.S., P.P., L.P., E.H., P.L., K.V., A.K., Q.W., A.T., S.Y., and J.B. performed the experiments. A.T.W. and M.M.R. performed dendritic arborization experiments, and H.K. and J.R.M. performed epilepsy phenotyping. M.J. and A.K. performed network analysis. J.I., M.D.S., M.J., and S.G. analyzed data. J.I., M.J., and S.G. wrote the manuscript with input from all authors.

COMPETING FINANCIAL INTERESTS

The authors declare that no conflicts of interest or competing financial interests exist in relation to this work.

FIGURE LEGENDS

Figure 1. Experimental strategy for identifying neurodevelopmental phenotypes in single-hit and two-hit-interaction models of 16p11.2 homologs.

We identified 14 homologs of 16p11.2 deletion genes in *Drosophila melanogaster* (**Top**), and evaluated global, neurodevelopmental and cellular phenotypes. We also performed transcriptome sequencing and assessed changes in expression of biologically significant genes (**Left**). Next, we identified modifiers of the one-hit eye phenotype for select homologs using two-hit interaction models. A subset of these interactions was further assessed for cellular phenotypes in the two-hit knockdown eyes. We incorporated all fly interactions into a human brain-specific genetic interaction network (**Right**).

Figure 2. Neurodevelopmental defects in flies with knockdown of individual 16p11.2 homologs.

(A) Percentage of 16p11.2 homologs with ubiquitous, eye-specific, wing-specific, and pan-neuronal knockdown at various temperatures that manifest specific phenotypes. (B) Assessment of 16p11.2 homologs for motor defects showed changes in climbing ability over ten days (two-way ANOVA, $p=0.028$, $df=62$, $F=1.61$). Data represented here shows mean \pm standard deviation of 10 independent groups of 10 flies for each line. (C) Assessment of knockdown of 16p11.2 homologs for frequency of spontaneous unprovoked seizure events ($n=5-7$ replicates of 20 fly samples) and average number of seizure events per fly ($n=52-101$ individual flies, Mann-Whitney test, $*p<0.05$). *PPP4C^{pp4-19C}* knockdown was achieved using *Elav-GAL4* and no *Dicer2*, and knockdown of the other two genes and the control used *Elav-GAL4>Dicer2*. (D) Assessment of neuromuscular junction length, synaptic area and bouton numbers for the tested 16p11.2 homologs ($n=4-8$, $*p<0.05$, Mann-Whitney test). Representative confocal fluorescent images (maximum projections of two or three optical sections) of the larval neuromuscular synapses are shown for three homologs. (E) Assessment of dendritic arborization in larvae with knockdown of 16p11.2 homologs, including a box plot of the total number of intersections for all analyzed homologs, calculated by manual Sholl analysis and normalized to width measurement for each given hemisegment to control for slight size variation ($n=9-11$, $*p<0.05$, Mann-Whitney test). Representative confocal live images of class IV da neurons labeled with *mCD8-GFP* under the control of *ppk-GAL4* are shown for two 16p11.2 homologs and control. (F) Assessment of

axonal targeting with knockdown of 16p11.2 homologs. The schematic of the third-instar larval visual system was generated by Sam Kunes⁹² and reprinted with permission from the publisher. Representative confocal images of larval eye discs stained with anti-chaoptin illustrate normal axonal targeting from the retina to the optic lobes of the brain in the control and defects with eye-specific knockdown of *KCTD13*^{CG10465} and *MAPK3*^{rl}.

Figure 3. Cellular phenotypes in the fly eye due to knockdown of individual 16p11.2 homologs.

(A) Schematics and images of the wild-type adult, pupal, and larval eye show the cell organization and structure of the fly eye during development. The wild-type adult eye displays a symmetrical organization of ommatidia, and *Flynotyper* software detects the center of each ommatidium (orange circle) and calculates a phenotypic score based on the length and angle between the ommatidial centers. Illustrations of the wild-type pupal eye show the arrangement of cone cells (C), primary pigment cells (1°), and secondary pigment cells (2°) along the faces of the hexagon, and bristle cells (b) and tertiary pigment cells (3°) at alternating vertices, as well as the eight photoreceptor cells within an ommatidium. The larval imaginal disc schematic shows proliferating cells posterior to the morphogenetic furrow. Pupal eyes were stained with anti-Dlg and phalloidin to visualize ommatidial cells and photoreceptor cells, respectively, while the larval eye was stained with anti-pH3 to visualize proliferating cells. Diagrams of the pupal and larval eye were generated by Frank Pichaud⁹³ and Joan E. Hooper⁹⁴ and are reprinted with permission from the publishers. **(B)** Example images of pupal eyes stained with anti-Dlg illustrate the structure and organization in control and knockdown flies. Circles and arrows indicate differences in cell organization between control and knockdown pupal eyes (yellow circles: cone cell number and organization, white circles: bristle groups, white arrowheads: secondary cells, white arrows: primary cells, yellow arrows: rotation of ommatidia). **(C)** Representative brightfield adult eye images and confocal images of pupal eye and larval eye discs, stained with anti-Dlg and anti-pH3 respectively, of select 16p11.2 homologs illustrate defects in cell proliferation caused by eye-specific knockdown of these homologs. **(D)** Box plot of *Flynotyper* scores for knockdown of 13 homologs of 16p11.2 genes with *GMR-GAL4>Dicer2* (n=7-19, *p<0.05, Mann-Whitney test). *FAM57B*^{CG17841} knockdown displayed pupal lethality with *Dicer2*, and therefore the effect of gene knockdown in further experiments was tested

without *Dicer2*. (E) Box plot of photoreceptor cell count in the pupal eyes of 16p11.2 knockdown flies (n=59-80, *p<0.05, Mann-Whitney test). (F) Table summarizing the cellular defects observed in the pupal eye of 16p11.2 homologs. “+” symbols indicate the severity of the observed cellular defects. (G) Box plot of pH3-positive cell count in the larval eyes of 16p11.2 knockdown flies (n=6-11, *p<0.05, Mann-Whitney test). (H) Box plot of adult eye area in 16p11.2 one-hit knockdown models (n=5-13, *p<0.05, Mann-Whitney test).

Figure 4. Phenotypic and functional consequences of pairwise knockdown of 16p11.2 homologs.

Representative brightfield adult eye images and box plots of *Flyntyper* scores of pairwise knockdown of (A) *MAPK3^{rl}* with other 16p11.2 homologs (n=6-15, *p<0.05, Mann-Whitney test), (B) *KCTD13^{CG10465}* with other 16p11.2 homologs (n=4-14, *p<0.05) and (C) *PPP4C^{pp4-19C}* with other 16p11.2 homologs (n=5-17, *p<0.05). (D) Assessment of axonal targeting in *KCTD13^{CG10465}/CORO1A^{CG14607}* two-hit knockdown flies. Representative confocal images of larval eye discs stained with anti-chaoptin illustrate axonal targeting from the retina to the optic lobes of the brain in eye-specific knockdown of *KCTD13^{CG10465}*, and rescue of these defects with double knockdown of *KCTD13^{CG10465}* and *CORO1A^{CG14607}*. (E) Confocal images of pupal eye and larval eye discs, stained with anti-Dlg and anti-pH3 respectively, for one-hit and two-hit knockdown of 16p11.2 homologs. (F) Table summarizing the cellular defects observed in the pupal eye of one-hit 16p11.2 flies compared to double knockdown of 16p11.2 homologs. “+” symbols indicate the severity of the observed cellular defects, while “Supp” indicates that the cellular defects were suppressed in the two-hit models. (G) Box plot of pH3-positive cell counts in the larval eye discs between one-hit and two-hit knockdowns of 16p11.2 homologs (n=6-13, *p<0.05).

Figure 5. Interactions of 16p11.2 homologs with neurodevelopmental genes.

(A) Heatmap of change in phenotype measures (from manual scoring) in two-hit models of flies with knockdown of 16p11.2 homologs with core neurodevelopmental genes (left) or genes within CNV regions (right). Enhancers (orange) and suppressors (blue) for representative interactions of 16p11.2 homologs are shown. (B) Table summarizing the number of tested interactions of *DOC2A^{rp}*, *PPP4C^{pp4-19C}*, *MAPK3^{rl}* and *KCTD13^{CG10465}* with 50

neurodevelopmental and genes within other CNV regions. Of the 200 tested interactions measured by manual scoring or *Flynotyper*, 46 were identified as suppressors or enhancers of one-hit phenotype, and were validated in multiple RNAi or deficiency lines when available. (C) Representative brightfield adult eye images and box plots of *Flynotyper* scores for simultaneous knockdowns of *KCTD13*^{CG10465}, *MAPK3*^{rl}, *PPP4C*^{pp4-19C}, and *DOC2A*^{rph} with neurodevelopmental genes (n=5-13, *p<0.05, Mann-Whitney test). (D) Representative confocal images of pupal eye and larval eye discs of the *MAPK3*^{rl}/*PTEN*^{dpten} two-hit knockdown flies, stained with anti-Dlg and anti-pH3 respectively. (E) Box plot of photoreceptor cell count in the pupal eye of *MAPK3*^{rl} and *PTEN*^{dpten} one-hit and two-hit flies (n=58-65, p=3.62×10⁻¹⁵ compared to one-hit knockdown of *MAPK3*^{rl}). (F) Box plot of pH3-positive cells in the larval eye between *MAPK3*^{rl} and *PTEN*^{dpten} one-hit and two-hit flies (n=9, p=0.00174 compared to one-hit knockdown of *MAPK3*^{rl}).

Figure 6. Interactions of 16p11.2 homologs within cell proliferation pathways.

Representative brightfield adult eye images and box plots of *Flynotyper* scores for (A) pairwise knockdown of *MAPK3*^{rl} and up-regulated genes identified from transcriptome data (n=6-13, *p<0.05, Mann-Whitney test), and (B) pairwise knockdown of *KCTD13*^{CG10465} and up-regulated genes identified from transcriptome data (n=2-14, *p<0.05). (C) Confocal images of pupal eye and larval eye discs stained with anti-Dlg and anti-pH3, respectively, for *MAPK3*^{rl}/*COX6A2*^{cox6AL} and *KCTD13*^{CG10465}/*RAF1*^{CG14607} two-hit knockdown flies. (D) Box plot of photoreceptor cell counts in *MAPK3*^{rl}/*COX6A2*^{cox6AL} and *KCTD13*^{CG10465}/*RAF1*^{CG14607} two-hit knockdown flies (n=62-68, *p<0.05). (E) Box plot of the number of pH3-positive cells in *MAPK3*^{rl}/*COX6A2*^{cox6AL} and *KCTD13*^{CG10465}/*RAF1*^{CG14607} two-hit knockdown flies (n=12-13, *p<0.05). (F) Assessment of axonal targeting in *MAPK3*^{rl}/*COX6A2*^{cox6AL} and *KCTD13*^{CG10465}/*RAF1*^{CG14607} two-hit knockdowns. Representative confocal images of larval eye discs stained with anti-chaoptin illustrate rescue of axonal targeting defects in the two-locus models (compared to one-hits shown in Figure 2F). (G) A human brain-specific genetic interaction network of all tested 16p11.2 genes and modifier genes, as well as neighboring connector genes. Network nodes with thick borders represent tested genes, with node shape representing gene category. The size of the nodes is proportional to how many connections they have in the network, and the thickness of

the edges is proportional to the number of critical paths in the network using that edge. Purple nodes are genes annotated with cell proliferation or cell cycle GO terms.

Figure 7. A complex interaction model for pathogenicity of rare CNVs. (A) Examples of identifiable interactions from quantitative phenotyping data observed with pairwise knockdown of genes. Blue lines indicate modulation of *GeneB* expression in wild-type flies, while orange lines indicate modulation of *GeneA* expression when *GeneB* is also knocked down. *GeneA* knockdowns that have the same phenotype with or without *GeneB* knockdown indicate no interaction between the two genes (left). Epistatic interactions occur when the change in effect for two-hit knockdown flies compared to *GeneA* knockdown is less severe (suppressor) or more severe (enhancer) than that for *GeneB* knockdown compared to control (center). When the effect of *GeneB* knockdown is the same in wild-type flies and flies with *GeneA* knockdown, the two genes show an additive interaction (right). **(B)** Summary table listing all validated interactions with 16p11.2 genes found using *Flynotyper* screening. For epistatic interactions, blue-colored genes represent suppressors while red-colored genes indicate enhancers of the one-hit phenotype. Bold genes are annotated for cell proliferation/cell cycle GO terms. * indicates observed cell organization/proliferation defects in the developing eye, and † indicates observed axonal targeting defects. **(C)** Knockdown of individual genes within the 16p11.2 region contributes towards various neuronal or developmental phenotypes. However, pairwise knockdown of 16p11.2 genes, or knockdown of 16p11.2 genes with other modifier genes, leads to enhancement, suppression, or rescue of these phenotypes, ultimately resulting to variable phenotypes dependent on the extent of modulation.

REFERENCES

1. Girirajan S, Eichler EE. Phenotypic variability and genetic susceptibility to genomic disorders. *Hum Mol Genet* **19**, R176-187 (2010).
2. Slager RE, Newton TL, Vlangos CN, Finucane B, Elsea SH. Mutations in RAI1 associated with Smith-Magenis syndrome. *Nat Genet* **33**, 466-468 (2003).
3. Pober BR. Williams-Beuren syndrome. *N Engl J Med* **362**, 239-252 (2010).
4. Lindsay EA, *et al.* Tbx1 haploinsufficiency in the DiGeorge syndrome region causes aortic arch defects in mice. *Nature* **410**, 97-101 (2001).
5. Kumar RA, *et al.* Recurrent 16p11.2 microdeletions in autism. *Hum Mol Genet* **17**, 628-638 (2008).
6. Weiss LA, *et al.* Association between microdeletion and microduplication at 16p11.2 and autism. *N Engl J Med* **358**, 667-675 (2008).
7. Bijlsma EK, *et al.* Extending the phenotype of recurrent rearrangements of 16p11.2: deletions in mentally retarded patients without autism and in normal individuals. *Eur J Med Genet* **52**, 77-87 (2009).
8. Mefford HC, *et al.* Genome-wide copy number variation in epilepsy: novel susceptibility loci in idiopathic generalized and focal epilepsies. *PLoS Genet* **6**, e1000962 (2010).
9. Walters RG, *et al.* A new highly penetrant form of obesity due to deletions on chromosome 16p11.2. *Nature* **463**, 671-675 (2010).
10. Iossifov I, *et al.* The contribution of de novo coding mutations to autism spectrum disorder. *Nature* **515**, 216-221 (2014).
11. Gilissen C, *et al.* Genome sequencing identifies major causes of severe intellectual disability. *Nature* **511**, 344-347 (2014).
12. Fromer M, *et al.* De novo mutations in schizophrenia implicate synaptic networks. *Nature* **506**, 179-184 (2014).

13. Epi KC, *et al.* De novo mutations in epileptic encephalopathies. *Nature* **501**, 217-221 (2013).
14. Blumenthal I, *et al.* Transcriptional consequences of 16p11.2 deletion and duplication in mouse cortex and multiplex autism families. *Am J Hum Genet* **94**, 870-883 (2014).
15. Migliavacca E, *et al.* A Potential Contributory Role for Ciliary Dysfunction in the 16p11.2 600 kb BP4-BP5 Pathology. *Am J Hum Genet* **96**, 784-796 (2015).
16. Deshpande A, *et al.* Cellular Phenotypes in Human iPSC-Derived Neurons from a Genetic Model of Autism Spectrum Disorder. *Cell reports* **21**, 2678-2687 (2017).
17. Horev G, *et al.* Dosage-dependent phenotypes in models of 16p11.2 lesions found in autism. *Proc Natl Acad Sci U S A* **108**, 17076-17081 (2011).
18. Portmann T, *et al.* Behavioral abnormalities and circuit defects in the basal ganglia of a mouse model of 16p11.2 deletion syndrome. *Cell reports* **7**, 1077-1092 (2014).
19. Pucilowska J, Vithayathil J, Tavares EJ, Kelly C, Karlo JC, Landreth GE. The 16p11.2 deletion mouse model of autism exhibits altered cortical progenitor proliferation and brain cytoarchitecture linked to the ERK MAPK pathway. *J Neurosci* **35**, 3190-3200 (2015).
20. Arbogast T, *et al.* Reciprocal Effects on Neurocognitive and Metabolic Phenotypes in Mouse Models of 16p11.2 Deletion and Duplication Syndromes. *PLoS Genet* **12**, e1005709 (2016).
21. Escamilla CO, *et al.* Kctd13 deletion reduces synaptic transmission via increased RhoA. *Nature* **551**, 227-231 (2017).
22. Blaker-Lee A, Gupta S, McCammon JM, De Rienzo G, Sive H. Zebrafish homologs of genes within 16p11.2, a genomic region associated with brain disorders, are active during brain development, and include two deletion dosage sensor genes. *Disease models & mechanisms* **5**, 834-851 (2012).
23. Golzio C, *et al.* KCTD13 is a major driver of mirrored neuroanatomical phenotypes of the 16p11.2 copy number variant. *Nature* **485**, 363-367 (2012).

24. McCammon JM, Blaker-Lee A, Chen X, Sive H. The 16p11.2 homologs fam57ba and doc2a generate certain brain and body phenotypes. *Hum Mol Genet*, 1-14 (2017).
25. Andrews T, *et al.* The clustering of functionally related genes contributes to CNV-mediated disease. *Genome Res* **25**, 802-813 (2015).
26. Wangler MF, Yamamoto S, Bellen HJ. Fruit flies in biomedical research. *Genetics* **199**, 639-653 (2015).
27. Wu Y, *et al.* A Drosophila model for Angelman syndrome. *Proc Natl Acad Sci U S A* **105**, 12399-12404 (2008).
28. Cukier HN, Perez AM, Collins AL, Zhou Z, Zoghbi HY, Botas J. Genetic modifiers of MeCP2 function in Drosophila. *PLoS Genet* **4**, e1000179 (2008).
29. Gatto CL, Broadie K. Drosophila modeling of heritable neurodevelopmental disorders. *Curr Opin Neurobiol* **21**, 834-841 (2011).
30. Kochinke K, *et al.* Systematic Phenomics Analysis Deconvolutes Genes Mutated in Intellectual Disability into Biologically Coherent Modules. *Am J Hum Genet* **98**, 149-164 (2016).
31. Shorter J, *et al.* Genetic architecture of natural variation in Drosophila melanogaster aggressive behavior. *Proc Natl Acad Sci U S A* **112**, E3555-3563 (2015).
32. He X, Zhou S, St Armour GE, Mackay TF, Anholt RR. Epistatic partners of neurogenic genes modulate Drosophila olfactory behavior. *Genes Brain Behav* **15**, 280-290 (2016).
33. Grice SJ, Liu JL, Webber C. Synergistic interactions between Drosophila orthologues of genes spanned by de novo human CNVs support multiple-hit models of autism. *PLoS Genet* **11**, e1004998 (2015).
34. Dietzl G, *et al.* A genome-wide transgenic RNAi library for conditional gene inactivation in Drosophila. *Nature* **448**, 151-156 (2007).
35. Zufferey F, *et al.* A 600 kb deletion syndrome at 16p11.2 leads to energy imbalance and neuropsychiatric disorders. *J Med Genet* **49**, 660-668 (2012).

36. Ehaideb SN, *et al.* Mutation of orthologous prickle genes causes a similar epilepsy syndrome in flies and humans. *Annals of clinical and translational neurology* **3**, 695-707 (2016).
37. Penzes P, Cahill ME, Jones KA, VanLeeuwen JE, Woolfrey KM. Dendritic spine pathology in neuropsychiatric disorders. *Nat Neurosci* **14**, 285-293 (2011).
38. Grueber WB, Jan LY, Jan YN. Tiling of the Drosophila epidermis by multidendritic sensory neurons. *Development* **129**, 2867-2878 (2002).
39. Hadjieconomou D, Timofeev K, Salecker I. A step-by-step guide to visual circuit assembly in Drosophila. *Curr Opin Neurobiol* **21**, 76-84 (2011).
40. Kumar JP. Building an ommatidium one cell at a time. *Dev Dyn* **241**, 136-149 (2012).
41. Thomas BJ, Wassarman DA. A fly's eye view of biology. *Trends Genet* **15**, 184-190 (1999).
42. Bilen J, Bonini NM. Genome-wide screen for modifiers of ataxin-3 neurodegeneration in Drosophila. *PLoS Genet* **3**, 1950-1964 (2007).
43. Neufeld TP, Tang AH, Rubin GM. A genetic screen to identify components of the sina signaling pathway in Drosophila eye development. *Genetics* **148**, 277-286 (1998).
44. Iyer J, *et al.* Quantitative Assessment of Eye Phenotypes for Functional Genetic Studies Using Drosophila melanogaster. *G3* **6**, 1427-1437 (2016).
45. Marchetto MC, *et al.* Altered proliferation and networks in neural cells derived from idiopathic autistic individuals. *Mol Psychiatry* **22**, 820-835 (2017).
46. Ernst C. Proliferation and Differentiation Deficits are a Major Convergence Point for Neurodevelopmental Disorders. *Trends Neurosci* **39**, 290-299 (2016).
47. Pinto D, *et al.* Functional impact of global rare copy number variation in autism spectrum disorders. *Nature* **466**, 368-372 (2010).

48. Huang H, *et al.* PTEN affects cell size, cell proliferation and apoptosis during *Drosophila* eye development. *Development* **126**, 5365-5372 (1999).
49. Betancur C, Sakurai T, Buxbaum JD. The emerging role of synaptic cell-adhesion pathways in the pathogenesis of autism spectrum disorders. *Trends Neurosci* **32**, 402-412 (2009).
50. von Kriegsheim A, *et al.* Cell fate decisions are specified by the dynamic ERK interactome. *Nat Cell Biol* **11**, 1458-1464 (2009).
51. Bulgakov OV, Eggenschwiler JT, Hong DH, Anderson KV, Li T. FKBP8 is a negative regulator of mouse sonic hedgehog signaling in neural tissues. *Development* **131**, 2149-2159 (2004).
52. Mackay TF. Epistasis and quantitative traits: using model organisms to study gene-gene interactions. *Nat Rev Genet* **15**, 22-33 (2014).
53. Durak O, *et al.* Chd8 mediates cortical neurogenesis via transcriptional regulation of cell cycle and Wnt signaling. *Nat Neurosci* **19**, 1477-1488 (2016).
54. Bozdagi O, *et al.* Haploinsufficiency of the autism-associated Shank3 gene leads to deficits in synaptic function, social interaction, and social communication. *Molecular autism* **1**, 15 (2010).
55. Bachmann-Gagescu R, *et al.* Recurrent 200-kb deletions of 16p11.2 that include the *SH2B1* gene are associated with developmental delay and obesity. *Genet Med*, (2010).
56. Loviglio MN, *et al.* Chromosomal contacts connect loci associated with autism, BMI and head circumference phenotypes. *Mol Psychiatry* **22**, 836-849 (2017).
57. Crawley JN, Heyer WD, LaSalle JM. Autism and Cancer Share Risk Genes, Pathways, and Drug Targets. *Trends Genet* **32**, 139-146 (2016).
58. Kim SY, Volsky DJ. PAGE: parametric analysis of gene set enrichment. *BMC Bioinformatics* **6**, 144 (2005).

59. Warde-Farley D, *et al.* The GeneMANIA prediction server: biological network integration for gene prioritization and predicting gene function. *Nucleic Acids Res* **38**, W214-220 (2010).
60. Greene CS, *et al.* Understanding multicellular function and disease with human tissue-specific networks. *Nat Genet* **47**, 569-576 (2015).
61. Krishnan A, *et al.* Genome-wide prediction and functional characterization of the genetic basis of autism spectrum disorder. *Nat Neurosci* **19**, 1454-1462 (2016).
62. Zhou J, *et al.* Pharmacological inhibition of mTORC1 suppresses anatomical, cellular, and behavioral abnormalities in neural-specific Pten knock-out mice. *J Neurosci* **29**, 1773-1783 (2009).
63. Imielinski M, *et al.* Oncogenic and sorafenib-sensitive ARAF mutations in lung adenocarcinoma. *J Clin Invest* **124**, 1582-1586 (2014).
64. Lu X, Tang X, Guo W, Ren T, Zhao H. Sorafenib induces growth inhibition and apoptosis of human chondrosarcoma cells by blocking the RAF/ERK/MEK pathway. *J Surg Oncol* **102**, 821-826 (2010).
65. Haller M, Au J, O'Neill M, Lamb DJ. 16p11.2 transcription factor MAZ is a dosage-sensitive regulator of genitourinary development. *Proc Natl Acad Sci U S A* **115**, E1849-E1858 (2018).
66. Parisi MJ, Lin H. The role of the hedgehog/patched signaling pathway in epithelial stem cell proliferation: from fly to human. *Cell Res* **8**, 15-21 (1998).
67. Slack C, Alic N, Foley A, Cabecinha M, Hoddinott MP, Partridge L. The Ras-Erk-ETS-Signaling Pathway Is a Drug Target for Longevity. *Cell* **162**, 72-83 (2015).
68. He H, Tan CK, Downey KM, So AG. A tumor necrosis factor alpha- and interleukin 6-inducible protein that interacts with the small subunit of DNA polymerase delta and proliferating cell nuclear antigen. *Proc Natl Acad Sci U S A* **98**, 11979-11984 (2001).
69. Petrovski S, Wang Q, Heinzen EL, Allen AS, Goldstein DB. Genic intolerance to functional variation and the interpretation of personal genomes. *PLoS Genet* **9**, e1003709 (2013).

70. Lek M, *et al.* Analysis of protein-coding genetic variation in 60,706 humans. *Nature* **536**, 285-291 (2016).
71. Shinawi M, *et al.* Recurrent reciprocal 16p11.2 rearrangements associated with global developmental delay, behavioural problems, dysmorphism, epilepsy, and abnormal head size. *J Med Genet* **47**, 332-341 (2010).
72. Moore JH. A global view of epistasis. *Nat Genet* **37**, 13-14 (2005).
73. Hu Y, *et al.* An integrative approach to ortholog prediction for disease-focused and other functional studies. *BMC Bioinformatics* **12**, 357 (2011).
74. Vilella AJ, Severin J, Ureta-Vidal A, Heng L, Durbin R, Birney E. EnsemblCompara GeneTrees: Complete, duplication-aware phylogenetic trees in vertebrates. *Genome Res* **19**, 327-335 (2009).
75. Chintapalli VR, Wang J, Dow JA. Using FlyAtlas to identify better *Drosophila melanogaster* models of human disease. *Nat Genet* **39**, 715-720 (2007).
76. Wernet MF, Desplan C. Homothorax and Extradenticle alter the transcription factor network in *Drosophila* ommatidia at the dorsal rim of the retina. *Development* **141**, 918-928 (2014).
77. Bharathi V, Pallavi SK, Bajpai R, Emerald BS, Shashidhara LS. Genetic characterization of the *Drosophila* homologue of coronin. *J Cell Sci* **117**, 1911-1922 (2004).
78. Biggs WH, 3rd, *et al.* The *Drosophila* rolled locus encodes a MAP kinase required in the sevenless signal transduction pathway. *EMBO J* **13**, 1628-1635 (1994).
79. Brand AH, Perrimon N. Targeted gene expression as a means of altering cell fates and generating dominant phenotypes. *Development* **118**, 401-415 (1993).
80. Girirajan S, *et al.* Phenotypic heterogeneity of genomic disorders and rare copy-number variants. *N Engl J Med* **367**, 1321-1331 (2012).

81. Liu YG, Whittier RF. Thermal asymmetric interlaced PCR: automatable amplification and sequencing of insert end fragments from P1 and YAC clones for chromosome walking. *Genomics* **25**, 674-681 (1995).
82. Green EW, Fedele G, Giorgini F, Kyriacou CP. A Drosophila RNAi collection is subject to dominant phenotypic effects. *Nat Methods* **11**, 222-223 (2014).
83. Schneider CA, Rasband WS, Eliceiri KW. NIH Image to ImageJ: 25 years of image analysis. *Nat Methods* **9**, 671-675 (2012).
84. Kawasaki F, Mattiuz AM, Ordway RW. Synaptic physiology and ultrastructure in comatose mutants define an in vivo role for NSF in neurotransmitter release. *J Neurosci* **18**, 10241-10249 (1998).
85. Nijhof B, *et al.* A New Fiji-Based Algorithm That Systematically Quantifies Nine Synaptic Parameters Provides Insights into Drosophila NMJ Morphometry. *PLoS Comput Biol* **12**, e1004823 (2016).
86. Bolger AM, Lohse M, Usadel B. Trimmomatic: a flexible trimmer for Illumina sequence data. *Bioinformatics* **30**, 2114-2120 (2014).
87. Kim D, Pertea G, Trapnell C, Pimentel H, Kelley R, Salzberg SL. TopHat2: accurate alignment of transcriptomes in the presence of insertions, deletions and gene fusions. *Genome Biol* **14**, R36 (2013).
88. Anders S, Pyl PT, Huber W. HTSeq--a Python framework to work with high-throughput sequencing data. *Bioinformatics* **31**, 166-169 (2015).
89. Robinson MD, McCarthy DJ, Smyth GK. edgeR: a Bioconductor package for differential expression analysis of digital gene expression data. *Bioinformatics* **26**, 139-140 (2010).
90. Gene Ontology C. Gene Ontology Consortium: going forward. *Nucleic Acids Res* **43**, D1049-1056 (2015).
91. Shannon P, *et al.* Cytoscape: a software environment for integrated models of biomolecular interaction networks. *Genome Res* **13**, 2498-2504 (2003).

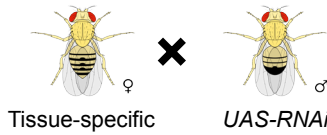
92. Daniele JR, Baqri RM, Kunes S. Analysis of axonal trafficking via a novel live-imaging technique reveals distinct hedgehog transport kinetics. *Biology open* **6**, 714-721 (2017).
93. Fichelson P, Brigui A, Pichaud F. Orthodenticle and Kruppel homolog 1 regulate *Drosophila* photoreceptor maturation. *Proc Natl Acad Sci U S A* **109**, 7893-7898 (2012).
94. Kent D, Bush EW, Hooper JE. Roadkill attenuates Hedgehog responses through degradation of Cubitus interruptus. *Development* **133**, 2001-2010 (2006).

chr. 16 16p13.3 13.2 16p12.3p12.2 p12.1 16p11.2 16q11.2 16q12.1 16q12.2 16q21 16q22.1 16q23.1 23.2 23.3q24.1

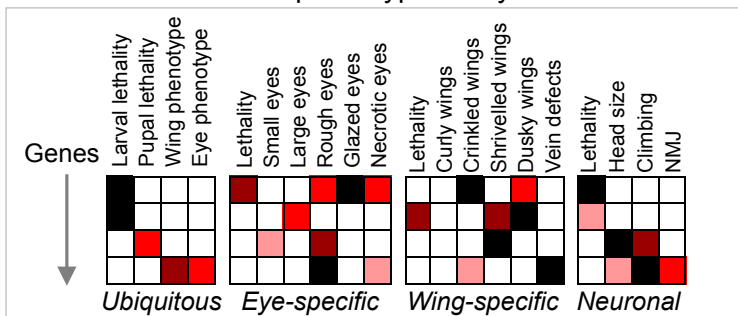
SPN QPRT C16orf54 KIF22 PRRT2 C16ORF53 MVP CDIPT SEZ6L2 ASPHD1 KCTD13 TMEM219 TAOK2 HIRIP3 INO80E DOC2A C16orf92 FAM57B ALDOA PPP4C TBX6 YPEL3 GDDPD3 MAPK3 CORO1A

14 homologs
31 RNAi lines

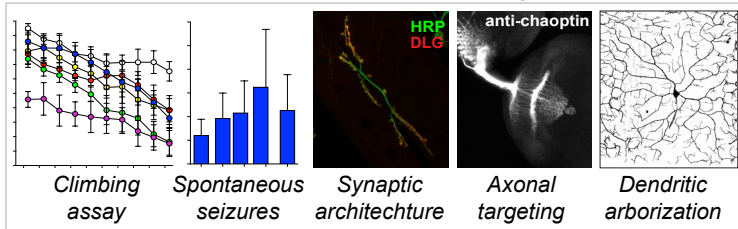
One-hit models



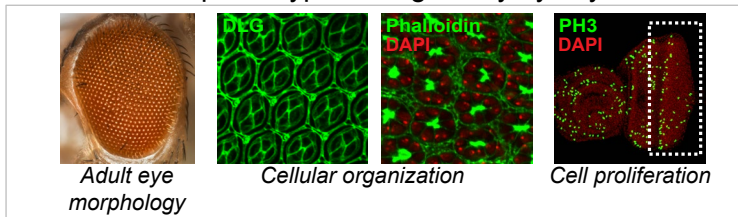
Global phenotypic analysis



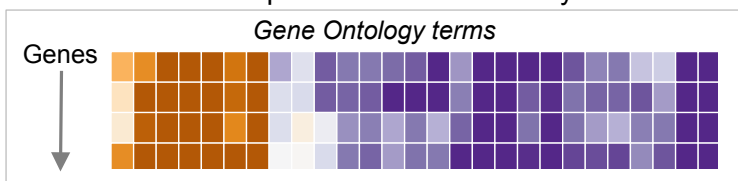
Neurodevelopmental phenotypes



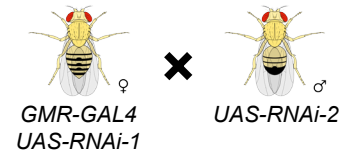
Cellular phenotypes using the fly eye system



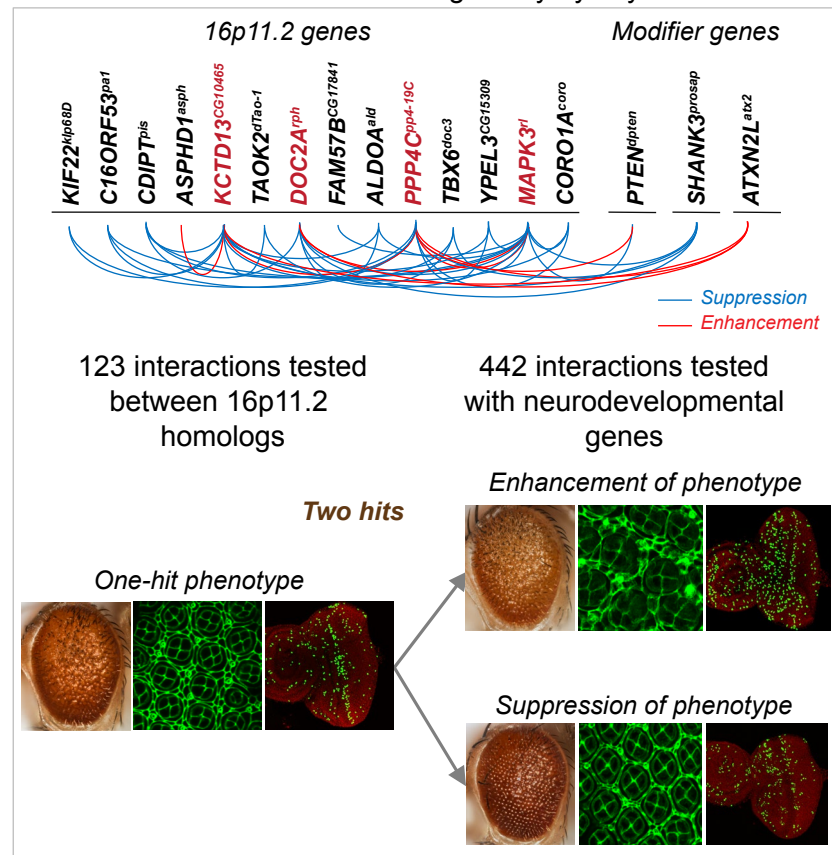
Transcriptome enrichment analysis



Two-hit interaction models



Interaction screens using the fly eye system



Human brain network of fly genetic interactions

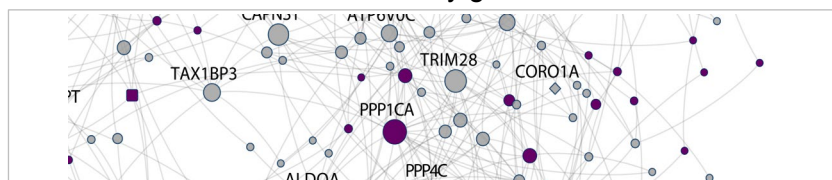


Figure 1. Experimental strategy for identifying neurodevelopmental phenotypes in single-hit and two-hit-interaction models of 16p11.2 homologs.

We identified 14 homologs of 16p11.2 deletion genes in *Drosophila melanogaster* (**Top**), and evaluated global, neurodevelopmental and cellular phenotypes. We also performed transcriptome sequencing and assessed changes in expression of biologically significant genes (**Left**). Next, we identified modifiers of the one-hit eye phenotype for select homologs using two-hit interaction models. A subset of these interactions was further assessed for cellular phenotypes in the two-hit knockdown eyes. We incorporated all fly interactions into a human brain-specific genetic interaction network (**Right**).

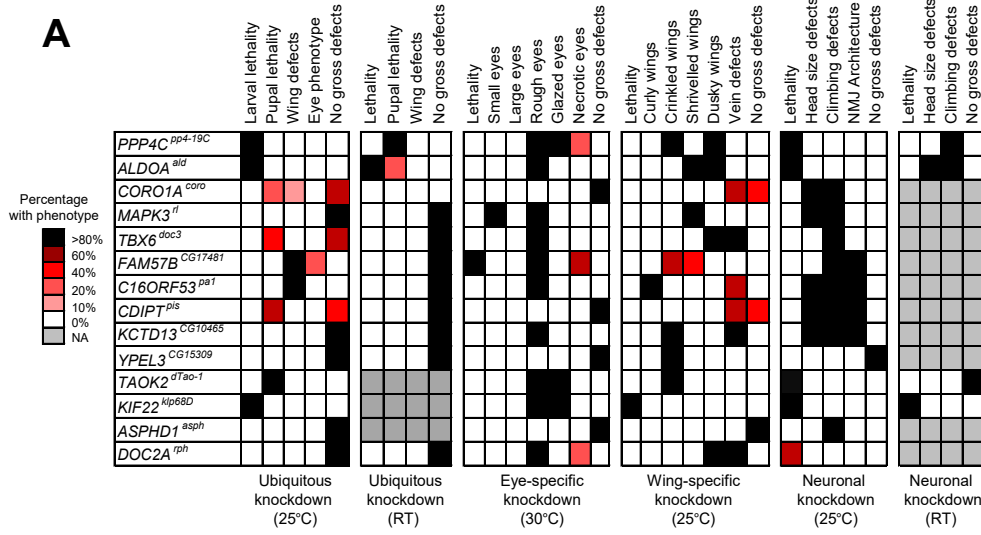
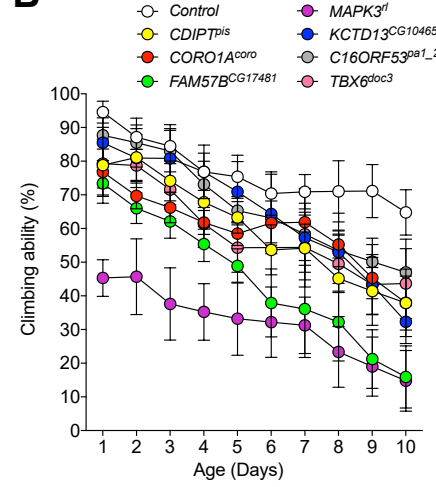
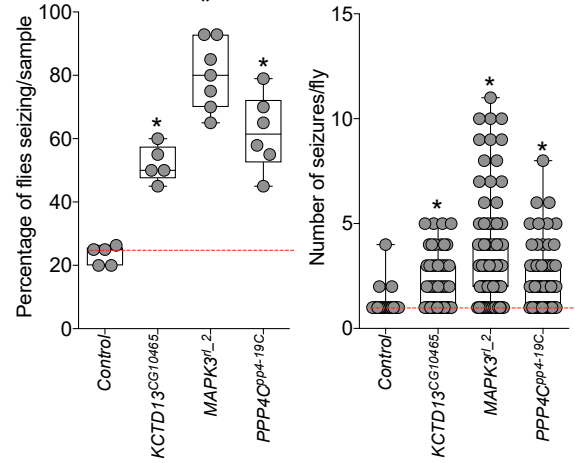
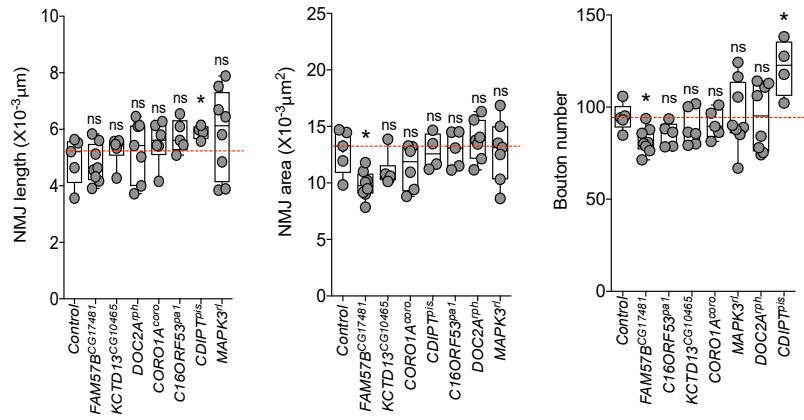
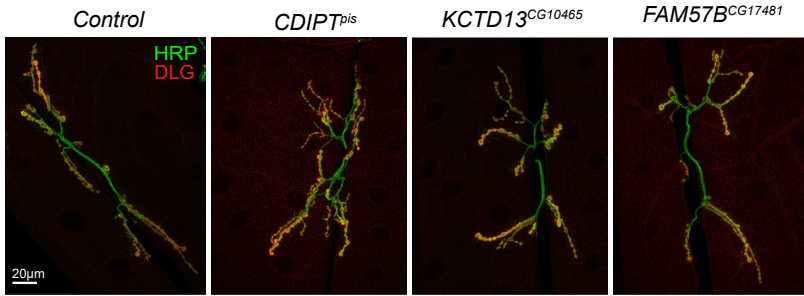
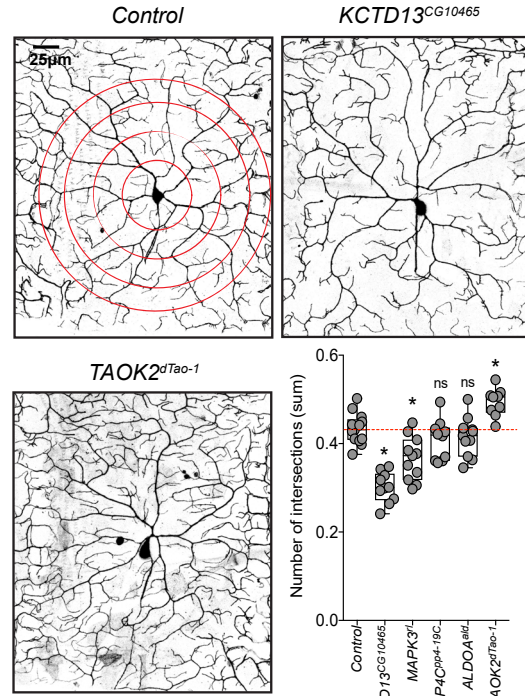
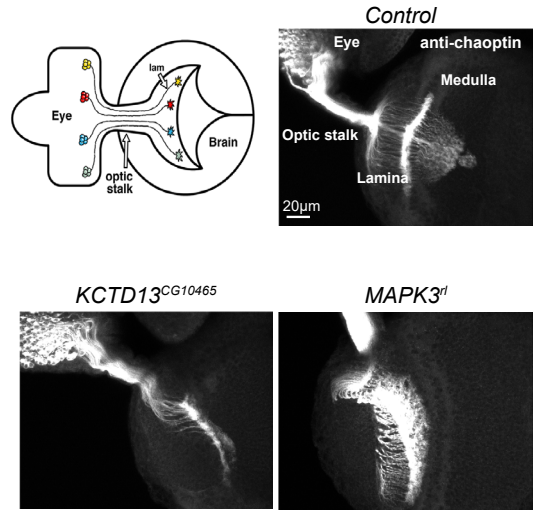
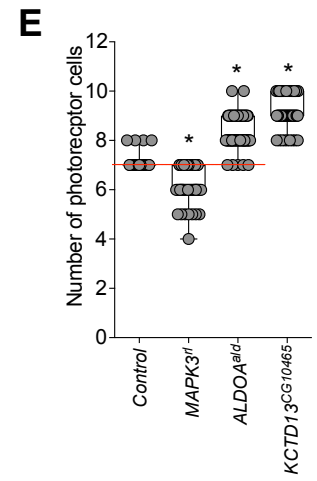
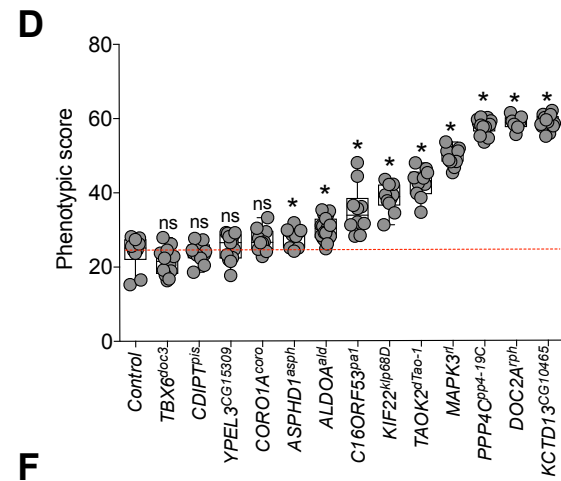
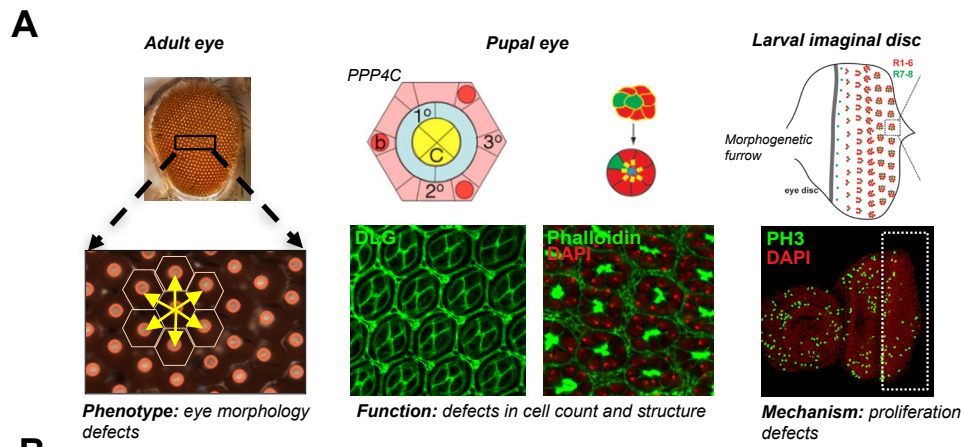
A**B****C****D****E****F**

Figure 2. Neurodevelopmental defects in flies with knockdown of individual 16p11.2 homologs.

(A) Percentage of 16p11.2 homologs with ubiquitous, eye-specific, wing-specific, and pan-neuronal knockdown at various temperatures that manifest specific phenotypes. (B) Assessment of 16p11.2 homologs for motor defects showed changes in climbing ability over ten days (two-way ANOVA, $p=0.028$, $df=62$, $F=1.61$). Data represented here shows mean \pm standard deviation of 10 independent groups of 10 flies for each line. (C) Assessment of knockdown of 16p11.2 homologs for frequency of spontaneous unprovoked seizure events ($n=5-7$ replicates of 20 fly samples) and average number of seizure events per fly ($n=52-101$ individual flies, Mann-Whitney test, $*p<0.05$). *PPP4C^{pp4-19C}* knockdown was achieved using *Elav-GAL4* and no *Dicer2*, and knockdown of the other two genes and the control used *Elav-GAL4>Dicer2*. (D) Assessment of neuromuscular junction length, synaptic area and bouton numbers for the tested 16p11.2 homologs ($n=4-8$, $*p<0.05$, Mann-Whitney test). Representative confocal fluorescent images (maximum projections of two or three optical sections) of the larval neuromuscular synapses are shown for three homologs. (E) Assessment of dendritic arborization in larvae with knockdown of 16p11.2 homologs, including a box plot of the total number of intersections for all analyzed homologs, calculated by manual Sholl analysis and normalized to width measurement for each given hemisegment to control for slight size variation ($n=9-11$, $*p<0.05$, Mann-Whitney test). Representative confocal live images of class IV da neurons labeled with *mCD8-GFP* under the control of *ppk-GAL4* are shown for two 16p11.2 homologs and control. (F) Assessment of axonal targeting with knockdown of 16p11.2 homologs. The schematic of the third-instar larval visual system was generated by Sam Kunes⁹⁴ and reprinted with permission from the publisher. Representative confocal images of larval eye discs stained with anti-chaoptin illustrate normal axonal targeting from the retina to the optic lobes of the brain in the control and defects with eye-specific knockdown of *KCTD13^{CG10465}* and *MAPK3^{rl}*.



F

Gene	Cone cell	Primary cell	Bristle group	Secondary cell	Tertiary cell	Rotation	Hexagon Structure
FAM57B ^{CG17481}	+++	++	++	+	+	+	+++
KCTD13 ^{CG10465}	+++	+	++	++	+	+	++
DOC2A ^{rph}	++	+	++	++	+	+	++
PPP4C ^{p4-19C}	++	++	++	++	++	+	+++
MAPK3 ^{rl}		+	+	++	+	+	+
TAOK2 ^{dTao-1}	++	+	++	++		+	++
C16ORF53 ^{pa1}			+	+			+
ALDOA ^{ald}	++		+	++		+	
CORO1A ^{coro}	+		+	+			+
CDIPT ^{pis}							

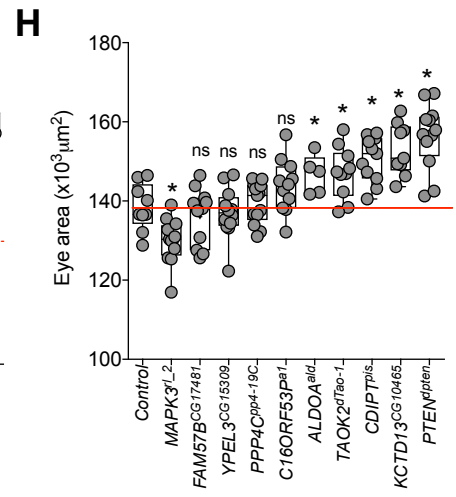
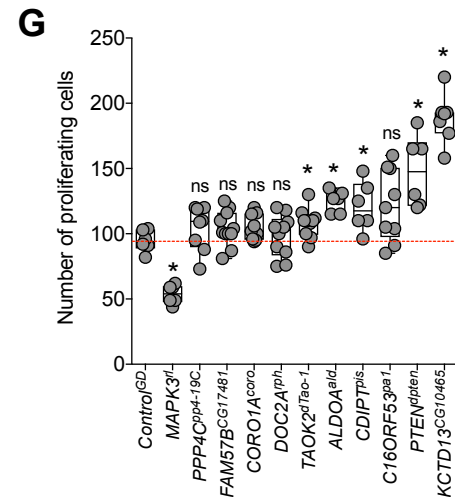
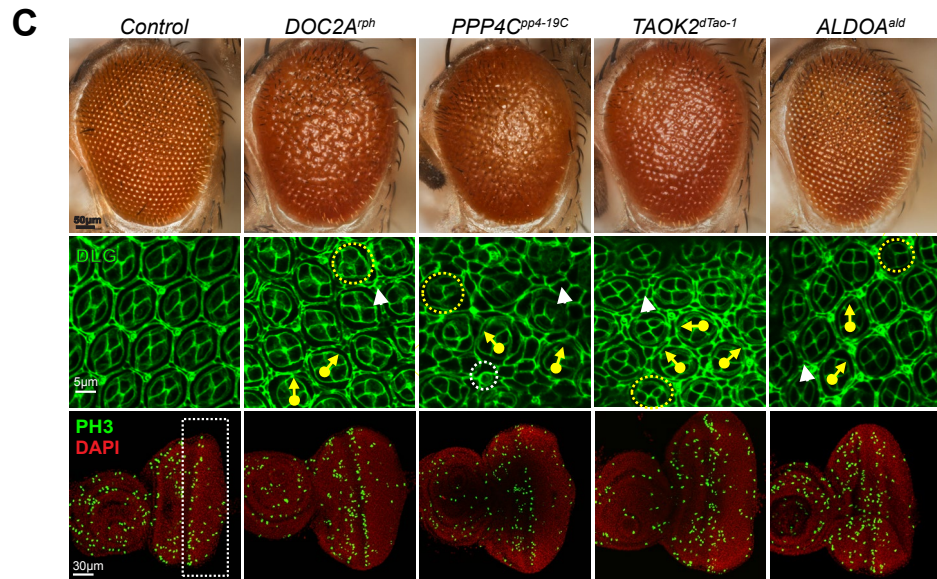
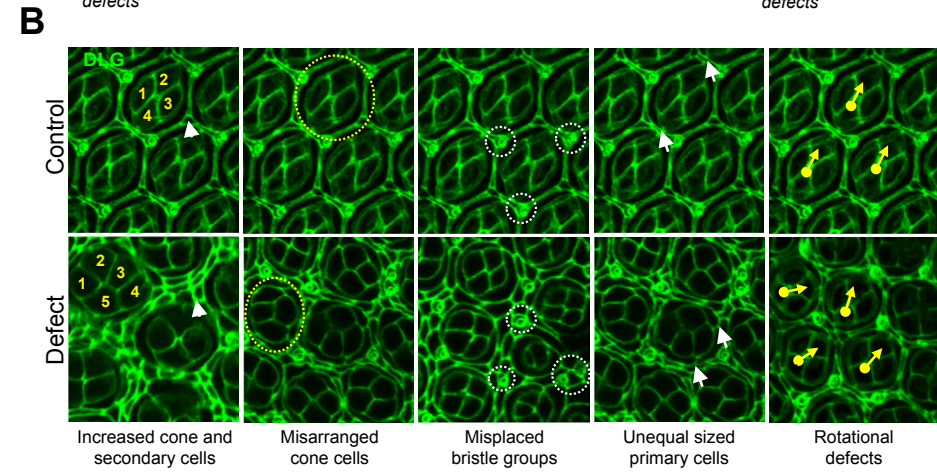
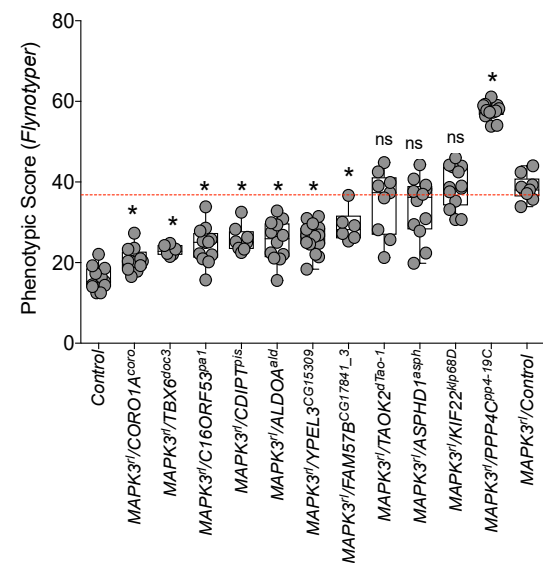
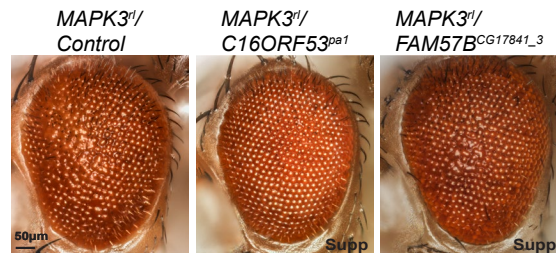
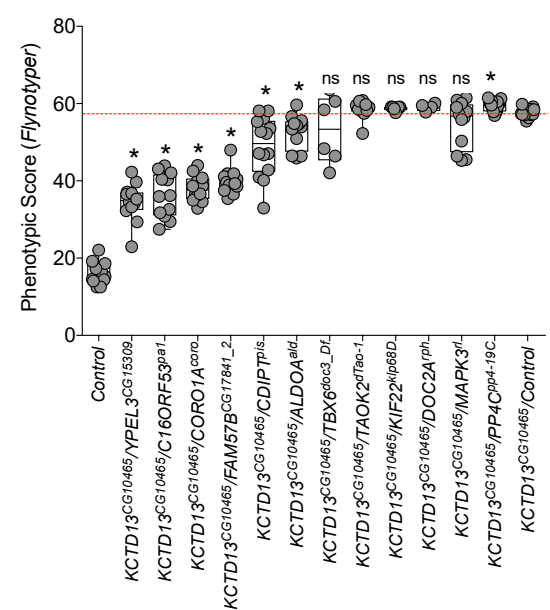
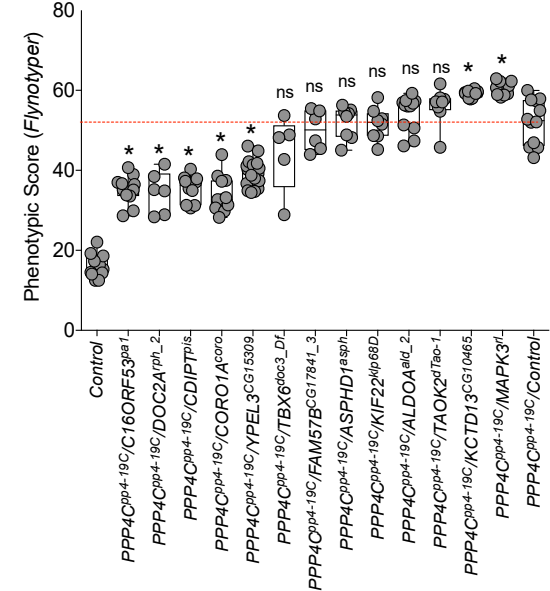
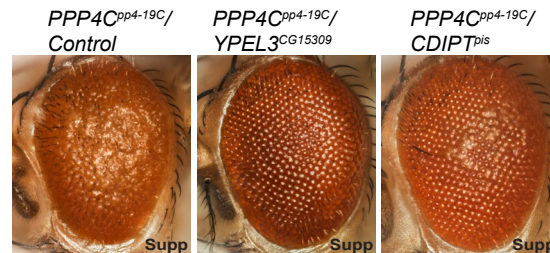
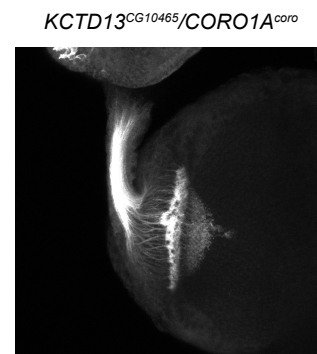
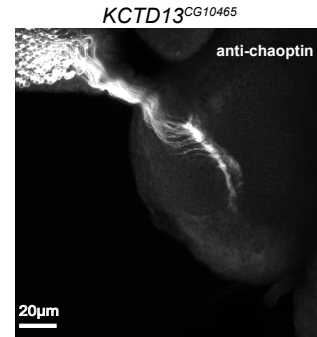
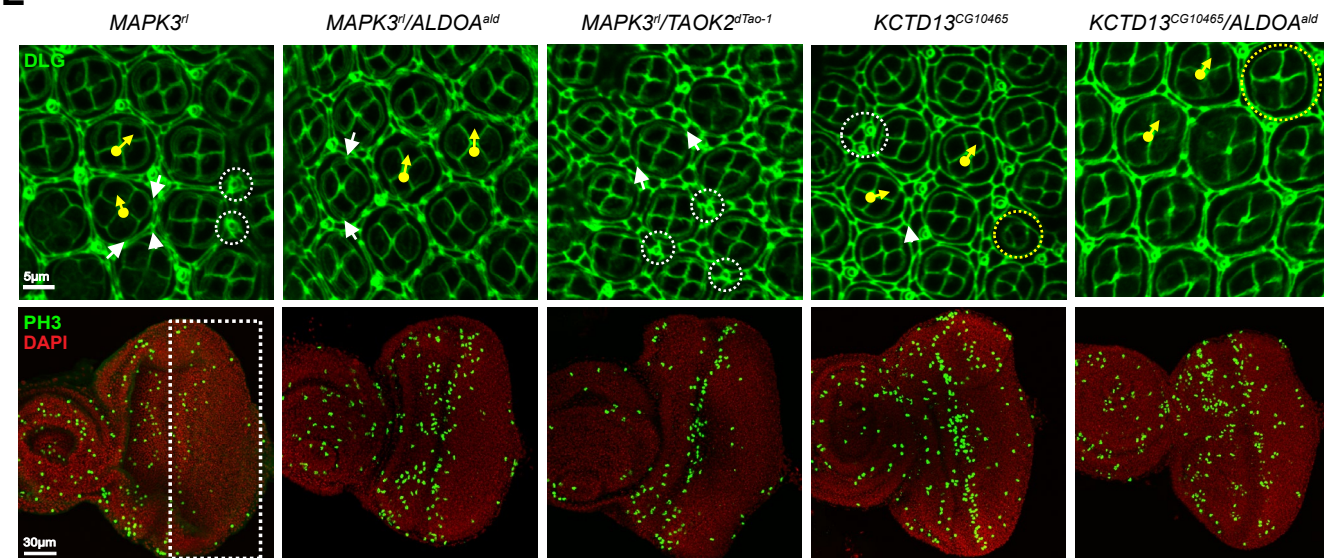


Figure 3. Cellular phenotypes in the fly eye due to knockdown of individual 16p11.2 homologs.

(A) Schematics and images of the wild-type adult, pupal, and larval eye show the cell organization and structure of the fly eye during development. The wild-type adult eye displays a symmetrical organization of ommatidia, and *Flynotyper* software detects the center of each ommatidium (orange circle) and calculates a phenotypic score based on the length and angle between the ommatidial centers. Illustrations of the wild-type pupal eye show the arrangement of cone cells (C), primary pigment cells (1°), and secondary pigment cells (2°) along the faces of the hexagon, and bristle cells (b) and tertiary pigment cells (3°) at alternating vertices, as well as the eight photoreceptor cells within an ommatidium. The larval imaginal disc schematic shows proliferating cells posterior to the morphogenetic furrow. Pupal eyes were stained with anti-Dlg and phalloidin to visualize ommatidial cells and photoreceptor cells, respectively, while the larval eye was stained with anti-pH3 to visualize proliferating cells. Diagrams of the pupal and larval eye were generated by Frank Pichaud⁹⁵ and Joan E. Hooper⁹⁶ and are reprinted with permission from the publishers. (B) Example images of pupal eyes stained with anti-Dlg illustrate the structure and organization in control and knockdown flies. Circles and arrows indicate differences in cell organization between control and knockdown pupal eyes (yellow circles: cone cell number and organization, white circles: bristle groups, white arrowheads: secondary cells, white arrows: primary cells, yellow arrows: rotation of ommatidia). (C) Representative brightfield adult eye images and confocal images of pupal eye and larval eye discs, stained with anti-Dlg and anti-pH3 respectively, of select 16p11.2 homologs illustrate defects in cell proliferation caused by eye-specific knockdown of these homologs. (D) Box plot of *Flynotyper* scores for knockdown of 13 homologs of 16p11.2 genes with *GMR-GAL4>Dicer2* (n=7-19, *p<0.05, Mann-Whitney test). *FAM57B^{CG17841}* knockdown displayed pupal lethality with *Dicer2*, and therefore the effect of gene knockdown in further experiments was tested without *Dicer2*. (E) Box plot of photoreceptor cell count in the pupal eyes of 16p11.2 knockdown flies (n=59-80, *p<0.05, Mann-Whitney test). (F) Table summarizing the cellular defects observed in the pupal eye of 16p11.2 homologs. “+” symbols indicate the severity of the observed cellular defects. (G) Box plot of pH3-positive cell count in the larval eyes of 16p11.2 knockdown flies (n=6-11, *p<0.05, Mann-Whitney test). (H) Box plot of adult eye area in 16p11.2 one-hit knockdown models (n=5-13, *p<0.05, Mann-Whitney test).

A**B****C****D****E****F**

	Cone cell defects	Primary cell defects	Secondary cell defects	Rotation defects
<i>MAPK3</i> ^{+/+}		+	+	+
<i>MAPK3</i> ^{+/+} / <i>ALDOA</i> ^{ald}		Supp	+	Supp
<i>MAPK3</i> ^{+/+} / <i>TAOK2</i> ^{dTao-1}		Supp	+	+
<i>KCTD13</i> ^{CG10465}	++	+	++	+
<i>KCTD13</i> ^{CG10465} / <i>ALDOA</i> ^{ald}	Supp	Supp	Supp	Supp
<i>KCTD13</i> ^{CG10465} / <i>TAOK2</i> ^{dTao-1}	Supp	Supp	++	+

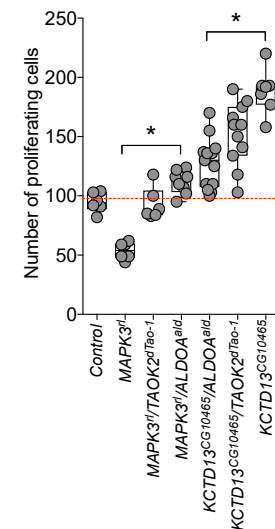
G

Figure 4. Phenotypic and functional consequences of pairwise knockdown of 16p11.2 homologs.

Representative brightfield adult eye images and box plots of *Flynotyper* scores of pairwise knockdown of (A) *MAPK3^{rl}* with other 16p11.2 homologs (n=6-15, *p<0.05, Mann-Whitney test), (B) *KCTD13^{CG10465}* with other 16p11.2 homologs (n=4-14, *p<0.05) and (C) *PPP4C^{pp4-19C}* with other 16p11.2 homologs (n=5-17, *p<0.05). (D) Assessment of axonal targeting in *KCTD13^{CG10465}/CORO1A^{CG14607}* two-hit knockdown flies. Representative confocal images of larval eye discs stained with anti-chaoptin illustrate axonal targeting from the retina to the optic lobes of the brain in eye-specific knockdown of *KCTD13^{CG10465}*, and rescue of these defects with double knockdown of *KCTD13^{CG10465}* and *CORO1A^{CG14607}*. (E) Confocal images of pupal eye and larval eye discs, stained with anti-Dlg and anti-pH3 respectively, for one-hit and two-hit knockdown of 16p11.2 homologs. (F) Table summarizing the cellular defects observed in the pupal eye of one-hit 16p11.2 flies compared to double knockdown of 16p11.2 homologs. “+” symbols indicate the severity of the observed cellular defects, while “Supp” indicates that the cellular defects were suppressed in the two-hit models. (G) Box plot of pH3-positive cell counts in the larval eye discs between one-hit and two-hit knockdowns of 16p11.2 homologs (n=6-13, *p<0.05).

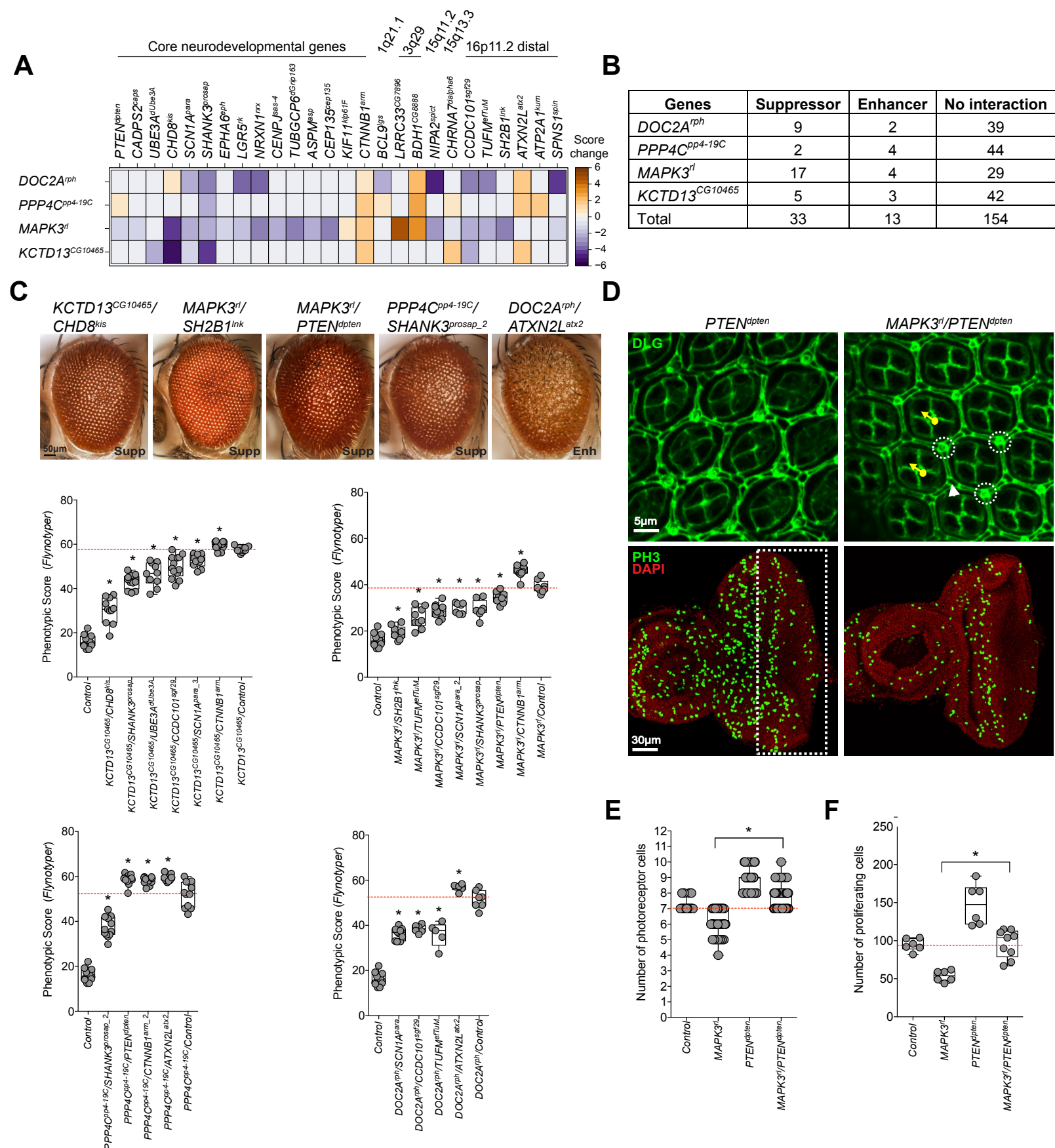


Figure 5. Interactions of 16p11.2 homologs with neurodevelopmental genes.

(A) Heatmap of change in phenotype measures (from manual scoring) in two-hit models of flies with knockdown of 16p11.2 homologs with core neurodevelopmental genes (left) or genes within CNV regions (right). Enhancers (orange) and suppressors (blue) for representative interactions of 16p11.2 homologs are shown. **(B)** Table summarizing the number of tested interactions of *DOC2A^{rph}*, *PPP4C^{pp4-19C}*, *MAPK3^{rl}* and *KCTD13^{CG10465}* with 50 neurodevelopmental and genes within other CNV regions. Of the 200 tested interactions measured by manual scoring or *Flynotyper*, 46 were identified as suppressors or enhancers of one-hit phenotype, and were validated in multiple RNAi or deficiency lines when available. **(C)** Representative brightfield adult eye images and box plots of *Flynotyper* scores for simultaneous knockdowns of *KCTD13^{CG10465}*, *MAPK3^{rl}*, *PPP4C^{pp4-19C}*, and *DOC2A^{rph}* with neurodevelopmental genes (n=5-13, *p<0.05, Mann-Whitney test). **(D)** Representative confocal images of pupal eye and larval eye discs of the *MAPK3^{rl}/PTEN^{dpten}* two-hit knockdown flies, stained with anti-Dlg and anti-pH3 respectively. **(E)** Box plot of photoreceptor cell count in the pupal eye of *MAPK3^{rl}* and *PTEN^{dpten}* one-hit and two-hit flies (n=58-65, p=3.62×10⁻¹⁵ compared to one-hit knockdown of *MAPK3^{rl}*). **(F)** Box plot of pH3-positive cells in the larval eye between *MAPK3^{rl}* and *PTEN^{dpten}* one-hit and two-hit flies (n=9, p=0.00174 compared to one-hit knockdown of *MAPK3^{rl}*).

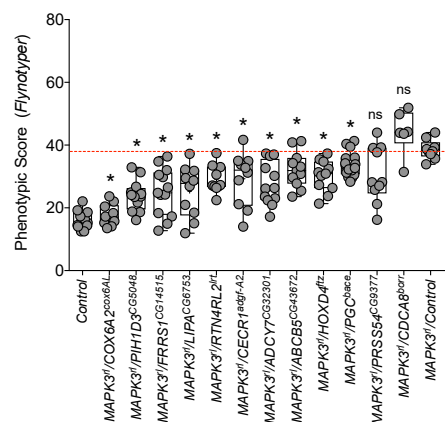
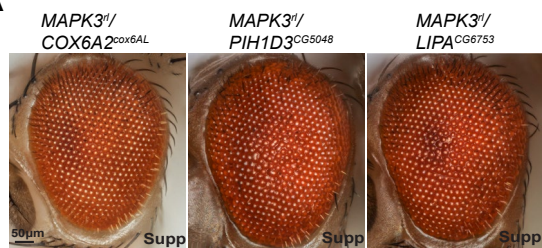
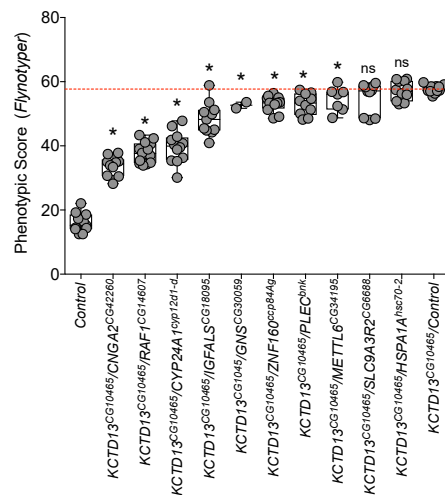
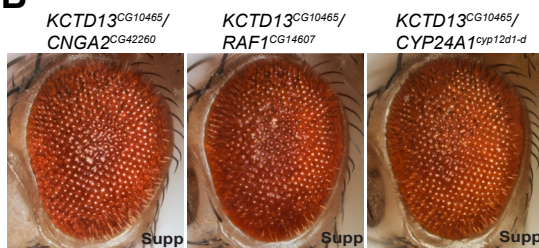
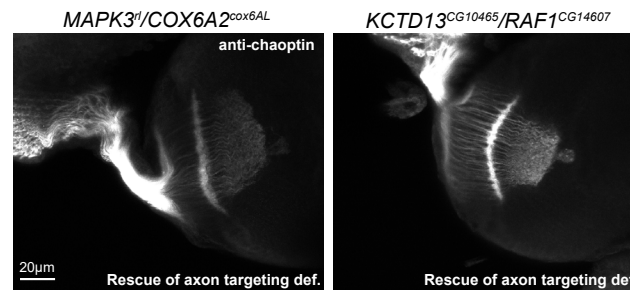
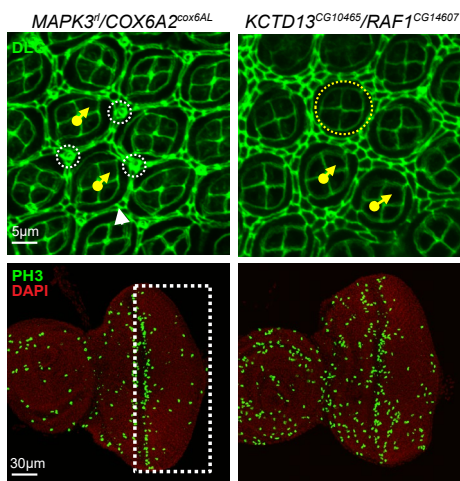
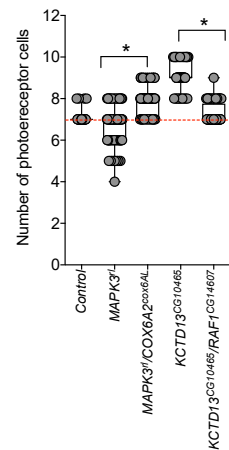
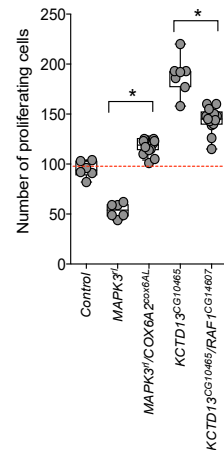
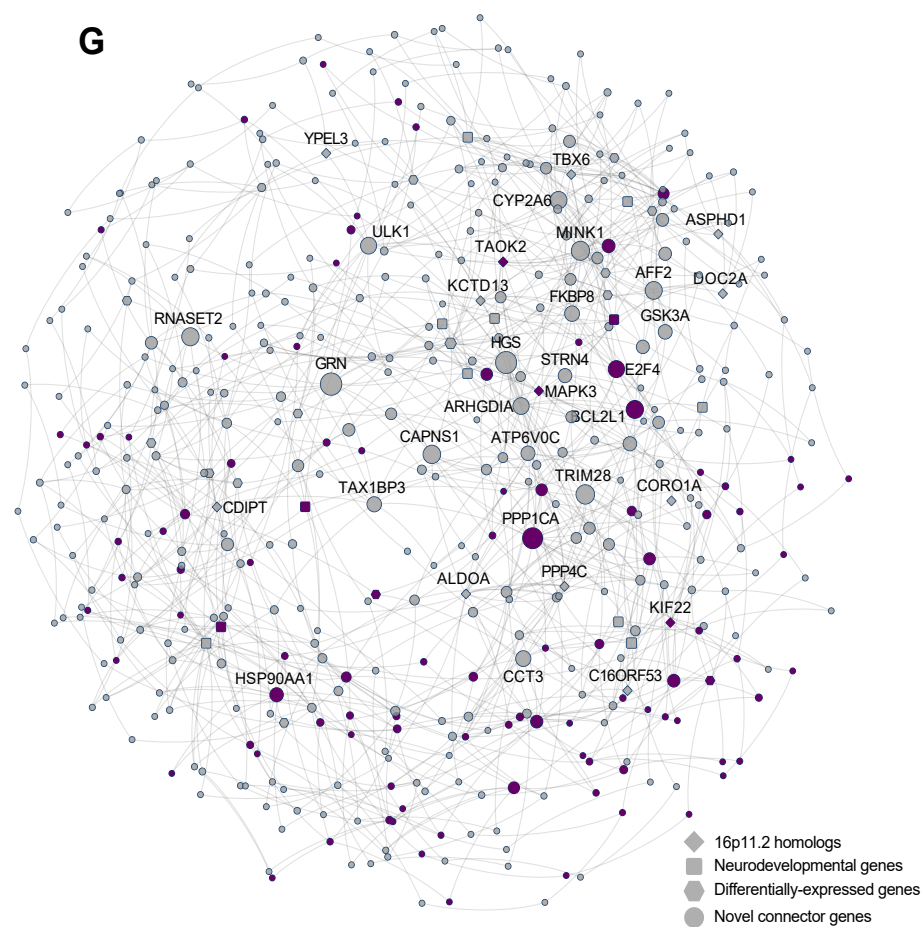
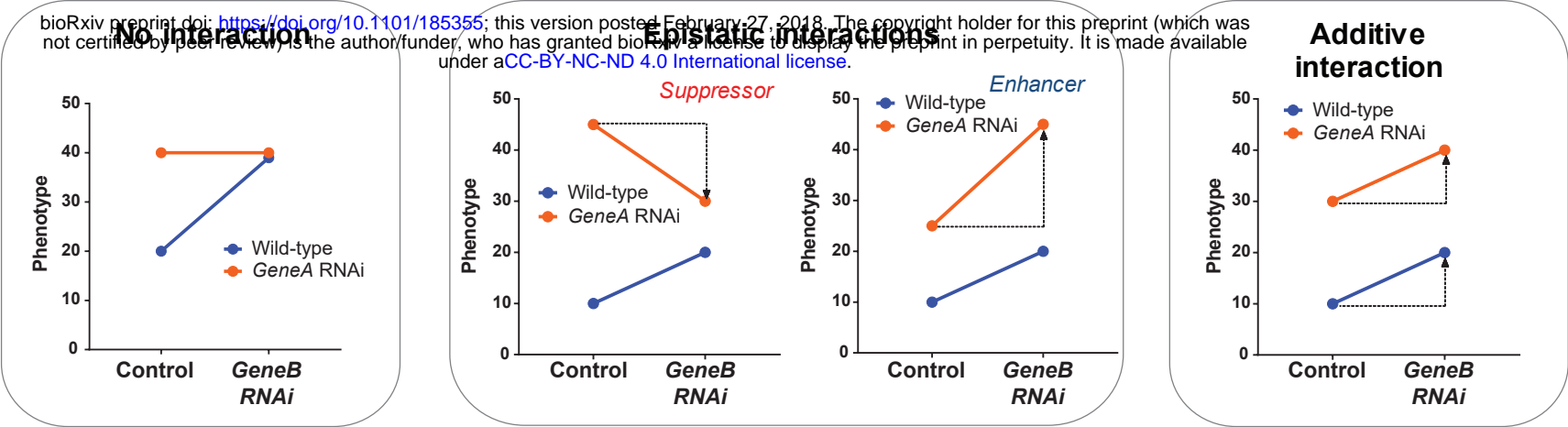
A**B****F****C****D****E****G**

Figure 6. Interactions of 16p11.2 homologs within cell proliferation pathways.

Representative brightfield adult eye images and box plots of *Flynotyper* scores for (A) pairwise knockdown of *MAPK3^{rl}* and up-regulated genes identified from transcriptome data (n=6-13, *p<0.05, Mann-Whitney test), and (B) pairwise knockdown of *KCTD13^{CG10465}* and up-regulated genes identified from transcriptome data (n=2-14, *p<0.05). (C) Confocal images of pupal eye and larval eye discs stained with anti-Dlg and anti-pH3, respectively, for *MAPK3^{rl}/COX6A2^{cox6AL}* and *KCTD13^{CG10465}/RAF1^{CG14607}* two-hit knockdown flies. (D) Box plot of photoreceptor cell counts in *MAPK3^{rl}/COX6A2^{cox6AL}* and *KCTD13^{CG10465}/RAF1^{CG14607}* two-hit knockdown flies (n=62-68, *p<0.05). (E) Box plot of the number of pH3-positive cells in *MAPK3^{rl}/COX6A2^{cox6AL}* and *KCTD13^{CG10465}/RAF1^{CG14607}* two-hit knockdown flies (n=12-13, *p<0.05). (F) Assessment of axonal targeting in *MAPK3^{rl}/COX6A2^{cox6AL}* and *KCTD13^{CG10465}/RAF1^{CG14607}* two-hit knockdowns. Representative confocal images of larval eye discs stained with anti-chaoptin illustrate rescue of axonal targeting defects in the two-locus models (compared to one-hits shown in Figure 2F). (G) A human brain-specific genetic interaction network of all tested 16p11.2 genes and modifier genes, as well as neighboring connector genes. Network nodes with thick borders represent tested genes, with node shape representing gene category. The size of the nodes is proportional to how many connections they have in the network, and the thickness of the edges is proportional to the number of critical paths in the network using that edge. Purple nodes are genes annotated with cell proliferation or cell cycle GO terms.

A



B

	Total interactions		Epistatic interactions			Additive interactions	
	Tested	Validated	16p11.2 genes	Neurodevelopmental genes	RNA-Seq targets	16p11.2 genes	Neurodevelopmental genes
KCTD13	45	23	7: C16orf53 , <i>CDIPT</i> , <i>FAM57B</i> , CORO1A [†] , <i>ALDOA</i> [†] , <i>YPEL3</i> , PPP4C	5: <i>CCDC101</i> , <i>UBE3A</i> , <i>CHD8</i> , <i>SCN1A</i> , <i>SHANK3</i>	8: <i>CNGA2</i> , RAF1 [†] , <i>CYP24A1</i> , <i>IGFALS</i> , <i>GNS</i> , <i>ZNF160</i> , <i>PLEC</i> , <i>METTL6</i>	0	3: <i>ATXN2L</i> , CTNNB1 , CHRNA7
MAPK3	47	39	7: C16orf53 , <i>CDIPT</i> , <i>FAM57B</i> , CORO1A , <i>ALDOA</i> [*] , <i>YPEL3</i> , <i>TBX6</i>	18: <i>CCDC101</i> , <i>TUFM</i> , SH2B1 , <i>SPNS1</i> , PTEN [*] , <i>CHD8</i> , <i>SCN1A</i> , <i>SHANK3</i> , <i>EPHA6</i> , LGR5 , <i>NRXN1</i> , CEP135 , CENPJ , TUBGCP6 , ASPM , <i>NIPA2</i> , CHRNA7 , CTNNB1	10: <i>COX6A2</i> [†] , <i>PIH1D3</i> , <i>FRRS1</i> , LIPA , <i>RTN4RL2</i> , <i>CECR1</i> , <i>ADCY7</i> , <i>ABCB5</i> , <i>HIXD4</i> , <i>PGC</i>	1: PPP4C	3: KIF11 , <i>LRRC33</i> , <i>BDH1</i>
PPP4C	37	13	6: C16orf53 , <i>CDIPT</i> , CORO1A , <i>DOC2A</i> , <i>YPEL3</i> , KCTD13	2: <i>SHANK3</i> , CHRNA7	--	1: MAPK3	4: <i>ATXN2L</i> , <i>ATP2A1</i> , PTEN , CTNNB1
DOC2A	37	13	2: <i>CDIPT</i> , <i>ALDOA</i>	9: <i>CCDC101</i> , <i>TUFM</i> , <i>SPNS1</i> , <i>SCN1A</i> , <i>SHANK3</i> , LGR5 , <i>NRXN1</i> , <i>NIPA2</i> , <i>BCL9</i>	--	0	2: <i>ATXN2L</i> , CTNNB1

C

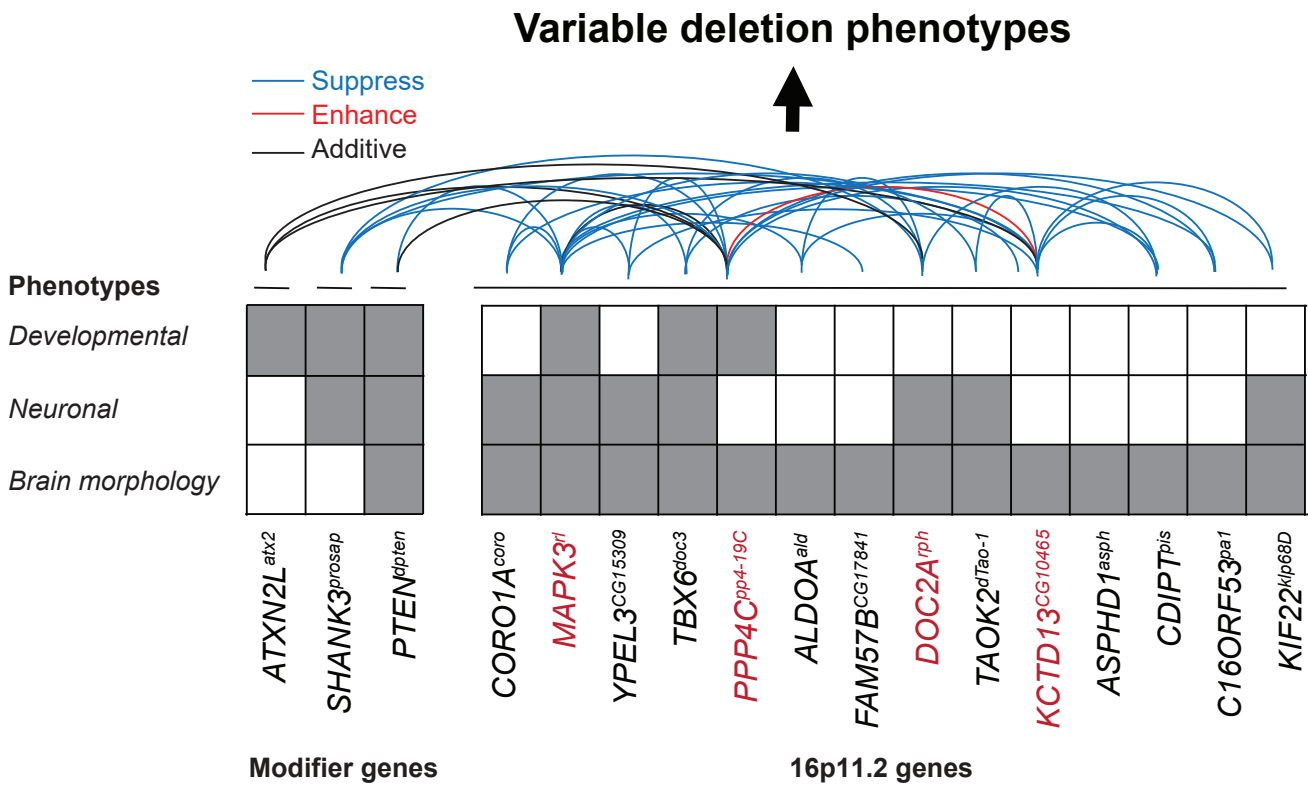


Figure 7. A complex interaction model for pathogenicity of rare CNVs. (A) Examples of identifiable interactions from quantitative phenotyping data observed with pairwise knockdown of genes. Blue lines indicate modulation of *GeneB* expression in wild-type flies, while orange lines indicate modulation of *GeneA* expression when *GeneB* is also knocked down. *GeneA* knockdowns that have the same phenotype with or without *GeneB* knockdown indicate no interaction between the two genes (left). Epistatic interactions occur when the change in effect for two-hit knockdown flies compared to *GeneA* knockdown is less severe (suppressor) or more severe (enhancer) than that for *GeneB* knockdown compared to control (center). When the effect of *GeneB* knockdown is the same in wild-type flies and flies with *GeneA* knockdown, the two genes show an additive interaction (right). **(B)** Summary table listing all validated interactions with 16p11.2 genes found using *Flynotyper* screening. For epistatic interactions, blue-colored genes represent suppressors while red-colored genes indicate enhancers of the one-hit phenotype. Bold genes are annotated for cell proliferation/cell cycle GO terms. * indicates observed cell organization/proliferation defects in the developing eye, and † indicates observed axonal targeting defects. **(C)** Knockdown of individual genes within the 16p11.2 region contributes towards various neuronal or developmental phenotypes. However, pairwise knockdown of 16p11.2 genes, or knockdown of 16p11.2 genes with other modifier genes, leads to enhancement, suppression, or rescue of these phenotypes, ultimately resulting to variable phenotypes dependent on the extent of modulation.

Pervasive epistasis modulates neurodevelopmental defects of the autism-associated 16p11.2 deletion

Janani Iyer^{1,9}, Mayanglambam Dhruba Singh^{1,9}, Matthew Jensen^{1,2,9}, Payal Patel^{1,9}, Lucilla Pizzo¹, Emily Huber¹, Haley Koerselman³, Alexis T. Weiner¹, Paola Lepanto⁴, Komal Vadodaria¹, Alexis Kubina¹, Qingyu Wang^{1,2}, Abigail Talbert¹, Sneha Yennawar¹, Jose Badano⁴, J. Robert Manak^{3,5}, Melissa M. Rolls¹, Arjun Krishnan^{6,7}, and Santhosh Girirajan^{1,2,8*}

Table of Contents

SUPPLEMENTARY FIGURES.....	3
Figure S1. Quality control of fly RNAi knockdown lines.	3
Figure S2. Neurodevelopmental defects in flies with knockdown of individual 16p11.2 homologs.....	5
Figure S3. Adult eye phenotypes of one-hit knockdown models of 16p11.2 homologs.....	7
Figure S4. Cellular eye phenotypes of one-hit knockdown models for 16p11.2 homologs.	9
Figure S5. Interactions between 16p11.2 homologs.	11
Figure S6. Interactions of 16p11.2 homologs with neurodevelopmental genes.	13
Figure S7. Functional enrichment of differentially-expressed genes in 16p11.2 knockdowns.	15
Figure S8. A complex interaction model for pathogenicity of 16p11.2 deletion.	17
SUPPLEMENTARY TABLES.....	19
Table S1. <i>Drosophila</i> homologs and model organism phenotypes of 16p11.2 genes.	19
Table S2. RNAi and deficiency fly stocks used for one-hit and two-hit experiments (Excel file).	21
Table S3. Quantitative PCR analysis of 16p11.2 homolog knockdowns (Excel file).	21
Table S4. Percentiles of <i>Flyntyper</i> scores for one-hit knockdown flies with <i>Dicer2</i>	22
Table S5. Tested and validated pairwise knockdown models between 16p11.2 homologs (Excel file).....	23
Table S6. Tested and validated pairwise knockdown models of 16p11.2 homologs with neurodevelopmental and transcriptome genes (Excel file).....	23
Table S7. Differentially-expressed genes in 16p11.2 knockdown flies (Excel file).	23
Table S8. Input and connector genes identified in a human brain-specific interaction network (Excel file).	23
Table S9. Pathogenicity of 16p11.2 genes based on human allele frequency metrics.	24
Table S10. Primers used in the PCR experiments (Excel file).	25
Table S11. Statistical analysis of experimental data (Excel file).....	25
REFERENCES.....	25

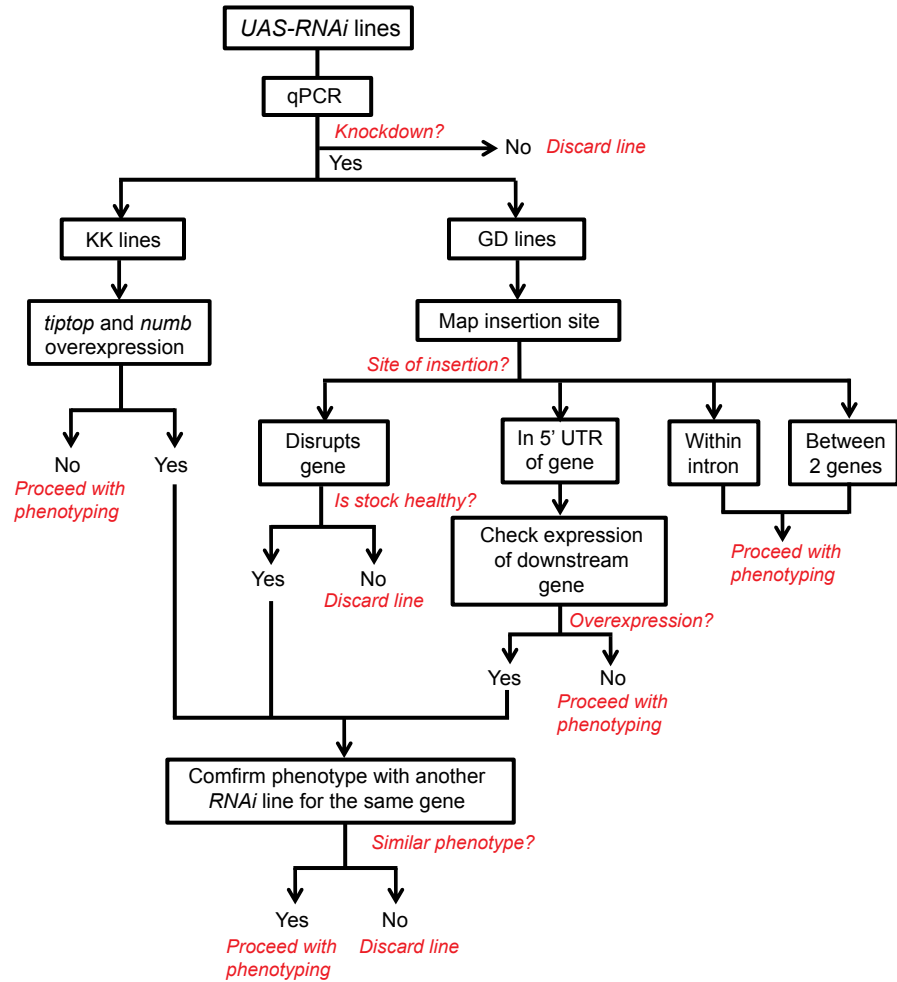
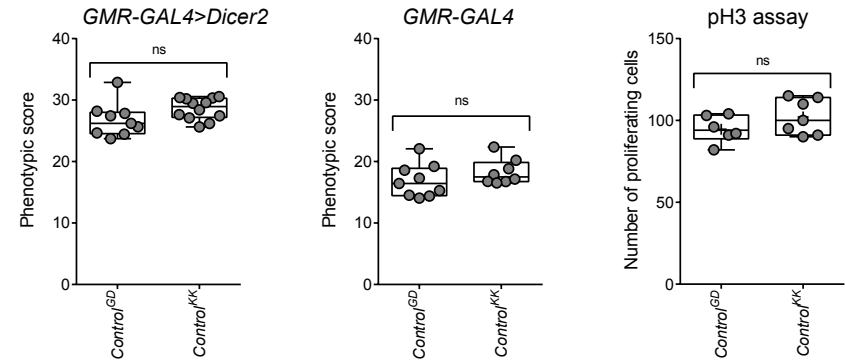
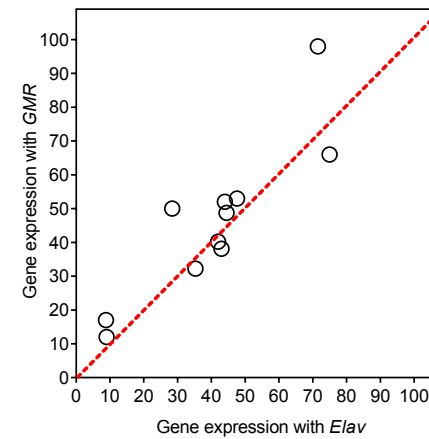
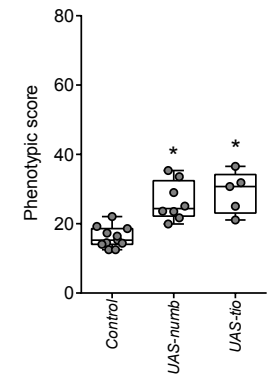
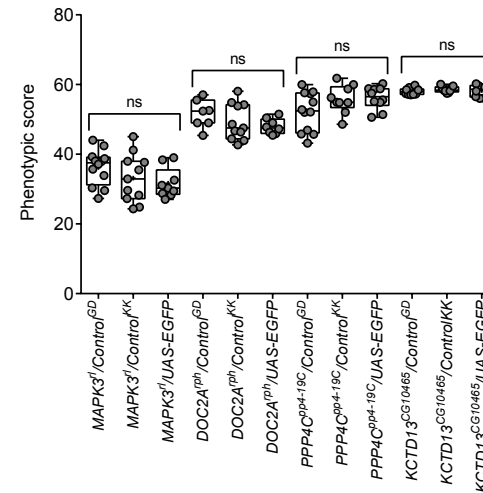
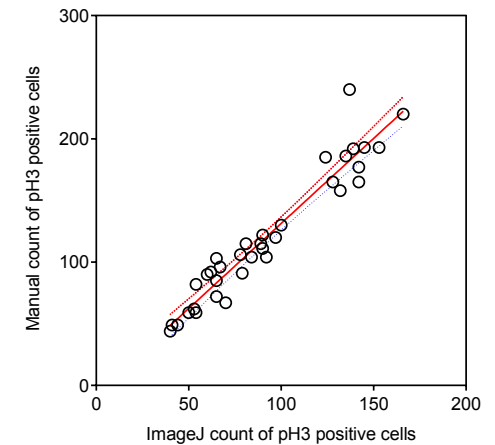
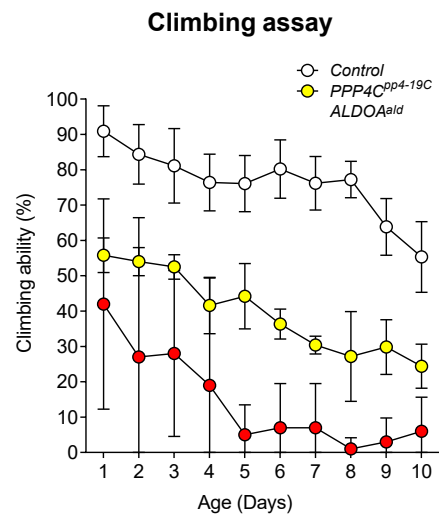
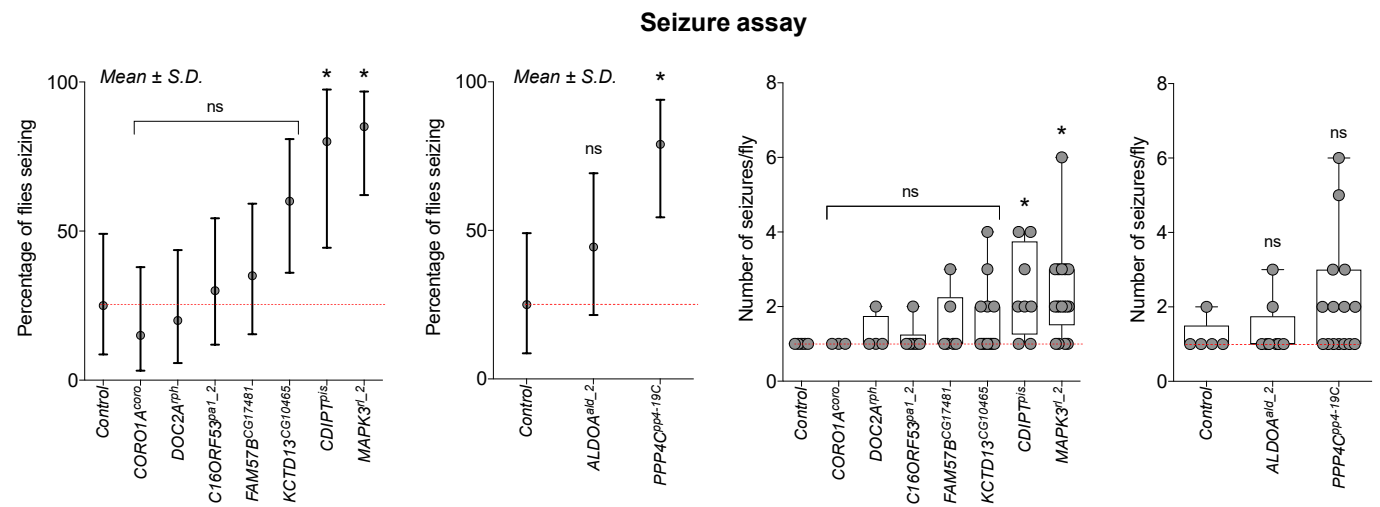
A**Quality control strategy****B****Comparison of GD and KK control lines****C****qPCR analysis of 16p11.2 homolog knockdowns****D****Overexpression of *tiptop* and *numb*****E****Efficiency of GAL4 in two-locus interaction studies****F****Comparison of manual count vs ImageJ count in proliferating cells**

Figure S1. Quality control of fly RNAi knockdown lines. (A) Quality control strategy for RNAi lines of 16p11.2 homologs. The level of knockdown was checked using qPCR (Figure S1B), followed by insertion site mapping of GD lines and checking *tiptop* and *numb* overexpression in KK lines. We screened a total of 44 RNAi lines for 16p11.2 homologs and selected 31 RNAi lines for our knockdown experiments. (B) *Flynotyper* scores of KK and GD control eyes with *GMR-GAL4>Dicer2* and *GMR-GAL4* without *Dicer2*, and number of proliferating cells. We found no differences in the phenotypes of GD and KK controls (n=7-12, Mann-Whitney test). (C) Scatter plot comparing gene expression (mRNA) of 11 homologs of 16p11.2 genes with *GMR-GAL4* and *Elav-GAL4* drivers. A high correlation was observed between knockdown lines using the two drivers (Pearson correlation, $r=0.8877$). (D) Phenotypic scores of *UAS-tio* and *UAS-numb* with *GMR-GAL4* at 30°C. The *Flynotyper* scores for each overexpression line were significantly higher (n=5-8, Mann-Whitney test, $*p<0.05$). (E) *Flynotyper* scores of *UAS-GFP* crosses with 16p11.2 homologs used in two-locus interaction studies show no difference in the eye phenotypes of flies with one *UAS* versus two *UAS* lines (n=8-11, Mann-Whitney test). (F) Plot comparing manual count versus ImageJ Analyze particles count of number of proliferating cells. While high correlation (Pearson correlation, $r=0.9599$, $p<0.0001$) was observed between the two counts, all results shown in the text for number of proliferating cells were counted manually.

A



B

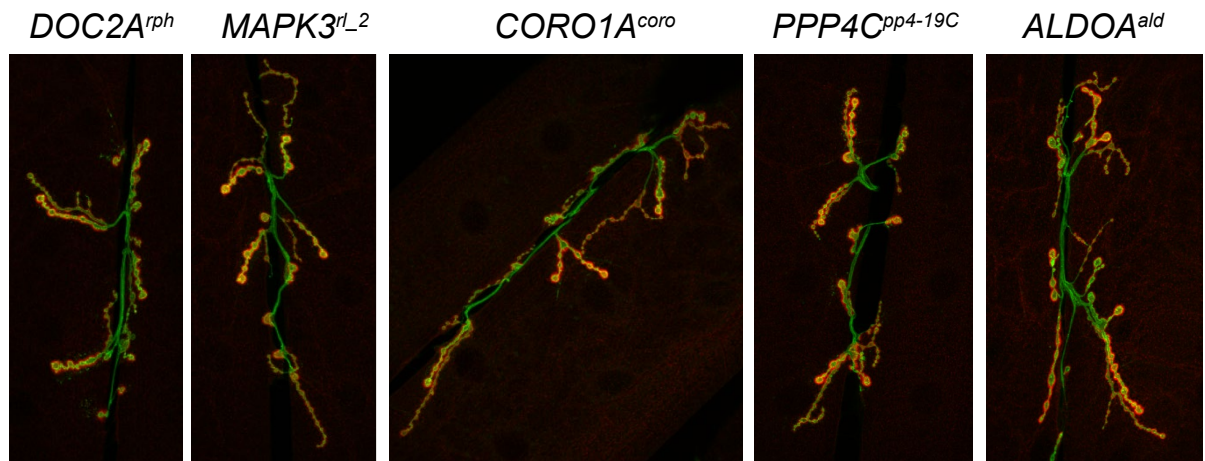


C

NMJ architecture

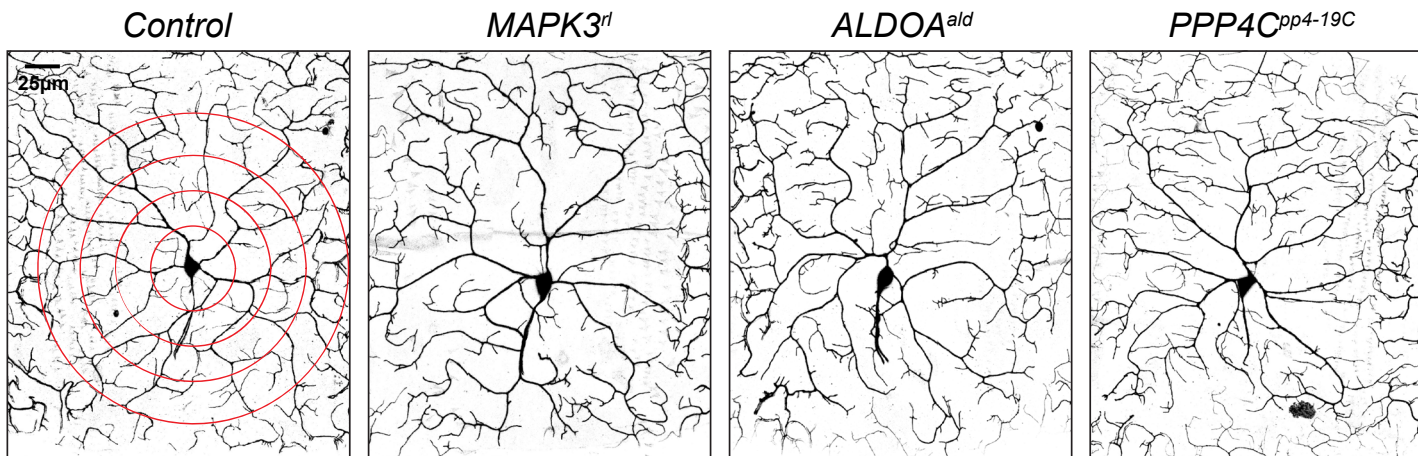
Gene	NMJ length	NMJ area	NMJ perimeter	Bouton number	Number of branches
<i>FAM57B^{CG17481}</i>	ns	+	ns	+	ns
<i>CDIPT^{plis}</i>	+	ns	ns	+	ns
<i>ALDOA^{ald}</i>	+	ns	ns	ns	+
<i>KCTD13^{CG10465}</i>	ns	ns	ns	ns	ns
<i>C16ORF53^{pa1}</i>	ns	ns	ns	ns	ns
<i>CORO1A^{coro}</i>	ns	ns	ns	ns	ns
<i>DOC2A^{rph}</i>	ns	ns	ns	ns	ns
<i>MAPK3^{rl}</i>	ns	ns	ns	ns	ns
<i>PPP4C^{pp4-19C}</i>	ns	ns	ns	ns	ns

D



E

Dendritic arborization



F

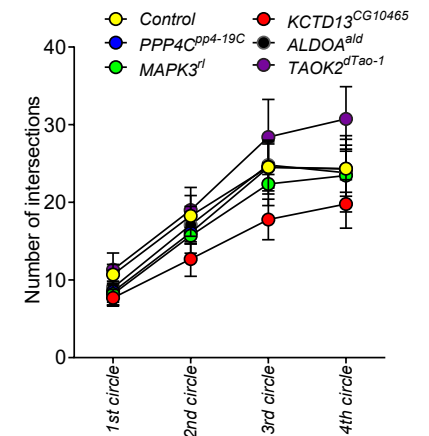


Figure S2. Neurodevelopmental defects in flies with knockdown of individual 16p11.2 homologs. (A) Assessment of motor defects in 16p11.2 homologs with *Elav-GAL4* and no *Dicer2* showed changes in climbing ability over ten days compared to control (two-way ANOVA, $F=1.6199$, $df=27$, $p=0.0286$). Data represented here shows mean \pm standard deviation of 10 independent groups of 10 flies for each line. (B) Assessment of frequency of spontaneous unprovoked seizure events (Fisher's Exact test, $n=10-20$, $*p<0.05$) and average number of seizure events per fly (Mann-Whitney test, $n=3-17$, $*p<0.05$) for seven 16p11.2 homologs with *Elav-GAL4>Dicer2* and two homologs, *PPP4C^{pp4-19C}* and *ALDOA^{ald}*, with *Elav-GAL4* and no *Dicer2*. Error bars for seizure frequency indicate binomial proportion confidence intervals. Three top homologs were selected for further validation with a larger sample size (Figure 2C). (C) Assessment of neuromuscular junction features for 16p11.2 homologs. "+" indicates a significant change compared to control ($p<0.05$, two-tailed Mann-Whitney test), while "ns" indicates no change in that feature. (D) Representative confocal images of NMJs for knockdown of five 16p11.2 homologs. *DOC2A^{rh}*, *MAPK3^{rl}*, and *CORO1A^{coro}* were generated using *Elav-GAL4>Dicer2* at 25°C, while *PPP4C^{pp4-19C}* and *ALDOA^{ald}* were generated using *Elav-GAL4* without *Dicer2* at room temperature. (E) Representative confocal live images of class IV da neurons labeled with *mCD8-GFP* under the control of *ppk-GAL4* are shown for three 16p11.2 homologs and control. Red circles on the control image indicate the circles used in Sholl analysis. (F) Line plot of the number of intersections at each concentric circle (two-way ANOVA, $p=0.0027$, $df=5$, $F=3.76$). Intersections were calculated by manual Sholl analysis and normalized to width measurement for each given hemisegment to control for slight size variation. Data represented here shows mean \pm standard deviation of 10-16 flies per genotype for each circle.

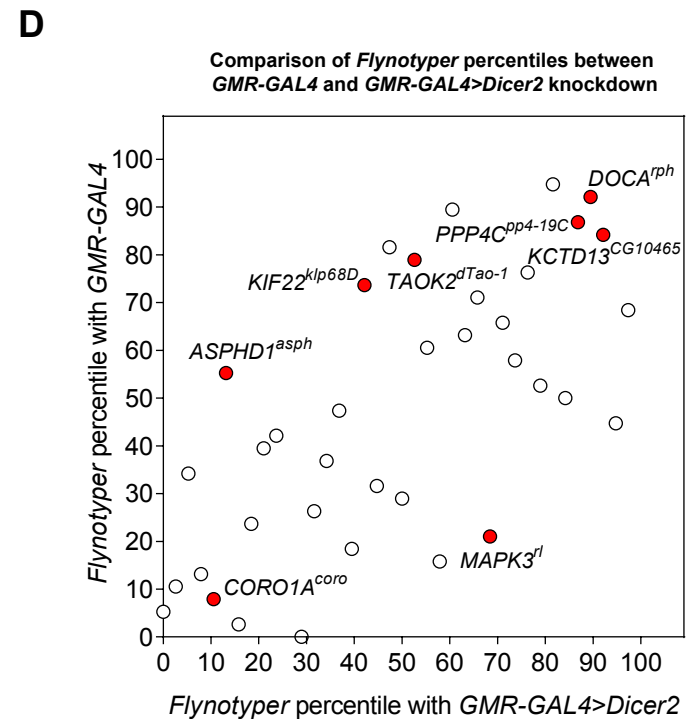
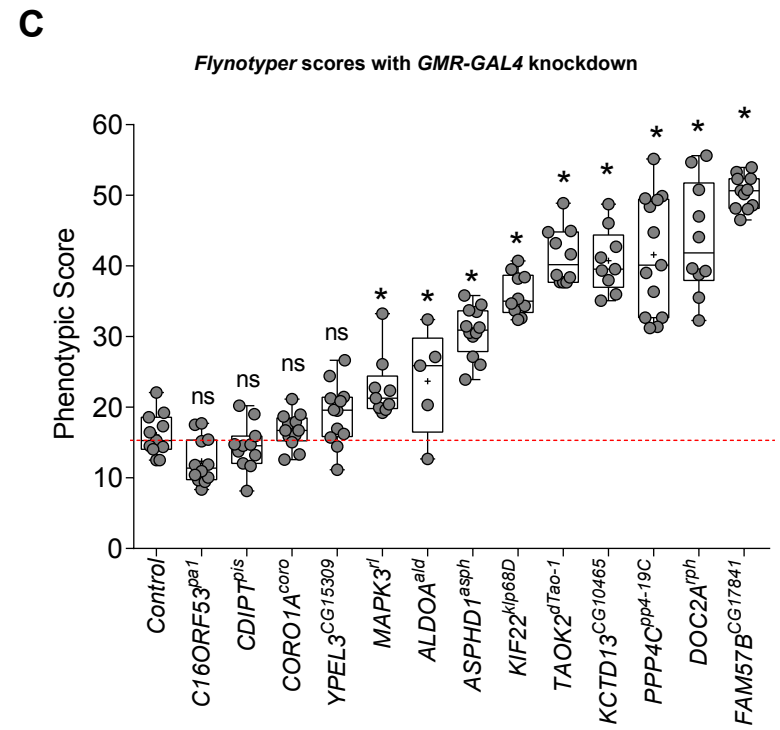
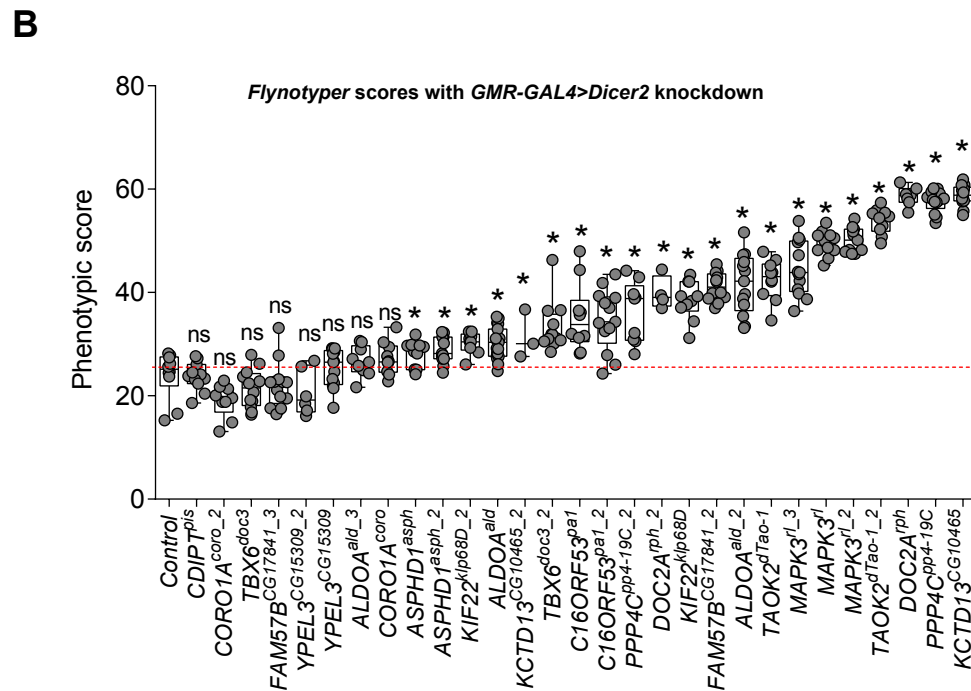
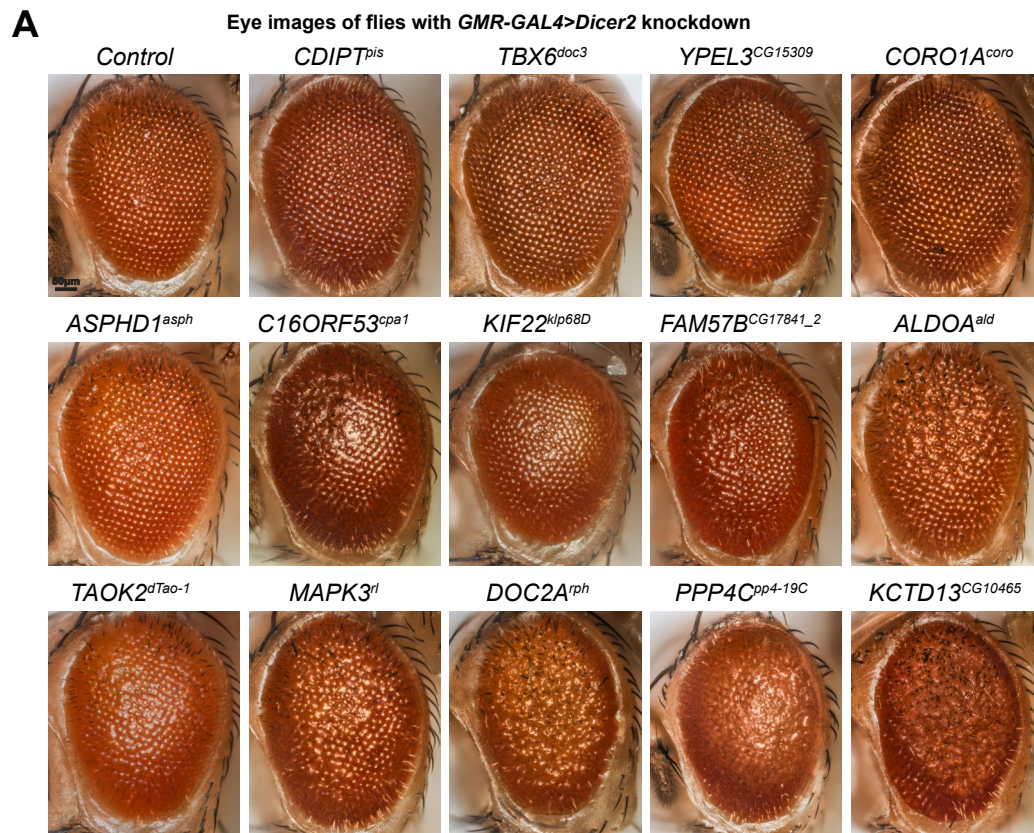
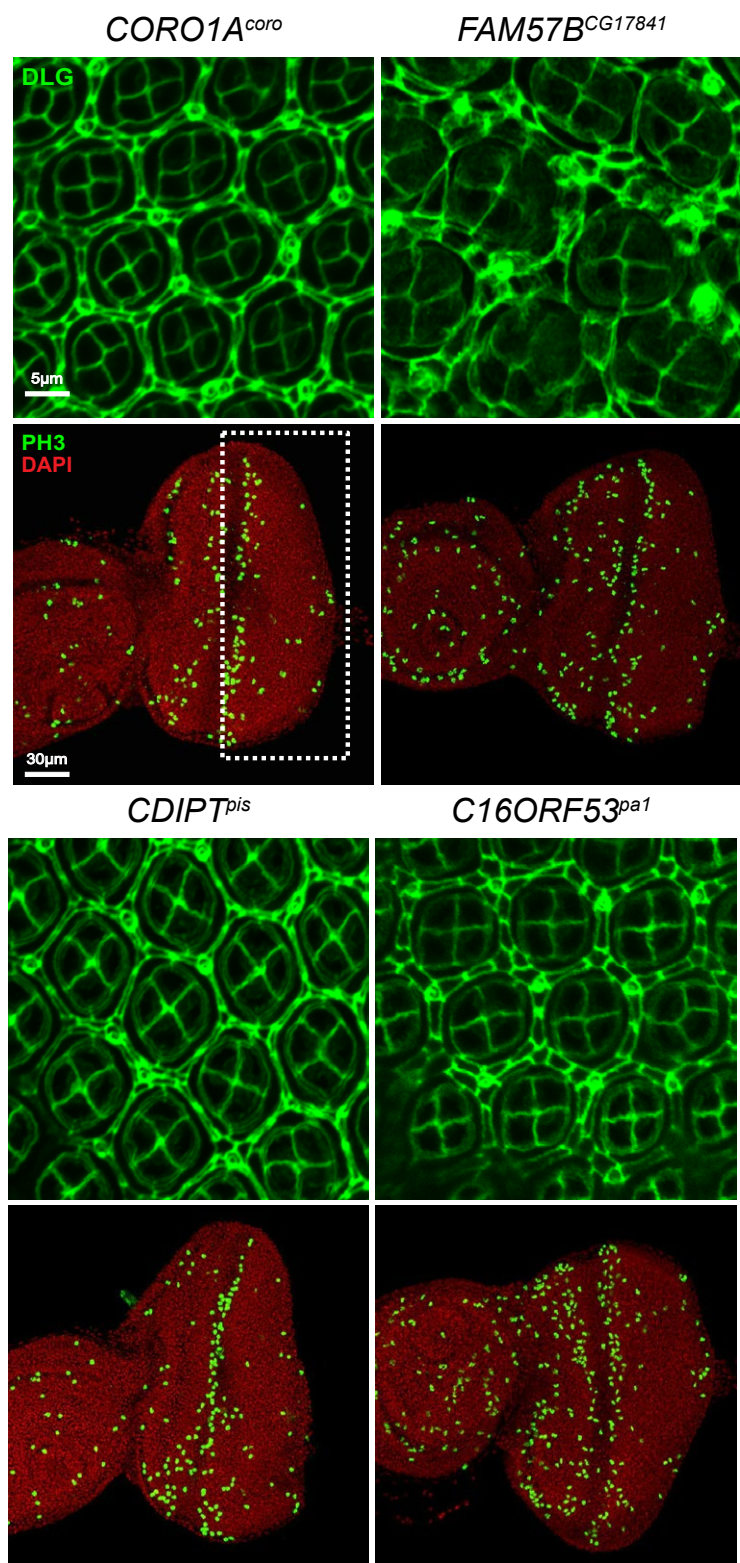
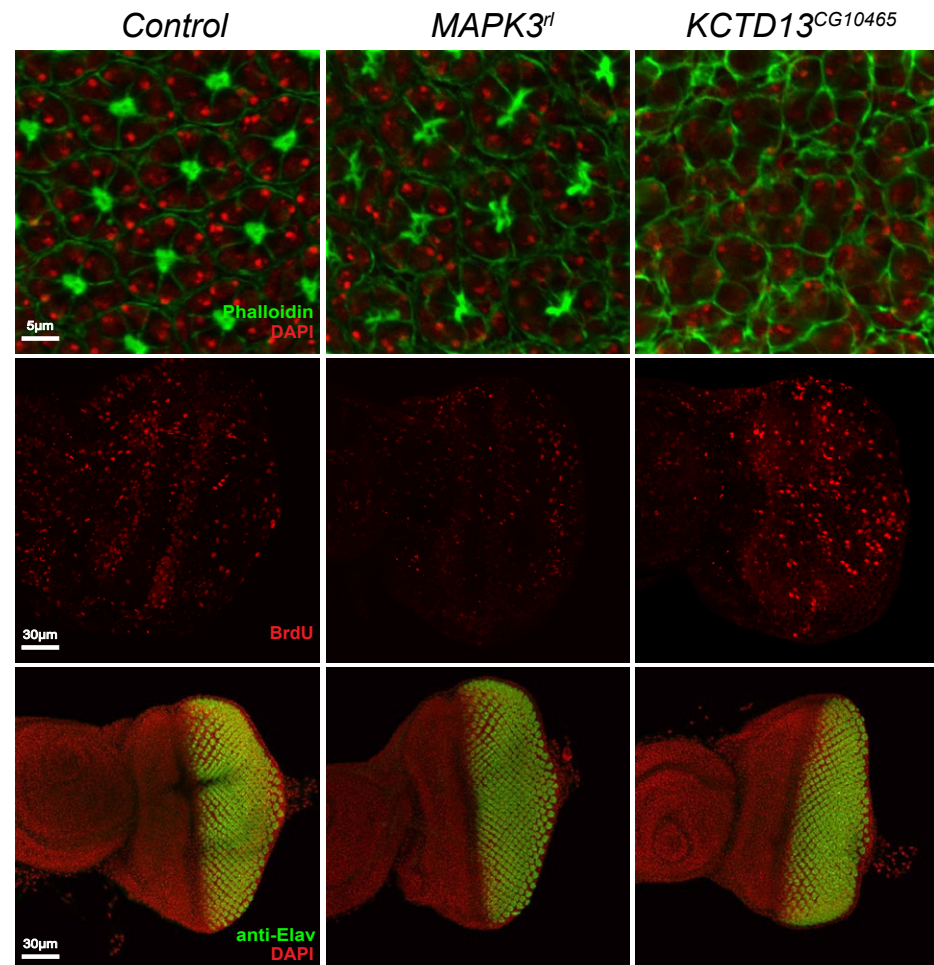


Figure S3. Adult eye phenotypes of one-hit knockdown models of 16p11.2 homologs. (A) Representative brightfield microscope images of fly eyes displaying eye-specific knockdown for each 16p11.2 homolog at 30°C with *GMR-GAL4>Dicer2* driver. (B) *Flynotyper* scores for 29 tested *GMR-GAL4>Dicer2* lines of 16p11.2 homologs. Twenty-one lines had significantly higher *Flynotyper* scores compared to the controls (n=3-19, Mann-Whitney test, *p<0.05). Two tested lines, *FAM57B*^{CG17841} (lethal) and *CDIPT*^{pis_2}, are not shown in this figure. (C) Box plot of *Flynotyper* scores for knockdown of 13 tested homologs of 16p11.2 genes with *GMR-GAL4* and no *Dicer2*. Nine of the 13 tested homologs had significantly higher *Flynotyper* scores than the control (n=5-13, Mann-Whitney test, *p<0.05). (D) Comparison of percentile ranks for *Flynotyper* scores of *GMR-GAL4* lines of 16p11.2 homologs and other neurodevelopmental genes with and without *Dicer2* (Table S3). Select 16p11.2 genes are highlighted in red. Percentiles of homologs with *Dicer2* correlate to percentiles of homologs without *Dicer2* (Pearson correlation, r=0.6853, p=2.877×10⁻⁶), showing that relative severity of the eye phenotype is not affected by *Dicer2*.

A



B



C

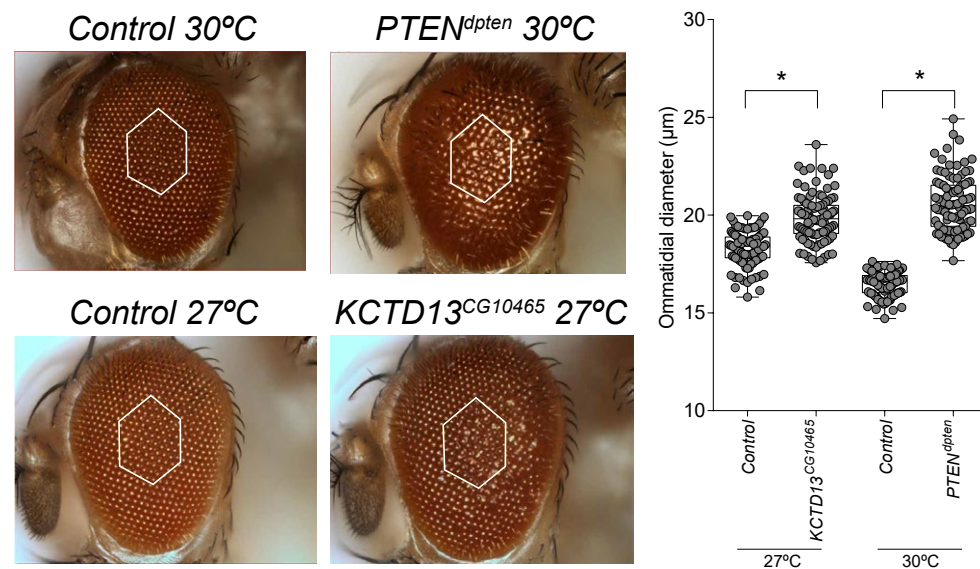
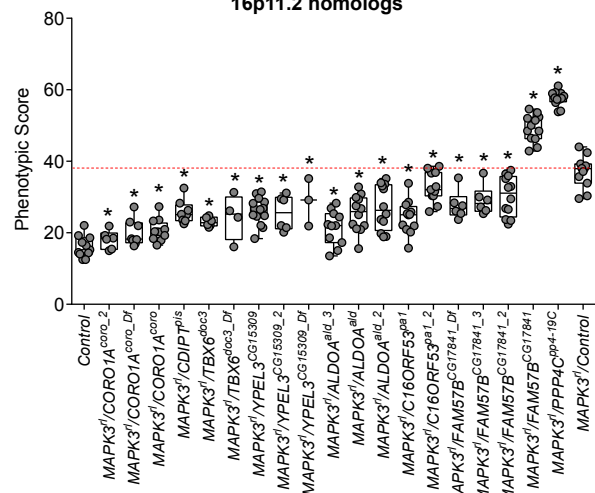


Figure S4. Cellular eye phenotypes of one-hit knockdown models for 16p11.2 homologs. (A) Representative confocal images of the pupal eye and larval eye disc illustrate the defects observed in eye-specific knockdown of four 16p11.2 homologs with *GMR-GAL4* driver and no *Dicer2* (other homologs are shown in Figures 3C and 4E). (B) Representative confocal images of pupal eyes stained with phalloidin and DAPI for 16p11.2 homologs illustrate defects in photoreceptor cell counts, and larval eye discs stained with BrdU and anti-Elav show the effects of knockdown on cell proliferation and differentiation, respectively. No significant difference in the number of differentiating cells was observed in either knockdown when compared to control. (C) Eye images of control, *PTEN*^{*dpten*} and *KCTD13*^{*CG10465*} knockdown flies highlighting regions (white hexagons) used to calculate the average size of each ommatidium. *KCTD13*^{*CG10465*} knockdown flies were raised at 27°C due to severity of the eye phenotype at 30°C. Both knockdowns showed an increase in ommatidial diameter compared to their respective controls (n=100, *p<0.05, Mann-Whitney test).

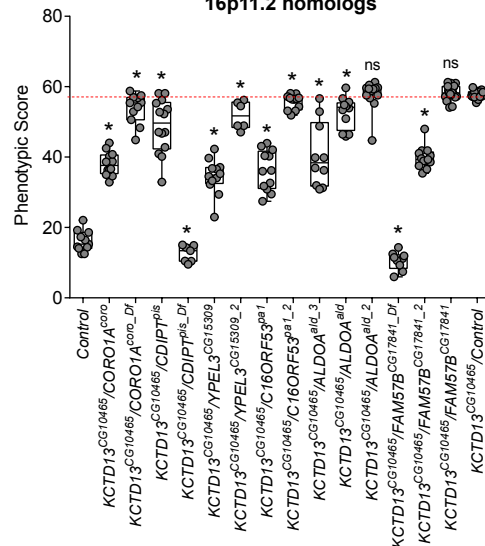
A

MAPK3^{rl} interactions with 16p11.2 homologs



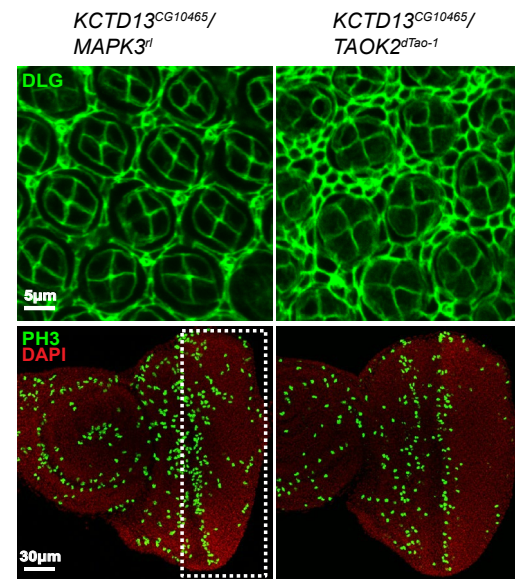
B

KCTD13^{CG10465} interactions with 16p11.2 homologs

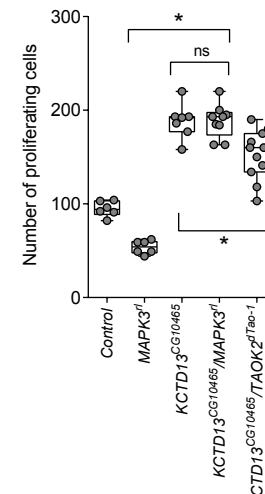


F

Cellular phenotypes of 16p11.2 two-hit models

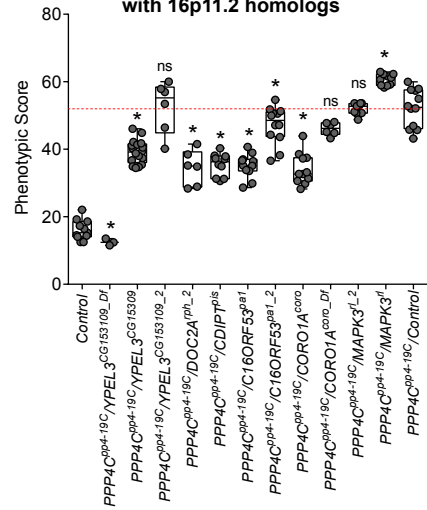


G



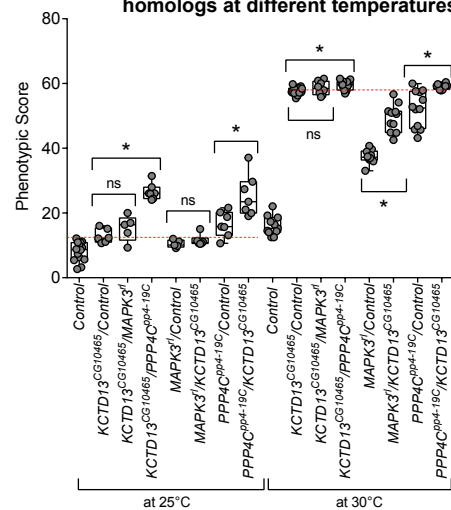
C

PPP4C^{pp4-19C} interactions with 16p11.2 homologs



D

KCTD13^{CG10465} interactions with 16p11.2 homologs at different temperatures.

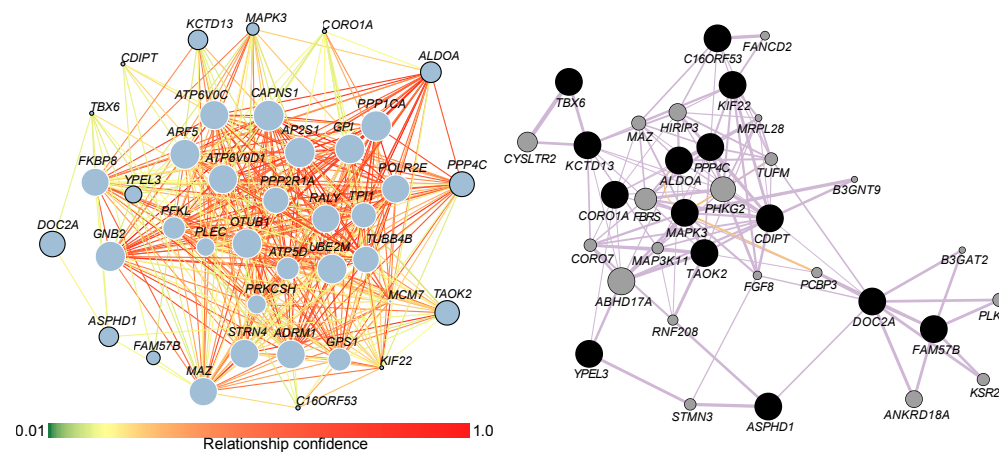


H

Gene	Cone cell defects	Primary cell defects	Bristle group defects	Secondary cell defects	Tertiary cell defects	Rotation defects	Hexagon structure defects
MAPK3 ^{rl}		+	+	++	+	+	+
MAPK3 ^{rl} /ALDOA ^{ald}		Supp	Supp	+		Supp	
MAPK3 ^{rl} /TAOK2 ^{dTao-1}		Supp	+	+	+	+	+
KCTD13 ^{CG10465}	+++	+	++	++	+	+	++
KCTD13 ^{CG10465} /ALDOA ^{ald}	Supp	Supp	++	Supp	Supp		Supp
KCTD13 ^{CG10465} /TAOK2 ^{dTao-1}	Supp	Supp	++	++	+	+	++
KCTD13 ^{CG10465} /MAPK3 ^{rl}	Supp	Supp	++	++	++	+	++

I

Human genetic interaction networks of 16p11.2 genes



E

DOC2A^{rh} interactions with 16p11.2 homologs

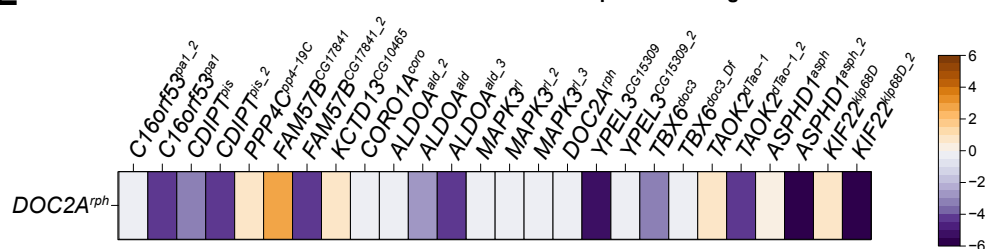
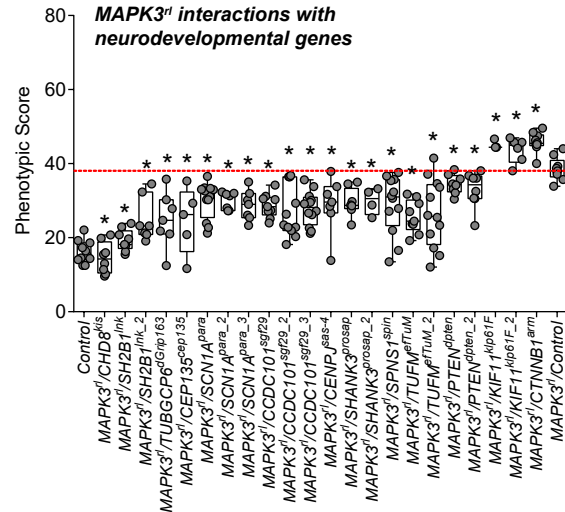
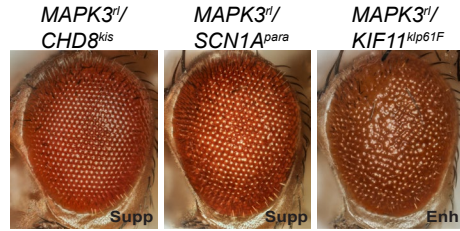
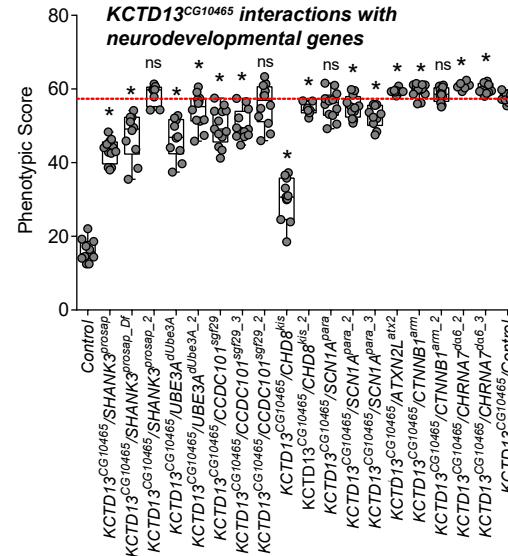
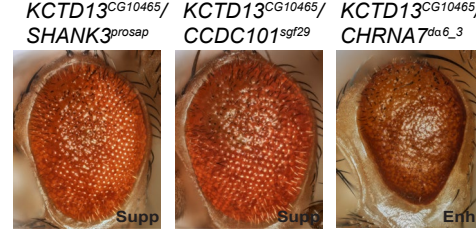


Figure S5. Interactions between 16p11.2 homologs. (A) Representative eye images and *Flynotyper* scores for 19 crosses of *MAPK3^{rl}* with eight 16p11.2 homologs that modify the one-hit *MAPK3^{rl}* phenotype (n=3-15, Mann-Whitney test, *p<0.05). Concordant results from two or more lines were required to identify positive interactions. Because single knockdown of *FAM57B^{CG17841}* is partially lethal, the two-hit model with *MAPK3^{rl}* is considered suppression. (B) Representative eye images and *Flynotyper* scores for 15 crosses of *KCTD13^{CG10465}* with six 16p11.2 homologs that modify the one-hit *KCTD13^{CG10465}* phenotype (n=3-17, Mann-Whitney test, *p<0.05). Because RNAi knockdown of *FAM57B^{CG17841}* is partially lethal, the two-hit model with *KCTD13^{CG10465}* is considered as a suppression of the lethality phenotype. (C) Representative eye images and *Flynotyper* scores for 11 crosses of *PPP4C^{pp4-19C}* with six 16p11.2 homologs that modify the one-hit *PPP4C^{pp4-19C}* phenotype (n=6-20, Mann-Whitney test, *p<0.05, two-tailed Mann-Whitney test). Even though only one line of *MAPK3^{rl}* and *CORO1A^{coro}* showed statistically-significant changes compared to the one-hit control, the second lines tested showed suppression of the glossy eye phenotype or a trend towards enhancement of the phenotype, respectively, which were indicative of validated interactions. (D) Representative eye images and *Flynotyper* scores for *KCTD13^{CG10465}* two-hit crosses with *MAPK3^{rl}* and *PPP4C^{pp4-19C}* at different temperatures (n=5-13, Mann-Whitney test, *p<0.05). We suspected that the enhanced eye phenotypes at 30°C were due to severity of *KCTD13^{CG10465}* knockdown, and confirmed a significant enhancement of the eye phenotype only for *KCTD13^{CG10465}/PPP4C^{pp4-19C}* at 25°C. (E) A heat map of the change in manual eye scores of *DOC2A^{rph}* two-hit knockdowns with other 16p11.2 homologs compared to *DOC2A^{rph}* one-hit flies. (F) Representative confocal images of pupal eye and larval eye disc, stained with anti-Dlg and anti-pH3 respectively, of double knockdown of *KCTD13^{CG10465}/MAPK3^{rl}* and *KCTD13^{CG10465}/TAOK2^{dTao-1}*. (G) Assessment of proliferating cell count in the larval eyes shown in Figure S4F (n=9-11, Mann-Whitney test, *p<0.05). (H) Table summarizing the cellular defects observed in the pupal eyes of one-hit and two-hit 16p11.2 homologs knockdown. “+” symbols indicate the severity of the observed cellular defects, while “Supp” indicates that the cellular defects were suppressed in the two-hit models. (I) Interaction network of fourteen tested 16p11.2 genes in the context of a brain-specific gene interaction network¹ and (right) a general human gene interaction network (GeneMania)². (Left) Nodes with black borders represent 16p11.2 genes, while white borders represent 25 connector genes. The size of the nodes represents a predictive score for the involvement of each gene in autism, and colors of the edges represent confidence (min. 0.1) in the annotated interactions. (Right) Grey-shaded nodes represent the input 16p11.2 genes, while black nodes represent the connector genes. Edge color represents interaction data source (purple: co-expression, orange: predicted interaction). Also note that the 16p11.2 distal gene *TUFM* is connected to *MAPK3*, *C16ORF53*, and *DOC2A* in the GeneMania interaction network, consistent with the interactions identified in fly models.

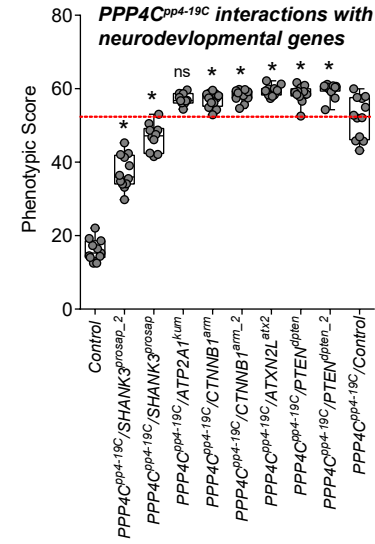
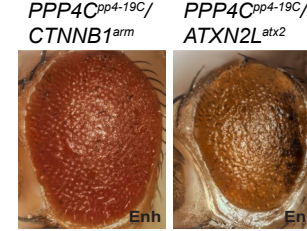
A



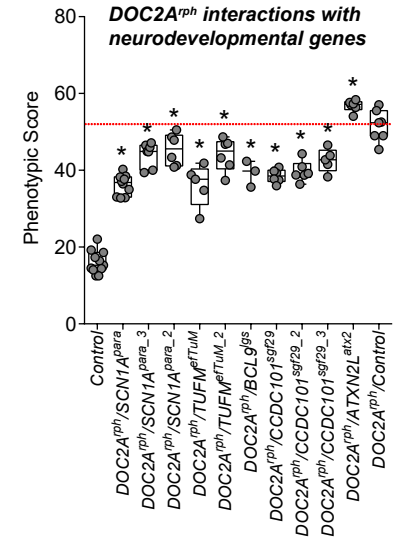
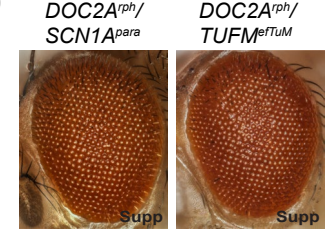
B



C

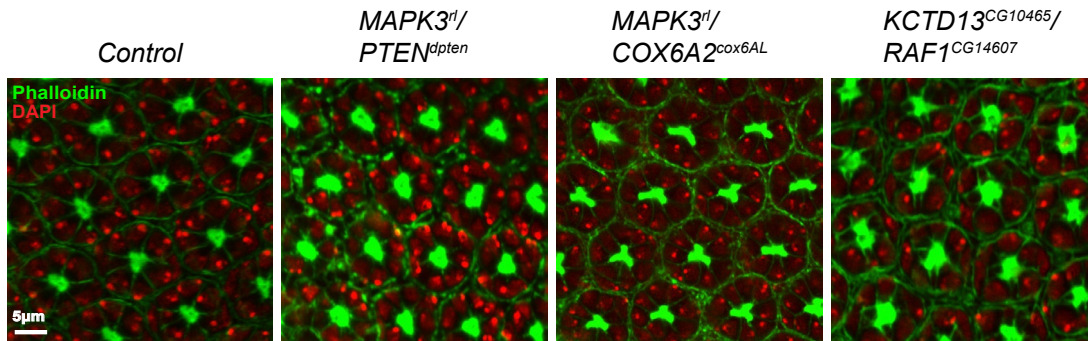


D



E

Phalloidin staining for analysis of photoreceptor cells



F

Cellular defects between 16p11.2 homologs and neurodevelopmental genes

Gene	Cone cell defects	Primary cell defects	Bristle group defects	Secondary cell defects	Tertiary cell defects	Rotation defects	Hexagon structure defects
MAPK3 ^{rl}		+	+	++	+	+	+
MAPK3 ^{rl} /PTEN ^{pten}		Supp	+	Supp	Supp	Supp	Supp
MAPK3 ^{rl} /COX6A2 ^{cox6AL}		Supp	+	Supp	Supp	Supp	Supp
KCTD13 ^{CG10465}	+++	+	++	++	+	+	++
KCTD13 ^{CG10465} /RAF1 ^{CG14607}	Supp	Supp	++	++	+	Supp	+

Figure S6. Interactions of 16p11.2 homologs with neurodevelopmental genes. (A) Representative eye images and *Flynotyper* scores for 22 crosses of *MAPK3^{rl}* with 13 neurodevelopmental genes that modify the one-hit *MAPK3^{rl}* phenotype (n=3-12, Mann-Whitney test, *p<0.05). Concordant results from two or more lines were required to identify positive interactions. (B) Representative eye images and *Flynotyper* scores for 18 crosses of *KCTD13^{CG10465}* with eight neurodevelopmental genes that modify the one-hit *KCTD13^{CG10465}* phenotype (n=6-18, Mann-Whitney test, *p<0.05). While the *Flynotyper* score of *KCTD13^{CG10465}/CTNNB1^{arm-2}* is not significant, it is considered to be an enhancer since black spots were observed in the double knockdown. (C) Representative eye images and *Flynotyper* scores for eight crosses of *PPP4C^{pp4-19C}* with five neurodevelopmental genes that modify the one-hit *PPP4C^{pp4-19C}* phenotype (n=10-12, Mann-Whitney test, *p<0.05). While *PPP4C^{pp4-19C}/ATP2A1^{kum}* did not have a significant *Flynotyper* score, we considered this interaction to be an enhancement due to its glossy eye phenotype. (D) Representative eye images and *Flynotyper* scores for 10 crosses of *DOC2A^{rph}* with five neurodevelopmental genes that modify the one-hit *DOC2A^{rph}* phenotype (n=3-10, Mann-Whitney test, *p<0.05). (E) Representative confocal images of pupal eyes stained with phalloidin and DAPI in control and double knockdowns of *MAPK3^{rl}/PTEN^{dpten}*, *MAPK3^{rl}/COX6A2^{cox6AL}* and *KCTD13^{CG10465}/RAF1^{CG14607}*. (F) Table summarizing the cellular defects observed in the pupal eye of one-hit *MAPK3^{rl}* and *KCTD13^{CG10465}* flies compared to double knockdown of *MAPK3^{rl}/PTEN^{dpten}*, *MAPK3^{rl}/COX6A2^{cox6AL}* and *KCTD13^{CG10465}/RAF1^{CG14607}*. “+” symbols indicate the severity of the observed cellular defects, while “Supp” indicates that the cellular defects were suppressed in the two-hit models.

Enriched gene ontology terms in differentially-expressed genes of 16p11.2 homologs



Network of cell proliferation genes differentially expressed in 16p11.2 homologs

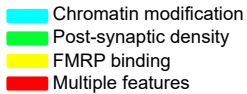


Figure S7. Functional enrichment of differentially-expressed genes in 16p11.2 knockdowns. (A) Heatmap showing selected Gene Ontology biological process terms whose component genes have significantly higher (blue) or lower (orange) expression values in the six 16p11.2 homolog knockdowns compared to wild-type control ($p < 0.01$ corrected by Benjamini-Hochberg method, Parametric Analysis of Geneset Enrichment test). (B) Network of all differentially-expressed cell proliferation genes in each 16p11.2 knockdown model. Edges connect 16p11.2 genes (hub nodes) to differentially-expressed genes (outer nodes). Thick node borders indicate genes related to neurodevelopmental diseases, while the node color represents neurodevelopmental function of those genes.

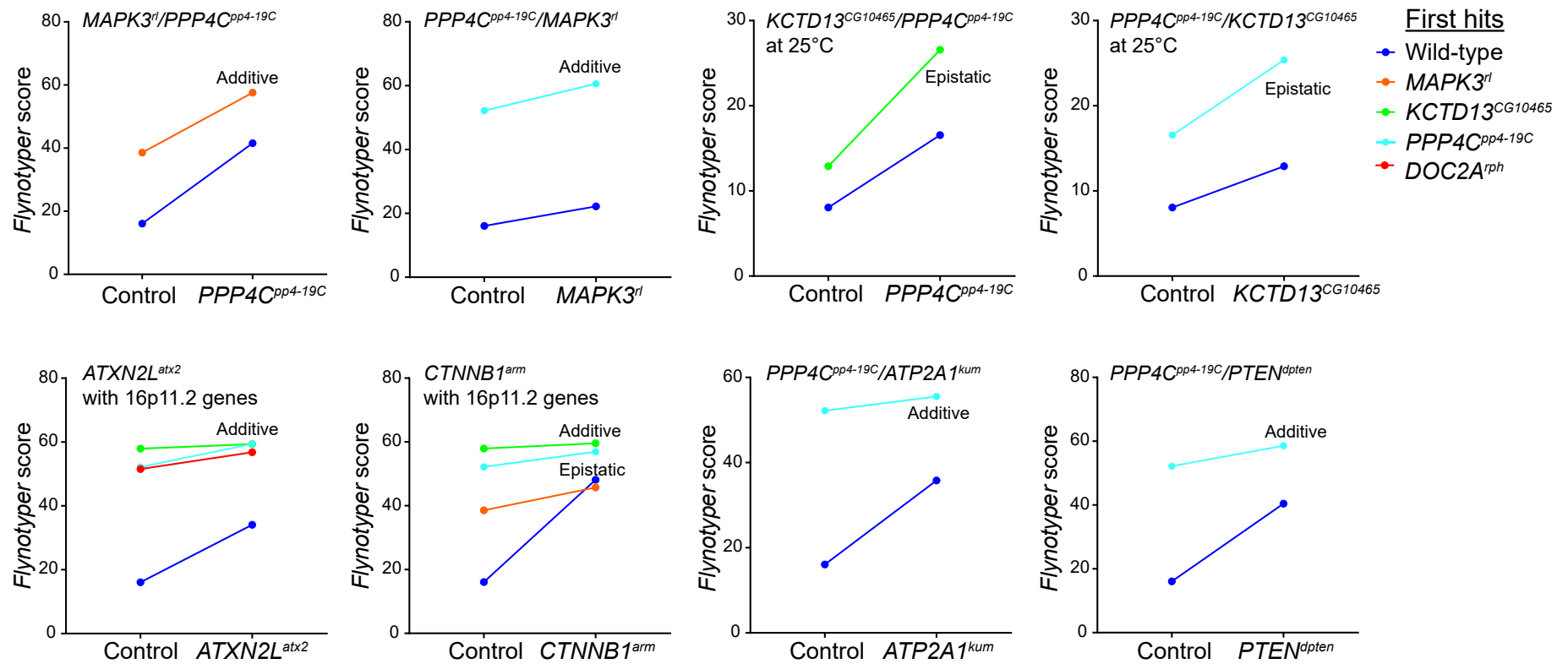
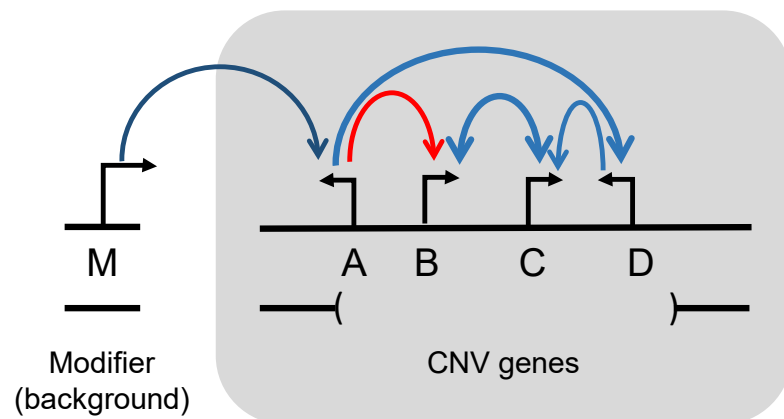
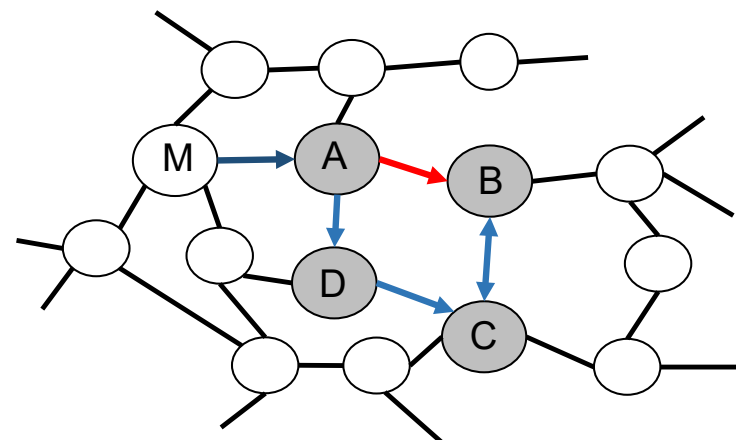
A**Phenotypic effects of selected interactions****B****Genetic interactions****Mechanistic effects**

Figure S8. A complex interaction model for pathogenicity of 16p11.2 deletion. (A) *Flynotyper* phenotypes of 16p11.2 pairwise knockdowns showing enhancement of the one-hit phenotypes. These plots are similar to those in Figure 7A and were generated to delineate additive interactions from epistatic enhancers. Interactions between *KCTD13*^{CG10465}/*PPP4C*^{pp4-19C} and *PPP4C*^{pp4-19C}/*KCTD13*^{CG10465} at 25°C as well as *MAPK3*^{rl}/*CTNNB1*^{arm} are epistatic, while the remaining interactions are additive. (B) In the human 16p11.2 deletion, modifier genes elsewhere in the genome can modulate the effects of multiple CNV genes (left) through shared cellular pathways (right), allowing the epistatic interactions between pairs of CNV genes to ultimately influence the observed neurodevelopmental phenotypes. Colored arrows represent suppression, blue, or enhancement, red, of the phenotypes caused by single-gene knockdown.

SUPPLEMENTARY TABLES

Table S1. *Drosophila* homologs and model organism phenotypes of 16p11.2 genes.

	Human gene	Fly ortholog	DIOPT score	Query coverage	Percentage identity (aa)	E value	<i>Drosophila</i> phenotypes							Zebrafish phenotypes			Mouse phenotypes		
							Early stage lethality (larval/pupal)	Developmental defects	Eye morphology defects	Neuronal defects	Motor defects	Expression in developing eye	Expression in adult eye	Neuroanatomical defects	Motor defects	Brain morphology defects	Developmental defects	Neuronal defects	Other defects *
1	<i>CDIPT</i>	<i>CG9245 (pis)</i>	10.00	98%	51%	2.00E-71	+	+		+	+	+	+			+			+
2	<i>PPP4C</i>	<i>CG32505 (pp4-19C)</i>	9.00	100%	92%	0	+	+	++	+	+	+	+		+	+	+ L		+
3	<i>ALDOA</i>	<i>CG6058 (ald)</i>	9.00	99%	69%	0	+	+	+	+	+	+	+		+	+	ND	ND	ND
4	<i>YPEL3</i>	<i>CG15309</i>	7.00	94%	82%	1.00E-64		+				+	+		+	+		+	+
5	<i>FAM57B</i>	<i>CG17841</i>	7.00	93%	30%	2.00E-27		+	++	+	+	+	+		+	+	ND	ND	ND
6	<i>CORO1A</i>	<i>CG9446 (coro)</i>	7.00	100%	50%	2.00E-173	+	+		+	+	+	+		+	+		+	+
7	<i>INO80E</i>	<i>CG18004</i> ¹	7.00	29%	65%	2.00E-12													
8	<i>MAPK3</i>	<i>CG12559 (rl)</i>	6.00	89%	82%	0		+	+	+	+	+	+		+	+	+	+	+
9	<i>KCTD13</i>	<i>CG10465</i>	6.00	79%	63%	1.00E-117		+	++	++	+	+	+	+	+	+	ND	ND	ND
10	<i>TAOK2</i>	<i>CG14217 (dTao-1)</i>	6.00	31%	68%	7.00E-165	+	+	+	+	ND	+	+			+		+	+
11	<i>TBX6</i>	<i>CG5093 (doc3)</i>	6.00	43%	58%	5.00E-76	+	+	+		+	+	+		+	+	+	+	+
12	<i>DOC2A</i>	<i>CG11556 (rph)</i>	5.00	75%	38%	9.00E-64		+	++	+	+		+			+		+	
13	<i>ASPHD1</i>	<i>CG8421 (asph)</i>	3.00	33%	38%	5.00E-19				ND	+		+			+	ND	ND	ND
14	<i>C16ORF53</i>	<i>CG11750 (pal)</i>	3.00					+	+	+	+	+	+			+	ND	ND	ND
15	<i>KIF22</i>	<i>CG7293 (klp68D)</i>	-	53%	41%	2.00E-64	+	+	+	+	ND	+	+		+	+	+		+
16	<i>MAZ</i>	<i>CG14938 (crol)</i>	1.00	62%	26%	1.00E-29													
17	<i>SEZ6L2</i>	<i>CG1500 (fw)</i>	-	29%	30%	7.00E-13													
18	<i>GDPD3</i>	<i>CG3942</i>	-	14%	39%	6.00E-12													

19	<i>SPN</i>	<i>CG13409</i>	-	31%	28%	1.8													
20	<i>C16ORF54</i>	<i>CG6621</i>	-	25%	33%	1.5													
21	<i>TMEM219</i>	<i>CG6280</i>	-	14%	29%	0.010													
22	<i>QPRT</i>	<i>CG15730</i>	-	8%	41%	0.037													
23	<i>PRRT2</i>	<i>No ortholog</i>	-																
24	<i>MVP</i>	<i>No ortholog</i>	-																
25	<i>HIRIP3</i>	<i>No ortholog</i>	-																

¹ No RNAi lines were available for *CG18004*.

*Cellular, immunological, cardiovascular, mortality/aging, hematopoietic, muscular, hearing/vestibular/ear, limbs/digits/tail, endocrine/exocrine glands, renal/urinary system, homeostasis/metabolism

We queried the *Drosophila* genome for homologs using DRSC Integrative Ortholog Prediction Tool (DIOPT), ENSEMBL database and reciprocal BLAST for each of the 25 human 16p11.2 genes. We selected 15 homologs with a DIOPT score of 3.00 or greater, or in the case of *KIF22*^{*klp68D*}, both high query coverage and percentage identity in BLAST. Three genes did not have any homologs, and the remaining seven genes with low or no DIOPT scores had low (<30%) query coverage and/or percentage identity in BLAST. Of the 15 selected homologs, one homolog (*INO80E*^{*CG18004*}) did not have any available RNAi lines. Overall, fly lines of 14 homologs for human 16p11.2 genes were used in this study. Phenotypes due to single gene knockdown or knockout in *Drosophila*, mouse^{3,4} and zebrafish^{5,6} models of the 14 selected homologs are also shown; +: degree of phenotype severity, L: lethality; ND: phenotype not determined. Gene expression in the *Drosophila* eye was determined from FlyAtlas⁷ (adult eye) and modEncode expression data⁸ (imaginal disc, larvae L3 wandering) or from previous functional studies^{9,10,11,12}.

Table S2. RNAi and deficiency fly stocks used for one-hit and two-hit experiments (Excel file). Each tab of the Excel file shows fly and human genes, stock numbers, and sources for all lines, as well as the genotypes for deficiency lines.

Table S3. Quantitative PCR analysis of 16p11.2 homolog knockdowns (Excel file). The first tab of this file lists the percentage of gene expression (mRNA) in 25 RNAi lines of 16p11.2 homologs with *Elav-GAL4>Dicer2* driver at 25°C, or *Elav-GAL4* without *Dicer2* at room temperature for *ALDOA^{ald}* and *PPP4C^{pp4-19C}* RNAi lines due to lethality with *Dicer2*. RNA levels were quantified using qPCR, normalized to *rp49* and expressed relative to levels of RNA in control. The second tab lists the percentage of *tiptop* and *numb* expression (mRNA) in KK RNAi lines of 16p11.2 homologs. Although three genes displayed high levels of *tiptop*, we did not observe the distinct eye phenotypes documented with overexpression of *tiptop* in the tested KK lines and were able to rule out the effect of this overexpression on the eye phenotypes. All genes displayed normal levels of *numb*.

Table S4. Percentiles of *Flyntyper* scores for one-hit knockdown flies with *Dicer2*.

	Gene category	<i>Flyntyper</i>	Rank	Percentile
<i>ATXN2L</i> ^{atx2}	16p11.2 distal	63.39	1	97.37%
<i>UBE3A</i> ^{dUbe3A}	Core Gene	59.05	2	94.74%
<i>KCTD13</i> ^{CG10465}	16p11.2	58.78	3	92.11%
<i>DOC2A</i> ^{rph}	16p11.2	58.61	4	89.47%
<i>PPP4C</i> ^{pp4-19C}	16p11.2	57.63	5	86.84%
<i>SH2B1</i> ^{lnk}	16p11.2 distal	57.47	6	84.21%
<i>CTNNB1</i> ^{arm}	Core Gene	54.60	7	81.58%
<i>TCTEX1D2</i> ^{CG5359}	3q29	52.33	8	78.95%
<i>ATP2A1</i> ^{kum}	16p11.2 distal	52.31	9	76.32%
<i>PIGZ</i> ^{CG3419}	3q29	51.92	10	73.68%
<i>ZDHC19</i> ^{app}	3q29	49.77	11	71.05%
<i>MAPK3</i> ^{rl}	16p11.2	49.52	12	68.42%
<i>SHANK3</i> ^{prosap}	Core Gene	48.99	13	65.79%
<i>CADPS2</i> ^{caps}	Core Gene	48.64	14	63.16%
<i>NCBP2</i> ^{Cbp20}	3q29	47.23	15	60.53%
<i>CHD8</i> ^{kis}	Core Gene	46.41	16	57.89%
<i>SPNS1</i> ^{spin}	16p11.2 distal	45.77	17	55.26%
<i>TAOK2</i> ^{dTao-1}	16p11.2	42.44	18	52.63%
<i>DLG1</i> ^{dlg1}	3q29	42.04	19	50.00%
<i>PTEN</i> ^{dpten}	Core Gene	40.51	20	47.37%
<i>CCDC101</i> ^{sgf29}	16p11.2 distal	40.02	21	44.74%
<i>KIF22</i> ^{klp68D}	16p11.2	38.48	22	42.11%
<i>TUFM</i> ^{efTuM}	16p11.2 distal	38.40	23	39.47%
<i>BDH1</i> ^{CG8888}	3q29	38.28	24	36.84%
<i>PAK2</i> ^{Pak}	3q29	36.91	25	34.21%
<i>SCN1A</i> ^{para}	Core Gene	35.87	26	31.58%
<i>C16ORF53</i> ^{pa1}	16p11.2	35.19	27	28.95%
<i>TBX6</i> ^{doc3_2}	16p11.2	33.25	28	26.32%
<i>OSTalpha</i> ^{CG6836}	3q29	30.84	29	23.68%
<i>LRRC33</i> ^{CG7896}	3q29	30.37	30	21.05%
<i>ALDOA</i> ^{ald}	16p11.2	30.20	31	18.42%
<i>PCYT1A</i> ^{Cct1}	3q29	28.48	32	15.79%
<i>ASPHD1</i> ^{asph}	16p11.2	28.17	33	13.16%
<i>CORO1A</i> ^{coro}	16p11.2	27.19	34	10.53%
<i>FBXO45</i> ^{Fsn}	3q29	26.88	35	7.89%
<i>PIGX</i> ^{CG30381}	3q29	26.37	36	5.26%
<i>YPEL3</i> ^{CG15309}	16p11.2	25.28	37	2.63%
<i>CDIPT</i> ^{pis}	16p11.2	23.76	38	0.00%
<i>FAM57B</i> ^{CG17841}	16p11.2	NA	NA	NA

Average *Flynotyper* score, rank and percentile for one-hit *GMR-GAL4* knockdown of 16p11.2 homologs (shaded in grey) and other neurodevelopmental genes. *FAM57B*^{CG17841} knockdown caused lethality and was therefore not ranked.

Table S5. Tested and validated pairwise knockdown models between 16p11.2 homologs (Excel file).

Tab 1 lists all tested pairwise interactions between 16p11.2 homologs, including the direction of interaction (enhancer or suppressor, highlighted in yellow), the method of testing (*Flynotyper* or manual scoring), the number of lines tested for each interaction, and the total number of interactions and interacting lines. Tab 2 lists manual scores for pairwise interactions; “ND” represents phenotypes not determined.

Table S6. Tested and validated pairwise knockdown models of 16p11.2 homologs with neurodevelopmental and transcriptome genes (Excel file).

This Excel file lists all tested pairwise interactions of 16p11.2 homologs with other neurodevelopmental genes (Tab 1) and genes identified from the transcriptome data (Tab 2), including the direction of interaction (enhancer or suppressor, highlighted in yellow), the method of testing (*Flynotyper* or manual scoring), the number of lines tested for each interaction, Gene Ontology annotations for cell proliferation or cell cycle, and the total number of interactions and interacting lines. Tab 3 lists manual scores for pairwise interactions at 30°C and 25°C; “ND” represents phenotypes not determined.

Table S7. Differentially-expressed genes in 16p11.2 knockdown flies (Excel file).

This table lists all differentially-expressed genes from RNA sequencing with log-fold change >1 or <-1 and false discovery rate <0.05 for each of the six 16p11.2 knockdown models, as determined by edgeR generalized linear model. The FlyBase ID, log-fold change, log counts per million, F-value test statistic, p-value, corrected false discovery rate, and human homologs identified by DIOPT are included for each differentially-expressed gene.

Table S8. Input and connector genes identified in a human brain-specific interaction network (Excel file).

This table lists all genes connected within the human brain-specific gene interaction network. The input column identifies genes used as inputs into the network (16p11.2 genes, interacting neurodevelopmental genes, or genes identified from transcriptome data for *KCTD13*^{CG10465} and *MAPK3*^{rl} knockdown). Also listed for each gene is the degree (number of edges connecting to each node), number of paths (number of shortest paths between genes that the node is part of), annotations for cell cycle or cell proliferation GO terms, and differential expression of that gene in the 16p11.2 knockdown models.

Table S9. Pathogenicity of 16p11.2 genes based on human allele frequency metrics.

	CNV	pLI rank percentile	RVIS percentile
<i>ALDOA</i>	16p11.2 CNV	50.48	18.59
<i>ASPHD1</i>	16p11.2 CNV	42.04	28.93
<i>C16orf54</i>	16p11.2 CNV	25.51	
<i>C16orf92</i>	16p11.2 CNV	51.92	68.98
<i>CDIPT</i>	16p11.2 CNV	79.27	8.75
<i>CORO1A</i>	16p11.2 CNV	14.32	21.41
<i>DOC2A</i>	16p11.2 CNV	52.01	19.73
<i>FAM57B</i>	16p11.2 CNV	36.03	26.23
<i>GDPD3</i>	16p11.2 CNV	86.01	57.15
<i>HIRIP3</i>	16p11.2 CNV	51.91	79.52
<i>INO80E</i>	16p11.2 CNV	52.27	48.12
<i>KCTD13</i>	16p11.2 CNV	21.89	30.07
<i>KIF22</i>	16p11.2 CNV	79.74	34.88
<i>MAPK3</i>	16p11.2 CNV	32.46	26.23
<i>MAZ</i>	16p11.2 CNV	14.36	
<i>MVP</i>	16p11.2 CNV	56.27	12.05
<i>PAGR1</i>	16p11.2 CNV	29.88	
<i>PPP4C</i>	16p11.2 CNV	22.81	44.54
<i>PRRT2</i>	16p11.2 CNV	35.65	81.38
<i>QPRT</i>	16p11.2 CNV	27.57	80.73
<i>SEZ6L2</i>	16p11.2 CNV	41.52	6.58
<i>SPN</i>	16p11.2 CNV	43.63	34.60
<i>TAOK2</i>	16p11.2 CNV	6.13	0.60
<i>TBX6</i>	16p11.2 CNV	49.77	50.22
<i>TMEM219</i>	16p11.2 CNV	64.55	38.58
<i>YPEL3</i>	16p11.2 CNV	41.94	66.57
<i>ELN</i>	Williams syndrome	76.94	47.20
<i>GTF2I</i>	Williams syndrome	5.41	
<i>KANSL1</i>	17q21.31 syndrome	4.48	30.95
<i>NSD1</i>	Sotos syndrome	0.53	3.24
<i>RAI1</i>	Smith-Magenis syndrome	5.68	0.25
<i>SHANK3</i>	Phelan-McDermid syndrome	4.13	
<i>TBX1</i>	DiGeorge syndrome/VCFS	11.13	
<i>UBE3A</i>	Prader-Willi/Angelmans syndrome	4.93	19.54

Rank percentiles of ExAC loss-of-function constraint metric (pLI) intolerance to variation (RVIS) scores are shown for all 16p11.2 genes and causative genes for select syndromic CNVs. The pLI and RVIS rank percentile scores for several 16p11.2 genes, including *TAOK2*, *CORO1A*, *PPP4C*, *KCTD13*, *MAPK3*, and *MAZ*, are similar to known pathogenic and disease-associated genes, indicating that they all share an importance in human development.

Table S10. Primers used in the PCR experiments (Excel file).

Tab 1 of the Excel file shows sequences for the forward and reverse TAIL-PCR primers, while tab 2 lists all primers used in qPCR experiments.

Table S11. Statistical analysis of experimental data (Excel file).

This table shows all statistical information (test used, control and experimental data, test statistics, p-values, confidence intervals, and sample size) for data presented in the main and supplemental figures.

References

1. Krishnan A, *et al.* Genome-wide prediction and functional characterization of the genetic basis of autism spectrum disorder. *Nat Neurosci* **19**, 1454-1462 (2016).
2. Warde-Farley D, *et al.* The GeneMANIA prediction server: biological network integration for gene prioritization and predicting gene function. *Nucleic Acids Res* **38**, W214-220 (2010).
3. Blake JA, Bult CJ, Kadin JA, Richardson JE, Eppig JT, Mouse Genome Database G. The Mouse Genome Database (MGD): premier model organism resource for mammalian genomics and genetics. *Nucleic Acids Res* **39**, D842-848 (2011).
4. Jayachandran R, *et al.* Coronin 1 regulates cognition and behavior through modulation of cAMP/protein kinase A signaling. *PLoS Biol* **12**, e1001820 (2014).
5. Blaker-Lee A, Gupta S, McCammon JM, De Rienzo G, Sive H. Zebrafish homologs of genes within 16p11.2, a genomic region associated with brain disorders, are active during brain development, and include two deletion dosage sensor genes. *Disease models & mechanisms* **5**, 834-851 (2012).
6. Golzio C, *et al.* KCTD13 is a major driver of mirrored neuroanatomical phenotypes of the 16p11.2 copy number variant. *Nature* **485**, 363-367 (2012).
7. Chintapalli VR, Wang J, Dow JA. Using FlyAtlas to identify better *Drosophila melanogaster* models of human disease. *Nat Genet* **39**, 715-720 (2007).
8. Celniker SE, *et al.* Unlocking the secrets of the genome. *Nature* **459**, 927-930 (2009).
9. Wernet MF, Desplan C. Homothorax and Extradenticle alter the transcription factor network in *Drosophila* ommatidia at the dorsal rim of the retina. *Development* **141**, 918-928 (2014).
10. Bharathi V, Pallavi SK, Bajpai R, Emerald BS, Shashidhara LS. Genetic characterization of the *Drosophila* homologue of coronin. *J Cell Sci* **117**, 1911-1922 (2004).
11. Biggs WH, 3rd, *et al.* The *Drosophila* rolled locus encodes a MAP kinase required in the sevenless signal transduction pathway. *EMBO J* **13**, 1628-1635 (1994).
12. Sarpal R, Ray K. Dynamic expression pattern of kinesin accessory protein in *Drosophila*. *Journal of biosciences* **27**, 479-487 (2002).